Compressible vortices and shock-vortex interactions

Thesis by

Gerard O'Reilly

In Partial Fulfillment of the Requirements
for the Degree of
Doctor of Philosophy

California Institute of Technology
Pasadena, California

2004
(Submitted May 17, 2004)

Acknowledgements

I'd like to thank my advisor Prof. Pullin for his guidance and support. His insightful counsel after numerous incidents of "clutching defeat from the jaws of victory" will always be appreciated. Further, I'd like to thank the ASC combustion and compressible turbulence group for aiding me throughout the course of this work, both financially and academically, and also for many interesting and informative lunchtime discussions. To the entire Iris(h) lab crew, in order of appearance: mrubel, pog, pphilch, bobba-shrimp, big vince, the fatman and dr. sober. Thank you for the unrelated titillating conversations and acrimonious arguments.

I'm eternally indebted to my adoring wife Sissi, for her cynical encouragement and infinite patience in dealing with the long evenings and weekends spent at work (rtd). Finally, I'd like to dedicate this dissertation to my mother and father. Their strength, optimism and reassurance have made this endeavor possible.

This work was supported by the Advanced Simulation Computing program (ASC) under subcontract no. B523297 of DOE contract W-7405-ENG-48.

Abstract

Secondary instabilities on the organized, spanwise, vortical structures in incompressible shear layers, play an important role in generating the onset of three-dimensional turbulence in such flows. The effect of increasing compressibility on these instabilities is examined by using the compressible Stuart vortex as a model for a compressible shear layer. It is found that both two- and three-dimensional subharmonic instabilities cease to promote pairing events even at moderate M_∞. The fundamental mode becomes dominant as M_∞ is increased, and a new instability corresponding to an instability on a parallel shear layer is observed. The interaction of a shock with a compressible vortex may be viewed as a simplified model of the general interaction of a shock with the coherent structures in a turbulent flow field. An approximate theory for computing shock-compressible-vortex interactions is developed, based on Ribner (1954). The problem of convection of a frozen pattern of vorticity, dilatation, temperature and entropy through a planar shock wave is considered. The refraction and modification of the upstream disturbances into the three basis modes permitted by the linear Euler equations is derived, as well as the perturbation to the shock wave. This theory is used to compute approximate post-shock states corresponding to shock-CSV interactions, a model for shock shear layer interactions. The method is verified by comparing its approximate post-shock fields with those computed explicitly using AMROC, a finite difference, AMR-WENO code. Finally, numerical solutions corresponding to a compressible analogue of the Mallier & Maslowe vortex (a periodic array of counter-rotating vortices) are presented. These solutions admit the existence of large regions of smooth supersonic flow, and could potentially be used to model the counter-rotating vortices arising from the single- and multi-mode Richtmyer-Meshkov instability.

Contents

List of Figures

List of Tables

Chapter 1 Introduction

The impulsive acceleration of an initially plane interface separating two fluids of different densities, brought about by a shock wave propagating normal to the interface, is known as the Richtmyer-Meshkov instability. Small disturbances on the interface are amplified leading to many compressible phenomena, including shock interactions, hydrodynamic instabilities and non-linear growth of the interface. Ultimately, the Richtmyer-Meshkov instability precipitates transition to a turbulent mixing region across a wide range of Mach numbers, where the amount of turbulent mixing increases with shock Mach number.

The Kelvin-Helmholtz instability, often present in shearing flows, causes the interface between two fluids moving at different velocities to wrinkle and grow, which eventually leads to a turbulent mixing zone between the two speed fluids. It is of fundamental importance in understanding free shear layers, and is partly responsible for the transition to turbulence of the Richtmyer-Meshkov induced mixing zone. Increasing compressibility has a dramatic effect on the nature of free shear layers. Supersonic mixing layers grow much less quickly than an incompressible mixing layer at the same free-stream velocity and density ratio. Also, the turbulent mixing zone is less ordered and shows highly three-dimensional structures. These structures can generate shock waves when convected downstream with supersonic velocity.

The interaction of shock waves with turbulent flows is one of the most important phenomenon observed in supersonic flow, giving rise to shock wave reflection, scattering and diffraction. It's also known to be one of the major sources of acoustic noise, such as that produced by wakes, mixing layers and boundary layers. Shock-turbulent interactions can also occur during the re-shock of the Richtmyer-Meshkov instability, where a reflected shock passes through the turbulent mixing zone. It is seen that the mixing and turbulence are enhanced by the additional vorticity produced by the passage of the shock.

All three of the above phenomena arise in the context of many man-made and natural applications. Effectuating energy production by means of inertial confinement fusion has long been impeded by mixing between the capsule and the fuel within, where the mixing is caused by the Richtmyer-Meshkov instability. A greater understanding of this instability, and the means by which it can be suppressed, is required to increase final compression and actually generate energy. Another problem of great interest is the control of pollutant emissions. Improved models of compressible mixing, and a deeper comprehension of the role of large scale vortices in entraining un-mixed free-stream fluid in compressible shear layers is necessary to predict chemical reactions more accurately.

All three physical processes are important in scram jet engine research. The limiting factor in these engines is the time taken to mix the fuel and oxidizer (the latter of which is traveling at supersonic speeds). For heat release to generate thrust the mixing must occur in the combustion chamber. Therefore, reduced mixing in supersonic shear layers is a major obstacle in producing positive thrust. For hypersonic air-breathing engines Yang *et al.* [93] postulate that by utilizing shock-induced mixing and the Richtmyer-Meshkov instability this problem may be overcome.

To understand some of these mechanisms more fully, a basic modeling approach will be undertaken here. The models developed and used in this dissertation are simple enough so that the problems considered remain tractable, but incorporate enough of the underlying physics to be interesting. In particular, the compressible Stuart vortex, Meiron *et al.* [52], is used to examine the suppression of secondary instabilities in compressible mixing layers, Chapters 2 and 3. In Chapter 4, a model for the counter-rotating vortices in the Richtmyer-Meshkov mixing zone is proposed. Such a model could prove useful in designing shock-vortex interaction aimed at producing re-shock like behavior. Finally, an approximate method for computing the interaction of a planar shock with a frozen compressible pre-shock disturbance is designed. Subsequently, this method is used to produce post-shock states corresponding to shock-compressible Stuart vortex interactions, Chapters 5 and 6.

Compressible shear layers: The incompressible turbulent mixing layer has been the subject of many experimental investigations. Winant & Browand [92] studied an incompressible mixing layer at moderate Reynolds number, and found large spanwise organized vortical structures. Brown & Roshko [14] demonstrated the existence of these spanwise structures at large values of the Reynolds numbers. It has been shown that these large eddies are principally responsible for boosting the growth rates of incompressible shear layers and fluid entrainment into the mixing region, via pairing and amalgamations: Winant & Browand [92], Brown & Roshko [14], Browand & Latigo [13], Bernall & Roshko [4] and Moore & Saffman [57].

With the advent of high-speed propulsion systems, experiments involving compressible mixing layers gained importance. Brich & Eggers [5] compiled a survey of free turbulent shear layer data and showed that as the Mach number increased, the turbulent growth rate decreased. This was initially thought to be due to the different free stream densities used to increase the free stream Mach number. Brown & Roshko [14] showed that the large decrease in growth rates was produced by increasing compressibility, not by density effects. Bogdanoff [8] and Papamoschou & Roshko [69] used the concept of convective Mach number, M_c, to investigate this reduction in growth rates, finding good collapse in the growth-rate data. More recently Slessor *et al.* [89] suggest a new scaling parameter suitable for flows with far from unity free-stream density and sound-speed ratios. Gas compressibility also produces changes in the large-scale vortex structures in mixing layers. Experimental evidence for the form of these structures is not definitive; Goebel & Dutton [26], Samimy & Elliot [83], Hall *et al.* [28], Clemens & Mungal [21] and Papamoschou & Bunyajitradulya [67]. It's clear from these experiments that the large-scale all structures become more three-dimensional as M_c increases.

Much numerical and analytical work has been done using parallel models for the compressible shear layer: Lees & Lin [43], Lin [47], Lessen *et al.* [44, 45], Blumen [6], Blumen *et al.* [7], Sandham & Reynolds [86, 85], Zhuang *et al.* [97, 96] and Zhuang & Dimotakis [95]. These works show a clear decrease in linear growth rates as M_c increases, and further, that three-dimensional instabilities are more vigorously amplified at higher Mach numbers. Non-parallel base flows, including the incompressible Stuart vortex and Kelvin-Helmholtz billows, have been used to determine the two- and three-dimensional stability properties of incompressible free shear layers; Pierrehumbert & Widnall [72], Klaassen & Peltier [36, 37, 38]. These works illustrate the effect and importance of secondary instabilities, related to the organized vortical structures present in incompressible mixing layers, for generating the onset of three-dimensional turbulent flow. Presently we wish to utilize a non-parallel flow model for the compressible shear layer in a effort to study the role of compressibility in suppressing some of these secondary instabilities. This model is the compressible Stuart vortex (CSV) proposed by Meiron, Moore & Pullin [52] as a continuation to finite Mach number of the Stuart [90] vortex.

The CSV is briefly reviewed in Chapter 2, where an analysis for the structure of the CSV when the mass flux in the closed cat's eyes regions is small is also presented. In this chapter a connection is made between the CSV and steady perturbations to parallel shear flows with tanh-velocity profiles in a compressible fluid. This link partially motivates the extension of the theory of stability of plane parallel flows to include the stability of the spatially nonuniform CSV states themselves. Chapter 3 outlines our approach to the numerical analysis of the instabilities of compressible shear flows. The instabilities of the CSV are described in §3.3, where comparisons are made with Pierrehumbert & Widnall [72] and Klassen & Peltier [37] in the limit of very small Mach number. The effect of subsonic free-stream Mach number on the linear instabilities which seed pairing interactions, and which generate streamwise streaks, is examined. Increasing the Mach number will be seen to inhibit the effectiveness of the pairing instability to promote pairing events. At larger values of M_c, there does not appear to be one dominantly amplified spanwise wavelength for either of the linear instabilities. This may be a possible explanation for the disorganization of the large-scale structures as the Mach number increases.

Smooth transonic flow: In the spirit of Meiron *et al.* [52] and Moore & Pullin [58, 59] we wish to study the effect of compressibility on steady incompressible vortical solutions of Euler's equations in two dimensions. In particular, it is desired to find a steady compressible vortical solution which admits a large region of smooth supersonic flow, in contrast to Morawetz's [61, 62, 63] results for the non-existence of continuous smooth transonic flow past airfoils. Additionally, the single- and multi-mode Richtmyer-Meshkov instability gives rise to compressible counter-rotating vortices in the mixing region. A model for such vortices would prove beneficial in studying the dynamics of this region and also be useful in modeling the re-shock process, where a reflected shock wave passes though the mixing region.

In Chapter 4 we extend the incompressible Mallier & Maslowe [51] vortex to allow for a finite free-stream sound speed. The Maillier & Maslowe vortex is an exact solution of the incompressible Euler equations, representing a periodic array of counter-rotating vortices. Unlike the Stuart vortex, there are no hyperbolic stagnation points between adjacent vortex cores. Meiron, Moore & Pullin [52] found a small range of the free stream Mach number for which their solutions contained embedded regions of smooth supersonic flow. They speculated that their numerical solution branches terminated due to the formation of weak incipient shocks, brought on by the presence of stagnation points between vortex cores. It was hoped that a compressible analogue of the Mallier & Maslowe would not suffer this limitation, and thereby produce large regions of supersonic flow between the counter rotating vortices (which would effectively be acting as supersonic nozzles).

One surprising result from this study was how increasing compressibility increases the normalized strain at the vortex cores. This in turn was seen to stretch the vortices substantially in the vertical direction. We find that the compressible Mallier & Maslowe vortex allows for smooth regions of supersonic flow to develop between the vortex cores. Solution branches still terminate at a finite value of the inverse of free stream Mach number. The termination appears to be due to a combination of the large vertical gradients in the divergence of the velocity field, potentially due to the onset of weak shocks in the supersonic region, and the increased strain rate in the vortex cores.

Shock-vortex interactions: The study of an interface under an impulsive acceleration was considered theoretically and numerically by Richtmyer [79]. Later his findings were qualitatively confirmed by the shock-tube experiments of Meshkov [53]. The emergence of inertial fusion as a potential power source has motivated many experimental studies of accelerated and shock-processed interfaces. Meshkov [53] and Aleshin [1] used a thin pre-shaped membrane, designed to rupture when impinged on by the shock, to create a density interface. Brouillette & Sturtevant [12] extracted a thin plate from the test-section just prior to shock tube firing, where the wake of the plate was used to perturb the interface. Jacobs *et al.* [34] and Budzinski *et al.* [15] used a gas curtain to separate the different density gases. Each of these methods suffers limitations: The shattered membrane contaminates the post-shock flow and prevents advanced diagnostic tools from being used. Perturbations to the initial interface produced by thin plate extraction are non-uniform and not easily reproducible. The dynamics of the two-interface gas curtain systems are more complicated, and less relevant, than the single-interface configuration.

The problem of interface generation has been solved more recently by using a vertical shock-tube with side-slots, Jones & Jacobs [35] and Collins & Jacobs [22]. The experiments are membrane-less, reproducible, and allow the use of advanced diagnostic techniques, such as planar laser-induced fluorescence. Their results agree with Richtmyer's predictions for early time growth of the interface, and also capture the $1/t$ long time growth behavior of the mixing region. Their visualizations clearly show the counter-rotating vortices generated by the instability, and the effect of re-shock on enhancing mixing and triggering transition to a final turbulent state.

Richtmyer's original analysis has also been greatly extended over the past couple of decades. Mikaelian [55] considered an analytical theory of Richtmyer-Meshkov instabilities in an arbitrary number of stratified fluids. Hann [29] incorporated weakly non-linear effects in computing the evolution of the interface. This analysis was later augmented (by using Pade approximates) to be valid for longer time, Zhang & Sohn [94]. One shortcoming of Zhang & Sohn's work was that it did not give the correct late time asymptotic scaling for growth rate decrease. Sadot *et al.* [81] addressed this weakness, and developed a model which provided the correct late time form. Saffman & Meiron [82] and Pham & Meiron [70] used an impulsive pressure distribution to approximate the shock, thereby providing an initial conditions for a fully non-linear simulation of the finite amplitude stage of the instability. Samtaney & Zabusky [84] examined the baroclinic vorticity generation by a shock on density inhomogeneities, and derived scaling laws for the circulation deposited per unit length of the un-shocked interface.

The interaction of a shock wave with a turbulent field is also an important problem, with respect to the re-shock process, shock enhanced mixing and as a major source of acoustic noise. Ribner [75, 77] used an approximate method to study noise generation by shock-incompressible-turbulence interactions, while Mahesh *et al.* [49, 50] and Lee *et al.* [41, 42] used both rapid distortion theory and numerical simulations to study the response of turbulence to a shock wave. The interaction of a shock with a vortex may be viewed as a simplified model of the general interaction of a shock wave with the coherent structures of a turbulent flow field. Ribner [76, 78] again used his approximate method to study the cylindrical acoustic waves generated by such and interaction. Also, much numerical work has been done on sound production by shock-vortex interactions, Grasso & Pirozzoli [27], Inoue & Hattori [32], Inoue & Takahashi [33] and Inoue [31].

Presently, we wish to develop an analytical method, by which the net effect of the passage of a shock through a compressible vortex can be computed. As did Pham & Meiron [70], we will produce a post-shock field as an initial condition for a high-order numerical method, and study its evolution without the need for a shock capturing scheme. We develop a theory which accounts not just for shock-compression, but also the baroclinic generation of vorticity and shock curvature. To do this we first make the ansatz that the passing of the shock occurs instantaneously. If the smooth pre-shock field can be decomposed into a frozen sum of sinusoidal modes, the interaction of each mode with the shock may be computed analytically. The post-shock modes are then summed to produce an approximate post-shock field.

Chu & Kovasznay [20] have shown that it's possible to decompose a weak disturbance in a viscous heat conducting fluid into three basic modes; a steady, incompressible vorticity mode, a steady incompressible, variable density entropy mode and a compressible, irrotational, unsteady acoustic mode. The interaction of each eigenmode with a shock has been analyzed: Ribner [74] investigated the vorticity eigenmode, Moore [60] the acoustic mode and Chang [18] the entropy eigenmode. Obviously, a general flow cannot be decomposed into a sum of modes, each of which satisfies the linearized Euler equations. In Chapter 5 a theory is developed to treat the interaction of a general frozen weak distribution of vorticity, dilatation, temperature and entropy. This theory is based on Ribner's analysis, and allows for pre-shock perturbations which are not bound by the linearized Euler equations. The shape of the perturbed shock and the downstream flow induced by this shock is computed. This theory is used in Chapter 6 to compute approximate post-shock fields corresponding to shock-CSV interactions (a model for a normal shock-compressible shear layer interactions) which are then used as an initial condition in a fully nonlinear simulation.

Chapter 2 Compressible Stuart vortex

In this chapter the structure of the linear array of compressible Stuart vortices (CSV; Stuart [90], Meiron, Moore & Pullin [52]) is investigated analytically. The CSV is a family of steady, homentropic, two-dimensional solutions to the compressible Euler equations, parameterized by the free stream Mach number M_∞, and the mass flux ϵ inside a single vortex core. It may be considered a model for a compressible shear layer, with known solutions having $0 \leq M_\infty < 1$. In particular, we study the CSV when ϵ is small and M_∞ is finite using a perturbation expansion in powers of ϵ. This interesting limit was overlooked by Meiron, Moore & Pullin [52]. The steady compressible Euler equations are written here in stream-function density form, the solution to which will be used extensively as a steady, compressible, non-uniform base-flow for the stability analysis presented in Chapter 3. An eigenvalue determining the structure of the perturbed vorticity and density fields is obtained from a singular Sturm-Liouville problem for the stream-function perturbation at $O(\epsilon)$. The resulting small-amplitude, steady CSV solutions are shown to represent a bifurcation from the neutral point in the stability of a parallel shear layer with a tanh-velocity profile in a compressible, inviscid perfect gas at uniform temperature.

2.1 Euler equations

To facilitate the analysis of the CSV, we briefly review the formulation of Meiron, Moore & Pullin [52], henceforth referred to as MMP, who considered the steady compressible Euler equations, together with the equation of state for a calorically perfect gas, for a shear flow in two-dimensional Cartesian co-ordinates (x, y), with x the streamwise or periodic direction, and y the transverse coordinate. The fluid velocity, vorticity, density and entropy will be denoted by $\mathbf{u}$, $\boldsymbol{\omega}$, ρ and s respectively, and, in this chapter, $*$ will indicate a dimensional quantity. The subscript ∞ is used to refer to uniform reference quantities as $y \to \pm\infty$, where the flow consists of opposed uniform streams, each with speed U_∞^*. In the following, unsubscripted fluid quantities are made non-dimensional against their reference values at infinity, and entropy is scaled against c_v. The free stream Mach number is $M_\infty = U_\infty^*/c_\infty^*$.

MMP constructed a compressible continuation of the incompressible Stuart vortex for $M_\infty > 0$. A stream function, $\psi(x, y)$-vorticity formulation of the steady, compressible Euler equations was used where the velocity components are given by

$$\rho u = \frac{\partial \psi}{\partial y}, \qquad \rho v = -\frac{\partial \psi}{\partial x}, \tag{2.1}$$

MMP then assumed homentropic flow, and that the total enthalpy depends on $\psi(x, y)$ alone, $h \equiv h(\psi)$. A closed set of equations was obtained for the choice, $dh/d\psi = e^{-2\mu\psi}$, where μ is a parameter to be discussed subsequently. The momentum and energy equations may then be written as

$$\nabla^2\psi - \frac{1}{\rho}\left(\nabla\psi \cdot \nabla\rho\right) = \rho^2 e^{-2\mu\psi}, \tag{2.2}$$

$$\frac{M_\infty^2}{2}\left(\nabla\psi\right)^2 + \frac{\rho^2\left(\rho^{\gamma-1} - 1\right)}{\gamma - 1} = \frac{M_\infty^2 \rho^2}{2}\left(1 - \frac{1}{\mu} e^{-2\mu\psi}\right). \tag{2.3}$$

On the semi-infinite rectangle, $\{\mathcal{R} : x \in [0, \pi], y \in [0, \infty]\}$, the boundary conditions are

$$\frac{\partial \psi}{\partial y} = 0 \quad \text{on} \quad (y = 0, 0 \le x \le \pi), \qquad \frac{\partial \psi}{\partial x} = 0 \quad \text{on} \quad (x = 0, 0 \le y \le \infty), \tag{2.4}$$

$$\psi \sim y + \theta_d \quad \text{as} \quad (y \to \infty, 0 \le x \le \pi), \qquad \rho \to 1 \quad \text{as} \quad (y \to \infty, 0 \le x \le \pi). \tag{2.5}$$

which require symmetry about $y = 0$. MMP show that two further conditions are needed to characterize solutions to (2.2-2.3). The first is to specify

$$\epsilon = \psi(0, 0) - \psi(\pi, 0), \tag{2.6}$$

where ϵ, $0 \le \epsilon < \infty$, is the mass flux inside the vortex core. The second is a constraint on the total dimensionless circulation. This can be determined by equating the area integral of vorticity over R, to the line integral of tangential velocity over ∂R. The tangential velocity is zero everywhere on ∂R except at infinity, where it has unit value over a distance π, implying the final constraint is written as

$$\int\int_{\mathcal{R}} \omega(x,y)dxdy = -\pi. \tag{2.7}$$

The unknowns are $\psi(x, y; M_\infty, \epsilon)$, $\rho(x, y; M_\infty, \epsilon)$, $\mu(M_\infty, \epsilon)$, and $\theta_d(M_\infty, \epsilon)$.

2.1.1 Incompressible Stuart vortex

When $M_\infty \to 0$, with ϵ fixed, the solution to (2.2-2.3) is $\rho(x, y) = 1$, $\mu = 1$ and

$$\psi = \ln\left(\kappa\cosh(y) + \sqrt{\kappa^2-1}\cos(x)\right), \quad \omega = -\left(\kappa\cosh(y) + \sqrt{\kappa^2-1}\cos(x)\right)^{-2}. \tag{2.8}$$

The mass flux may be written as $\epsilon = 2\ln\left(\kappa + \sqrt{\kappa^2-1}\right)$, from which it is easily verified that $\kappa = \cosh(\epsilon/2)$. This is the incompressible Stuart vortex [90]. The parameter $\kappa \in (1, \infty)$ parameterizes the family of solutions. When $\kappa = 1$, $\epsilon \to 0$, a parallel flow is obtained, $u = \tanh(y)$. When $\kappa \to \infty$, ψ describes the potential flow produced by an infinite array of point vortices with spacing 2π. Intermediate κ gives a smooth, periodic distribution of vorticity, where ψ is even about the lines $x = \pm n\pi$ with n integer. The steady streamline pattern is a periodic array of cat's eyes, with stagnation points on the symmetry line at $y = 0$. The displacement thickness is $\theta_d = \ln(\kappa/2)$.

2.1.2 Homentropic continuation

MMP found a continuation of the Stuart vortex to homentropic, compressible flow by obtaining a family of solutions to (2.2-2.3) with two parameters, M_∞, and ϵ. For well-posedness, they found it necessary to treat $\mu(M_\infty, \epsilon)$ as an eigenvalue, its value being determined by solving the non-linear governing equations. For a given ϵ, their numerical solutions indicated a small range of subsonic M_∞ for which locally supersonic smooth flow field existed, while above some maximum, but subsonic, value of M_∞ the solution branch was found to terminate. The termination is thought to be due to the onset of shocklets in the supersonic region, induced by the presence of the hyperbolic stagnation points between the vortices, which would invalidate the governing equations. No two-dimensional solutions were found to exist for $M_\infty \geq 1$. For $M_\infty \ll 1$, at finite ϵ, a Rayleigh-Janzen expansion showed that μ is determined from a solvability condition on the linearized equations, giving

$$\mu_0(M_\infty) = 1 + \frac{M_\infty^2}{2} + \mathcal{O}(M_\infty^4). \tag{2.9}$$

To $\mathcal{O}(M_\infty^2)$, μ_0 is independent of ϵ. It follows that the limiting solution for the homentropic CSV when $\epsilon \to 0$ at finite M_∞ is not given by its incompressible counterpart, where $\mu \to 1$ as $\epsilon \to 0$. This small mass-flux limit was not resolved by MMP, and is analyzed presently. It is also shown that this solution is intimately connected with the neutral stability point in the stability of parallel compressible flows.

2.2 Small mass flux limit; $\epsilon \ll 1$, M_∞ finite

We analyze the homentropic CSV equations, (2.2) and (2.3), at finite M_∞ for $\epsilon << 1$. These equations are perturbed about a parallel constant density profile of form to be determined from the analysis. This small mass flux solution is shown to coincide with neutrally stable perturbations to a CD base profile, Blumen [6]. Thus, the connection of the CSV to linearized-stability theory may be established. Numerical solutions of the CSV equations, following MMP, suggest an expansion of the form

$$\begin{aligned} \psi(x,y;M_\infty,\epsilon) &= \psi_0(y;M_\infty) + \epsilon\,\psi_1(x,y;M_\infty) + \mathcal{O}(\epsilon^2), && (2.10)\\ \rho(x,y;M_\infty,\epsilon) &= 1 + \epsilon\,\rho_1(x,y;M_\infty) + \mathcal{O}(\epsilon^2), && (2.11)\\ \mu(M_\infty,\epsilon) &= \mu_0(M_\infty) + \mathcal{O}(\epsilon^2), && (2.12) \end{aligned}$$

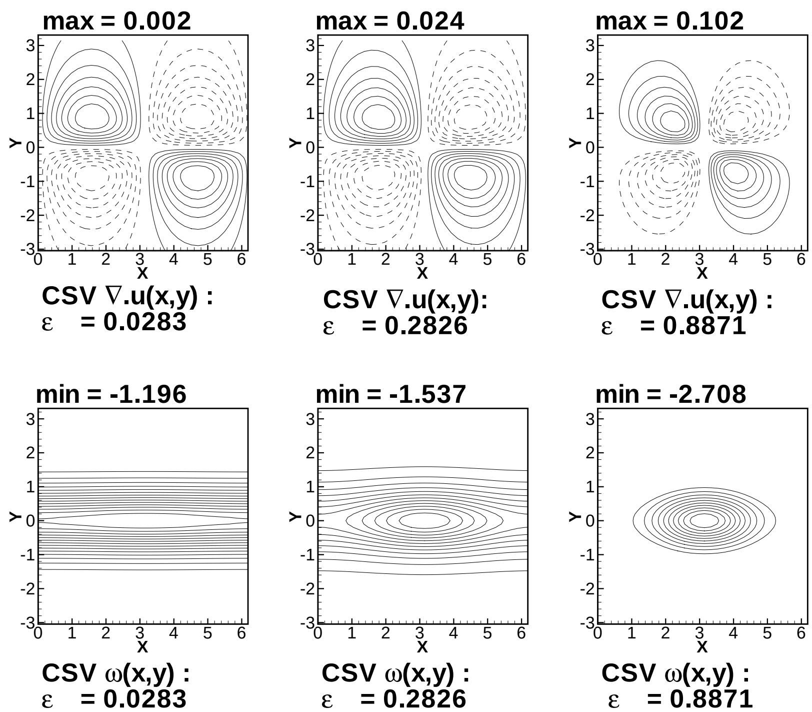

Figure 2.1: Examples of CSV profiles for $M_\infty = 0.51$. The maximum contour value is given for each profile; dashed lines will always indicate negative contours.

where $\mu_0(M_\infty)$ is to be determined. On substitution into (2.2) and (2.3), it is found that

$$\text{Momentum}: \quad \mathcal{O}(1) \quad \frac{\mathrm{d}^2\psi_0}{\mathrm{dy}^2} = \mathrm{e}^{-2\mu_0\psi_0}, \tag{2.13}$$

$$\text{Momentum}: \quad \mathcal{O}(\epsilon) \quad \nabla^2\psi_1 + 2\mu_0\mathrm{e}^{-2\mu_0\psi_0}\psi_1 = 2\mathrm{e}^{-2\mu_0\psi_0}\rho_1 + \frac{\mathrm{d}\psi_0}{\mathrm{dy}}\frac{\partial\rho_1}{\partial\mathrm{y}}, \tag{2.14}$$

$$\text{Enthalpy}: \quad \mathcal{O}(1) \quad \left(\frac{\mathrm{d}\psi_0}{\mathrm{dy}}\right)^2 = 1 - \frac{1}{\mu_0}\mathrm{e}^{-2\mu_0\psi_0}, \tag{2.15}$$

$$\text{Enthalpy}: \quad \mathcal{O}(\epsilon) \quad \left(\frac{1}{\mathrm{M}_\infty^2} - \left(\frac{\mathrm{d}\psi_0}{\mathrm{dy}}\right)^2\right)\rho_1 = \left(\mathrm{e}^{-2\mu_0\psi_0}\right)\psi_1 - \left(\frac{\mathrm{d}\psi_0}{\mathrm{dy}}\right)^2\frac{\partial\psi_1}{\partial\mathrm{y}}. \tag{2.16}$$

Integrating equation (2.15) and imposing the boundary condition (2.4) gives

$$\psi_0(y) = \frac{1}{\mu_0}\ln\left(\cosh(\mu_0 y)\right) - \frac{1}{2\mu_0}\ln(\mu_0). \tag{2.17}$$

It should be noted that equations (2.13) and (2.15) are equivalent. Equation (2.13) can be obtained from equation (2.15) by differentiating (2.15) with respect to y. It follows that, $\psi_1(x,y)$ and $\rho_1(x,y)$ must decay to zero as $y\to\infty$, since boundary condition (2.5) is satisfied by equation (2.17). At this stage, $\mu_0(M_\infty)$ remains undetermined, implying that expression (2.17) for ψ_0 is incomplete. To proceed, (2.17), (2.16) and (2.14) are used to obtain a single equation for ψ_1.

$$\begin{aligned}\frac{\partial^2\psi_1}{\partial x^2} \; + \; &\frac{\cosh^2(\mu_0 y)}{\cosh^2(\mu_0 y) - M_\infty^2\sinh^2(\mu_0 y)}\,\frac{\partial^2\psi_1}{\partial y^2} \\ &+ \frac{2\mu_0 M_\infty^2\tanh(\mu_0 y)\cosh^2(\mu_0 y)}{\left(\cosh^2(\mu_0 y) - M_\infty^2\sinh^2(\mu_0 y)\right)^2}\,\frac{\partial\psi_1}{\partial y} \\ &+ \frac{2\mu_0^2(1-M_\infty^2)\cosh^2(\mu_0 y)}{\left(\cosh^2(\mu_0 y) - M_\infty^2\sinh^2(\mu_0 y)\right)^2}\,\psi_1 = 0.\end{aligned} \tag{2.18}$$

Using $f(y;\alpha_s)$ to denote the cosine-transform of ψ_1 (where α_s is the steady streamwise wavenumber) allows equation (2.18) to be rewritten as

$$\frac{d^2 f}{dy^2} + \frac{2\mu_0 M_\infty^2 \tanh(\mu_0 y)\mathrm{sech}^2(\mu_0 y)}{1 - M_\infty^2 \tanh^2(\mu_0 y)} \frac{df}{dy} + \\ + \left(\frac{2\mu_0^2(1 - M_\infty^2)\,\mathrm{sech}^2(\mu_0 y)}{1 - M_\infty^2 \tanh^2(\mu_0 y)} + \alpha_s^2 \left(M_\infty^2 \tanh^2(\mu_0 y) - 1 \right) \right) f = 0. \quad (2.19)$$

Boundary condition (2.4) and the change of variables $\zeta = \tanh(\mu_0 y)$ yields a singular Sturm-Liouville problem for $f(\zeta;\alpha_s)$, with eigenvalue $\lambda = (\alpha_s/\mu_0)^2$,

$$\frac{d}{d\zeta}\left(\frac{1-\zeta^2}{1 - M_\infty^2 \zeta^2} \frac{df}{d\zeta} \right) + \left(\frac{2\,(1 - M_\infty^2)}{(1 - M_\infty^2 \zeta^2)^2} - \lambda \frac{1}{1-\zeta^2} \right) f = 0, \quad (2.20)$$

$$f'(\zeta = 0; \alpha, M_\infty) = f(\zeta = 1; \alpha, M_\infty) = 0. \quad (2.21)$$

Using this equation for $f(\zeta;\alpha_s)$, a singular Sturm-Liouville equation for the transform of the density perturbation, $r(\zeta;\alpha_s)$, may be derived.

$$\frac{d}{d\zeta}\left(\frac{1-\zeta^2}{\zeta^2} \frac{dr}{d\zeta} \right) - \lambda \left(\frac{1 - M_\infty^2 \zeta^2}{\zeta^2\,(1-\zeta^2)} \right) r = 0, \quad (2.22)$$

$$r'(\zeta = 0; \alpha_s, M_\infty) = r(\zeta = 1; \alpha_s, M_\infty) = 0. \quad (2.23)$$

Hence, μ_0 is to be obtained from an eigensolution of the $\mathcal{O}(\epsilon)$ equation for ψ or ρ. Solving equations (2.20) and (2.22) for $f(\zeta;\alpha_s)$ and $r(\zeta;\alpha_s)$, followed by taking the inverse cosine transforms gives

$$\lambda = 1 - M_\infty^2, \quad \alpha_s = 1, \qquad \mu_0 = \frac{1}{\sqrt{1 - M_\infty^2}}. \quad (2.24)$$

$$\psi_1(x,y) = \cos(x)\mathrm{sech}\,(\mu_0 \mathrm{y})^{1-\mathrm{M}_\infty^2}, \qquad \rho_1(x,y) = \mu_0 M_\infty \psi_1(x,y). \quad (2.25)$$

Unexpectedly, the eigensolutions to (2.20) and (2.22) are the same, implying $\rho_1(x,y)$ is identical to $\psi_1(x,y)$ up to a normalization factor for consistency with equation (2.16). The parallel stream function, when $\epsilon \to 0$, is thus given by (2.17), with $\mu_0(M_\infty)$ given by (2.24). Thus, the limiting parallel shear flow for the CSV when $\epsilon \to 0$ with M_∞ fixed may be obtained from its incompressible counterpart upon application of a Prandtl-Glauret stretching in the y-direction. Clearly, the solution branch terminates as $M_\infty \to 1$. The above expressions are expected to be uniformly valid in M_∞, when $\epsilon \ll 1$, and agrees with the numerical solution of MMP to six figures. Expanding $\mu_0(M_\infty)$ in (2.24) for $M_\infty \ll 1$ gives agreement with the Rayleigh-Janzen expression for $\mu_0(M_\infty)$, equation (2.9), to $\mathcal{O}(M_\infty^2)$.

2.2.1 Steady perturbations to a parallel shear layer

In this section we show how the solution of equation (2.22) may be linked to a steady perturbation to a parallel, compressible constant density shear layer. To obtain the appropriate equation for the density perturbation requires equations governing unsteady perturbations to a parallel steady compressible flow field. The constant density (CD) profile to be defined as,

$$\overline{u}(y) = \tanh(\omega_h y), \quad \overline{\rho}(y) \equiv 1, \quad \delta = \frac{2}{\omega_h}, \tag{2.26}$$

where the parameter ω_h is used to set the vorticity thickness and variables with over bars will denote steady base flow quantities. As in Chapter 3, where z is defined as the spanwise direction, the perturbations in velocity, density and entropy are denoted $\mathbf{u}'(x, y, z, t)$, $\rho'(x, y, z, t)$ and $s'(x, y, z, t)$ respectively. Defining the following partial differential operators,

$$\mathbf{L} = \frac{\partial}{\partial t} + \overline{u}(y)\frac{\partial}{\partial x}, \quad \mathbf{D}_x = \frac{\partial}{\partial x}, \quad \mathbf{D}_y = \frac{\partial}{\partial y}, \quad \mathbf{D}_z = \frac{\partial}{\partial z}, \tag{2.27}$$

allows the linearized unsteady governing equations to be written as:

$$\mathbf{L}\rho' + \mathbf{D}_x u' + \mathbf{D}_y v' + \mathbf{D}_z w' = 0, \tag{2.28}$$

$$\mathbf{D}_x\rho' + M_\infty^2 \mathbf{L} u' + M_\infty^2 \frac{d\overline{u}}{dy} v' + \mathbf{D}_x \frac{s'}{\gamma} = 0, \tag{2.29}$$

$$\mathbf{D}_y\rho' + M_\infty^2 \mathbf{L} v' + \mathbf{D}_y \frac{s'}{\gamma} = 0, \tag{2.30}$$

$$\mathbf{D}_z\rho' + M_\infty^2 \mathbf{L} w' + \mathbf{D}_z \frac{s'}{\gamma} = 0, \tag{2.31}$$

$$\mathbf{L}s' = 0. \tag{2.32}$$

A similar set of equations governing perturbations to a non-uniform, variable density, steady base flow will be derived in Chapter 3. To link solutions of equation (2.22) to steady solutions of equations (2.28)-(2.32) requires that a single equations for $\rho'(x, y, z, t)$ be obtained.

Firstly, for the homentropic base flow defined by equation (2.26), the linear entropy equation, equation (2.32), implies that the entropy perturbation may be set to zero, $s'(x, y, x, t) \equiv 0$, effectively eliminating γ from the resulting system of equations. Next, apply $M_\infty^2 L$ to the linearized continuity equation, equation (2.28), calling the result (I). Then take D_y times the linear y-momentum equation, equation (2.30), plus D_x times the linear x-momentum equation, equation (2.29), to remove $v'(x, y, z, t)$ from equation (I). Next use D_z times the linear z-momentum equation, equation (2.31), to eliminate $w'(x, y, z, t)$ from equation (I), yielding equation (II). Now operate on the linear x-momentum equation with L, use the linear y-momentum equation to eliminate $v'(x, y, z, t)$ from this equation to give (III). Finally, take L times equation (II) minus $2D_x$ times equation (III), to obtain the following single partial differential equation for $\rho'(x, y, z, t)$,

$$\left(M_\infty^2 L^3 - L\left(D_x^2 + D_y^2 + D_z^2\right) + 2\frac{d\overline{u}}{dy} D_x D_y \right) \rho'(x, y, z, t) = 0. \tag{2.33}$$

Setting the time derivatives in equation (2.33) to zero allows steady solutions to be obtained. For 2D disturbances to a parallel flow, there is stability to any perturbation with streamwise wave number larger than the steady wavenumber; Lin [47]. Obtaining the steady solutions will allow steady (transitional) wavenumbers to be determined. Take the Fourier transform in x and z, and denote the streamwise and spanwise wavenumbers at which the steady solutions may be found α_s and β_s. Define $\hat{\alpha}_s^2 = \alpha_s^2 + \beta_s^2$, $\hat{\alpha}_s \hat{M}_\infty = \alpha_s M_\infty$, and use the transformation $\zeta = \tanh(\omega_h y)$, to obtain the following singular Sturm-Liouville equation, with eigenvalue $\lambda = \hat{\alpha}_s^2/\omega_h^2$, for the steady transformed density perturbation, $r_s(\zeta; \alpha_s, \beta_s)$,

$$\frac{d}{d\zeta}\left(\frac{1-\zeta^2}{\zeta^2}\frac{dr_s}{d\zeta}\right) - \lambda\left(\frac{1-\hat{M}_\infty^2\zeta^2}{\zeta^2(1-\zeta^2)}\right) r_s = 0, \tag{2.34}$$

$$r_s(1) = r_s(-1) = 0. \tag{2.35}$$

In the two-dimensional limit this equation and its solution are identical to equation (2.22) and its eigensolution, $r(\zeta; \alpha_s)$. For non-trivial solutions to equation (2.34), the parameters (ω_h, $\hat{\alpha}_s$, $\hat{M}_\infty$) must be connected through the eigenvalue relationship derived previously. This implies that

$$\frac{1}{\omega_h^2} = \frac{\alpha_s^2(1-M_\infty^2)+\beta_s^2}{(\alpha_s^2+\beta_s^2)^2}. \tag{2.36}$$

When ω_h is specified, this condition defines a zero contour on which remaining parameters must lie. Thus, non-trivial steady disturbances to the hyperbolic tangent profile, are obtained only for parameters M_∞, α_s and β_s, which lie on the surface defined in $(\alpha - \beta - M_\infty)$ space. Disturbances which lie just inside the steady surface are amplified, while those just outside are neutral; Lin [47] and Lessen *et al.* [44]. Stuart [90] linked his solution to stable perturbations to a parallel, hyperbolic, incompressible shear layer. For the present analysis if the Mach number is set to zero, the incompressible solution of Michalke [54] is obtained.

2.3 Interpretations and remarks

We have shown that the two-dimensional steady-stability wavenumber of a parallel shear flow in a constant temperature, compressible perfect gas is a stability bifurcation point where, at given free-stream Mach number, the solution branch corresponding to the CSV begins. This establishes a link between the linear stability of a class of parallel shear flows with tanh-velocity profiles in a compressible fluid, and this special class of steady solutions to the Euler equations.

We remark that the two-dimensional continuations of the finite mass flux CSV from a parallel flow, at fixed Mach number, is not unique. In particular a continuation from a three-dimensional neutral stability point is possible since the relevant stability curves do not terminate when the free-stream Mach number becomes supersonic. Introducing β_s in equation (2.36) allows α_s to remain real, or μ to remain finite, as the sonic threshold is crossed. If such a continuation were admissible it may enable the construction of vortical, three-dimensional, globally supersonic solutions to the steady compressible non-linear Euler equations.

Chapter 3 Linearized stability of the compressible Euler equations

To investigate the normal-mode stability of the generally spatially-nonuniform linear array of compressible Stuart vortices (CSV; Stuart [90], Meiron *et al.* [52]), the linear partial-differential equations describing the time evolution of small perturbations to the CSV base state are solved numerically using a normal mode analysis in conjunction with a spectral method. The effect of increasing M_∞ on the two main classes of instabilities found by Pierrehumbert & Widnall [72] for the incompressible limit $M_\infty \to 0$ is studied. It is found that both two- and three-dimensional subharmonic instabilities cease to promote pairing events even at moderate M_∞. The fundamental mode becomes dominant at higher Mach numbers, although it ceases to peak strongly at a single spanwise wavenumber. We also find, over the range of ϵ investigated, a new instability corresponding to an instability on a parallel shear layer. The significance of these instabilities to experimental observations of growth in the compressible mixing layer is discussed.

3.1 Stability of nonuniform steady flows

To study the linearized stability of the CSV, the time evolution of small perturbations to solutions of equations (2.2)-(2.3), with finite ϵ and M_∞, is considered. For the investigation of stability, the ψ-ρ formulation of Chapter 2 is not appropriate and we utilize a primitive variable formulation in which, for given M_∞ and ϵ, the 2π streamwise periodic CSV base state is denoted by $(\overline{\rho}(x,y), \overline{u}(x,y), \overline{v}(x,y), \overline{s}(x,y))$. Here, x denotes the streamwise periodic direction, and y the transverse coordinate. The flow variables are nondimensionalized as Chapter 2, that is, velocity and density by their free stream values, U^*_∞ and ρ^*_∞, and entropy by c_v.

Before proceeding with the stability analysis, it is important to discuss the limitations of the CSV as a model of the non-linear waves which are physically realizable in a compressible parallel flow. Both experiments and numerical simulations indicate that as M_c is increased beyond 0.6, the large-scale structures in the mixing layer become three dimensional, a property which is not captured by the CSV. Furthermore, DNS of compressible vortices show entropy variations in the core, whereas the CSV is homentropic. Also, in a physical shear layer, the vorticity is compressed into thin regions, known as braids, between the vortex centers. The present two-dimensional CSV shows no such structures at the hyperbolic stagnation points. Nevertheless, the CSV is still a useful model for examining the effect of compressibility in suppressing the interaction between neighboring vortices in the compressible mixing layer environment.

Small perturbations to the base state are denoted

$$\begin{aligned} \chi &\equiv [\rho', \mathbf{u}', s'], \\ &\equiv [\rho'(x,y,z,t), u'(x,y,z,t), v'(x,y,z,t), w'(x,y,z,t), s'(x,y,z,t)], \end{aligned} \tag{3.1}$$

where z is the spanwise direction and $\mathbf{u}'$ denotes the three velocity components. The perturbations, assumed to be isentropic, have a modal representation of the form,

$$[\rho', \mathbf{u}', s'](x,y,z,t) = \; e^{i\alpha x}\, e^{i\beta z}\, e^{-\sigma t}[\hat{\rho}, \hat{\mathbf{u}}, \hat{s}](x,y). \tag{3.2}$$

For parallel base flows, the x dependence of hatted quantities is dropped. For non-parallel base flows, the hatted quantities are taken to be periodic in x, with the same period as the base flow. The y boundary conditions to be enforced, are, that as $y \to \pm\infty$, the hatted quantities decay to zero. No constraint will be placed on the parameters α and β, save that they be real. For non-parallel, periodic base flows, $0 \leq \alpha < 1$. The parameter β is the wavenumber of disturbances in the spanwise direction. For parallel base flows, it may be coupled together with α to define the angle of a particular disturbance ϑ as $\tan(\vartheta) = \beta/\alpha$. This does not have meaning for non-parallel base flows. No claim is made that perturbations (3.2) are complete or that perturbations do not exist which have an algebraic dependence on time.

The five linearized equations to be considered are the continuity, three momentum and entropy equations. Assuming (3.2) leads to an eigenvalue problem, with eigenvalue $\sigma = \sigma_r + i\,\sigma_i$, the real part of which represents exponential growth/decay,

$$\begin{aligned}
(\mathbf{L}_1 + \nabla\cdot\overline{\mathbf{u}})\,\hat{\rho} + (i\alpha\overline{\rho} + [\overline{\rho}, x])\,\hat{u} + [\overline{\rho}, y]\,\hat{v} + i\beta\overline{\rho}\,\hat{w} &= \sigma\hat{\rho} &(3.3)\\
\frac{1}{\overline{\rho}}\,(i\alpha g_1 + [g_1, x] + \mathbf{L}_2\overline{u})\,\hat{\rho} + \left(\mathbf{L}_1 + \frac{\partial\overline{u}}{\partial x}\right)\hat{u} + \left(\frac{\partial\overline{u}}{\partial y}\right)\hat{v} + \frac{1}{\overline{\rho}}\,(i\alpha g_2 + [g_2, x])\,\hat{s} &= \sigma\hat{u} &(3.4)\\
\frac{1}{\overline{\rho}}\,([g_1, y] + \mathbf{L}_2\overline{v})\,\hat{\rho} + \left(\frac{\partial\overline{v}}{\partial x}\right)\hat{u} + \left(\mathbf{L}_1 + \frac{\partial\overline{v}}{\partial y}\right)\hat{v} + \frac{1}{\overline{\rho}}\,[g_2, y]\,\hat{s} &= \sigma\hat{v} &(3.5)\\
\frac{1}{\overline{\rho}}\,i\beta g_1\,\hat{\rho} + \mathbf{L}_1\hat{w} + \frac{1}{\overline{\rho}}\,i\beta g_2\,\hat{s} &= \sigma\hat{w} &(3.6)\\
\left(\frac{\partial\overline{s}}{\partial x}\right)\hat{u} + \left(\frac{\partial\overline{s}}{\partial y}\right)\hat{v} + \mathbf{L}_1\hat{s} &= \sigma\hat{s} &(3.7)
\end{aligned}$$

The operators $\mathbf{L}_1$, $\mathbf{L}_2$, and $[\cdot,\cdot]$, and the functions g and h may be defined as

$$\mathbf{L}_1 = i\alpha\overline{u} + \overline{\mathbf{u}}\cdot\nabla, \qquad \mathbf{L}_2 = \overline{u}\frac{\partial}{\partial x} + \overline{v}\frac{\partial}{\partial y}, \quad [f, x] = \frac{\partial f}{\partial x} + f\frac{\partial}{\partial x}, \tag{3.8}$$

$$g_1(x,y) = \frac{1}{\gamma M_\infty^2}\left(1 + (\gamma-1)\,e^{\overline{s}(x,y)-\overline{s}_\infty}\right)\,\overline{\rho}^{\gamma-1}(x,y), \tag{3.9}$$

$$g_2(x,y) = \frac{1}{\gamma M_\infty^2}\,e^{\overline{s}(x,y)-\overline{s}_\infty}\,\overline{\rho}^{\gamma-1}(x,y). \tag{3.10}$$

As $M_\infty \to 0$, the linearized equations approach a singular limit. For homentropic base flows the linearized entropy equation decouples from the remaining equations, implying

$$\frac{ds'}{dt} = 0, \quad s'(t) \equiv s(t, x(t), y(t)) \quad \text{where} \quad \dot{x}(t) = \overline{u}(x,y),\ \dot{y}(t) = \overline{v}(x,y). \tag{3.11}$$

Thus, a normal-mode assumption combined with the linear approximation, imply, without loss of generality, that perturbations to a homentropic flow may be assumed to be homentropic.

Using similar arguments to those used by Pierrehumbert & Widnall [72], henceforth referred to as PW, some useful symmetry properties of equations (3.3)-(3.7) may be derived. Putting $\beta \to -\beta$, and reversing the sign of $\hat{w}$, an eigenfunction belonging to σ, for wavenumber β, may be turned into an eigenfunction belonging to the same eigenvalue, but now for wavenumber $-\beta$. Thus, it is only necessary to consider $\beta > 0$. A similar argument gives $\alpha > 0$. Finally, as a consequence of the time reversibility of the Euler equations, every exponentially damped mode has a corresponding exponentially growing mode. This means that the only stable modes are the neutral modes, $\sigma_r = 0$.

3.1.1 Numerical method

To find the spectrum of A, it must be approximated by a finite order matrix, whose eigenvalues can be found using conventional methods. This is done using a spectral collocation technique. The perturbations, $(\hat{\rho}, \hat{\mathbf{u}}, \hat{s})$, are spectrally represented with basis functions that satisfy the boundary conditions. Spectral differentiation and integration is used to compute the individual components of the discretized matrix. The basis functions are not orthogonal; therefore, care must be taken to convert the resulting discretized system to standard eigenvalue form.

The techniques described, for non-parallel, periodic base flows, are adapted from Boyd [9, 10, 11] and Cain *et al.* [16]. The discretized perturbations are written as

$$(\hat{\rho}, \hat{\mathbf{u}}, \hat{s})(x, y) = \sum_{m=-\frac{N_x}{2}+1}^{\frac{N_x}{2}} \sum_{n=0}^{N_y-3} (a_{mn}, \mathbf{b}_{mn}, c_{nm}) \mathrm{e}^{imx} \Phi_n(y), \tag{3.12}$$

where $\Phi_n(y)$ are basis functions, which decay as $y \to \pm\infty$. The interval $(-1, 1)$ is stretched onto $(-\infty, \infty)$ using the algebraic stretching, $Y = y/\sqrt{\eta^2 + y^2}$, where η is the stretching parameter. The functions $\Phi_n(y)$ are combinations of Chebyschev polynomials satisfying the boundary conditions. Letting $\phi_n(y(Y)) = T_n(Y)$,

$$\Phi_n(y) = \begin{cases} \phi_0(y) - \phi_{n+2}(y) & \text{n even} \\ \phi_1(y) - \phi_{n+2}(y) & \text{n odd.} \end{cases}$$

The number of collocation points in y is N_y, chosen to be the zeros of the Chebyschev polynomial of order N_y, with N_x points in x.

3.1.2 Discrete matrix

Discrete operators will be denoted with boldface symbols, and the discrete state vector denoted by $\mathbf{c}$. Thus equations (3.3)-(3.7) may be cast in the following non-standard eigenvalue form, where the growth rates σ appear as the eigenvalues.

$$\mathbf{A}\,\mathbf{c} = \sigma\,\mathbf{B}\,\mathbf{c}.$$

The matrix $\mathbf{A}$ is a block matrix, with $N_e \times N_e$ blocks, each representing a single term, multiplying any of $(\hat{\rho}, \hat{\mathbf{u}}, \hat{s})$, from the left hand side of the system of equations (3.3)-(3.7). Each block is dense and of size $N_b \times N_b$, where $N_b = N_x\,(N_y - 2)$. Thus $\mathbf{A}$ is a $N \times N$ dense matrix, where $N = N_e\,N_b$. Storage requirements for $\mathbf{A}$ limited the maximum values of N_x and N_y which could be used.

Let $q(x,y)$ be a general function of the base flow, and of the parameters (α, β, M_∞), defined from the left hand side of equations (3.3)-(3.7). Then, the type of integral which must be considered in computing a general element from any of the blocks of $\mathbf{A}$ is

$$I_A(k,s,m,n) \;=\; \int_{-\infty}^{\infty}\int_0^{2\pi} \frac{\eta}{\eta^2+y^2}\, q(x,y)\, e^{imx}\, e^{-ikx}\, \phi_n(y)\,\phi_s(y)\,dx\,dy,$$

where (k,s,m,n) define the element in the block and $q(x,y)$ characterizes the block. The basis functions in x and y imply

$$I_A(k,s,m,n) \approx \sum_{i=1}^{N_x}\sum_{j=1}^{N_y} w_x(k)\,w_\xi(s)\,q(x_i,\xi_j)\,e^{imx_i}\,e^{-ikx_i}\,\cos\left(n\xi_j\right)\,\cos\left(s\xi_j\right),$$

where $w_x(k)$, and $w_\xi(s)$ are the normalization weights, x_i are the collocation points in the x-direction, and ξ_j the inverse cosine of the collocation points Y_j. The summations are done using routines from the FFTW package.

The matrix $\mathbf{B}$ is a constant block-diagonal matrix, depending only on the parameters (N_e, N_x, N_y). The N_e diagonal blocks are identical, the elements of which are given by,

$$I_{\mathbf{B}}(k,s,m,n) = 2\pi\,\delta_{mk} \times \begin{cases} \dfrac{\pi}{2}\,\delta_{ns} \;+ & \begin{array}{ll} \pi & \text{if both}\, n \,\text{and}\, s \,\text{are even} \\ \frac{\pi}{2} & \text{if both}\, n \,\text{and}\, s \,\text{are odd.} \end{array} \end{cases}$$

The eigenvalues of this system were computed using routines from the LAPACK package.

Since all base flows considered presently are unbounded in y, the spectrum of the continuous operator is expected to contain both discrete and continuous components. Our physical interest is in the discrete part, which will represent large-scale, compressible growth dynamics. It was therefore necessary to separate, numerically, the discrete spectrum from the much larger set of eigenvalues that are the discrete approximation to the continuous spectrum. This was done presently by testing the convergence of each eigenvalue and eigenvector with increased resolution, the discrete spectrum showing rapid convergence to four figures or better, while the continuous spectrum converged much more slowly, see Appendix B for details.

3.2 Parallel base flows

The numerical method was verified against known results for the stability of compressible parallel base flows; Sandham & Reynolds [85, 86], Zhuang *et al.* [97], Lin [47], Lessen *et al.* [44]. Two different base flows were investigated, the class of Crocco-Busemann (CB) profiles and a constant density, parallel, hyperbolic-tangent velocity profile (CD), see section 2.2. For the CB profiles, the Crocco-Busemann relationship is used to relate a parallel temperature profile to a parallel velocity profile. Presently, we make the additional simplification of specifying a simple hyperbolic tangent profile, with a parameter ω_h set to fix the vorticity thickness, and $\overline{\tau}(y)$ denoting the temperature profile,

$$\overline{u}(y) = \tanh(\omega_h y), \quad \overline{\tau}(y) = 1 + \frac{1}{2}(\gamma - 1)\, M_\infty^2\, \overline{u}^2(y), \quad \delta = \frac{2}{\omega_h}. \tag{3.13}$$

M_c	σ_r: $N_y = 64$	σ_r: $N_y = 256$	σ_r: S&R
0.01	0.1896791	0.1896792	0.189
0.60	0.1175104	0.1175119	0.116
1.20	0.0529660	0.0529666	0.053

Table 3.1: Calculated values of σ_r, computed at $(\alpha_{max}, \beta_{max})$, compared at different resolutions for the CB profile. S&R $\rightarrow$ [85]

We choose $\omega_h = 1$ giving $\delta = 2$. The resulting profile is close, but not identical, to the true CB profile. The CD profile is homentropic, whereby its stability analysis admits a single equation for $\rho'(x, y, z, t)$, used extensively in Chapter 2.

The convective Mach number M_c, Bogdanoff [8], Papamoschou & Roshko [69], allows results from temporal and spatial stability analysis to be compared. For the type of flows used in this analysis $M_c = M_\infty$, implying that the two may be used interchangeably. Table 3.1 shows results from runs with $N_y = 64$ and $N_y = 256$, $\eta = 1.5$, compared with Sandham & Reynolds [85]. In the range $n = 0 - 40$, the agreement of the Chebyschev coefficients, $(a_n, \mathbf{b}_n, c_n)$, from the different resolutions, is on the order of four figures, where they decay exponentially fast by four orders of magnitude. For values of M_∞ above about 0.6, the most amplified modes become three dimensional, in good agreement with Sandham & Reynolds [85, 86].

3.3 Instabilities of the CSV

We now consider the stability of the nonuniform CSV states. The base flow is given by numerical solutions to (2.2-2.3) obtained by MMP using a spectral method, and repeated here for the stability calculations. We emphasize that known CSV solutions have $0 \leq M_\infty < 1$, even though they may contain embedded regions of locally supersonic flow. Thus our stability analysis is limited to nonuniform compressible shear flows with subsonic free streams. For the stability problem, there is a four-dimensional space of parameters comprising of ϵ, M_∞ for the base flow and α, β. Presently we consider three representative values of ϵ, shown in table 3.2, across a

Case	ϵ	κ
A	0.0283	1.0001
B	0.2826	1.0100
C	0.8871	1.1000

Table 3.2: The three representative values of the mass flux, ϵ, used.

range of M_∞. Figure 2.1 shows examples of the base flow at these values for $M_\infty = 0.51$. Case A is a near-parallel flow and is well represented by the solution derived from the perturbation analysis in Chapter 2. For case C, the base flow is highly non-parallel with the velocities in the x- and y-directions on the same order of magnitude. The coherent spanwise vortices have become compact, and the dilatation has risen by two orders of magnitude from case A. The continuation of case C terminates at M_∞ just above 0.6. This is thought to be due to the presence of shocklets, which appear to decelerate the flow from supersonic conditions at the edge of the vortex, to the stagnation points between the vortex cores. Sandham & Reynolds [86] observed the appearance of shocks in two-dimensional unsteady simulations at similar M_∞. This suggests that case C may provide the best model of the vortical structures in low convective Mach number compressible shear layers.

The spectral solutions reported use $\eta = 1.5$, and $[N_x, N_y] = ([32, 32], [32, 64], [64, 32])$, with four figure agreement found for the growth rates from the various resolution runs. The later resolutions are the highest which could be achieved with available computing resources. It is necessary to scale $(\sigma_r,\ \alpha,\ \beta)$ with the vorticity thickness of the base flow,

$$\delta(\epsilon, M_\infty) = -\frac{1}{\pi} \int_0^{2\pi} \int_0^{\infty} y\, \omega(x, y)\, dx\, dy. \tag{3.14}$$

The scaling factors are given by $\delta(\epsilon, M_\infty)/\delta(\epsilon, 0)$, figure 3.1(a).

3.3.1 Incompressible limit, $M_\infty = 0$

The stability algorithm may be run with $M_\infty = 0.01$ for comparison with PW and Klaassen & Peltier [37], henceforth referred to as KP. We first discuss $\alpha = 0.5$ (first

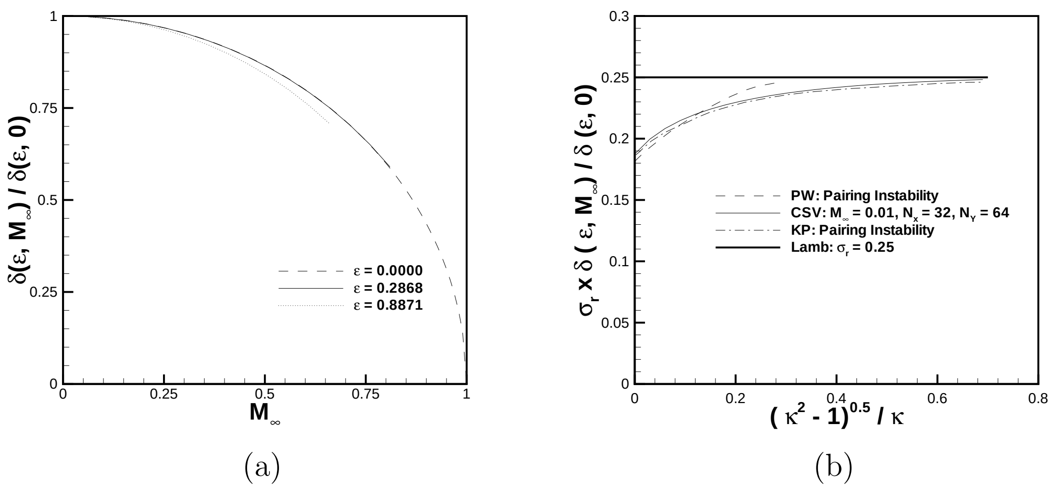

Figure 3.1: (a): Scaling factors determined from the vorticity thickness. The zero mass flux curve is given by $(1-M_\infty^2)^{1/2}$, an expression obtained from the perturbation analysis in the appendix. (b): Comparison with [72] and [37].

subharmonic) in which adjacent vortices in the base flow are displaced in opposite directions. The growth rates for $\alpha = 0.5, \beta = 0$ are shown in figure 3.1(b) as a function of core size parameter. The growth rates are real, increasing monotonically as the core size parameter is increased toward the [39] limit of $\sigma_r = 0.25$ for a row of point vortices. Differences in resolution, $[32, 64]$ presently and $[4, 6]$ for PW, account for the discrepancies in the growth rates. The agreement with KP, who used double the resolution of PW, is satisfactory. Also results very like PW were found using their resolution. We find that growth rates close to the point-vortex limit are achieved at $\epsilon = 1.696$, for which the 2-D pairing growth rate has risen to $\sigma_r = 0.2482$. Modes with finite β are referred to as helical pairing modes. Their growth rates are shown in figure 3.2(a) compared with PW. These modes have a short-wave cutoff off in β, which implies that spanwise scales with $\beta\delta >$ const do not amplify as they advect downstream.

Our final comparison with PW is done for the translative instability for which $\alpha = 0$. Perturbations then have the same x-periodicity as the base flow from which it

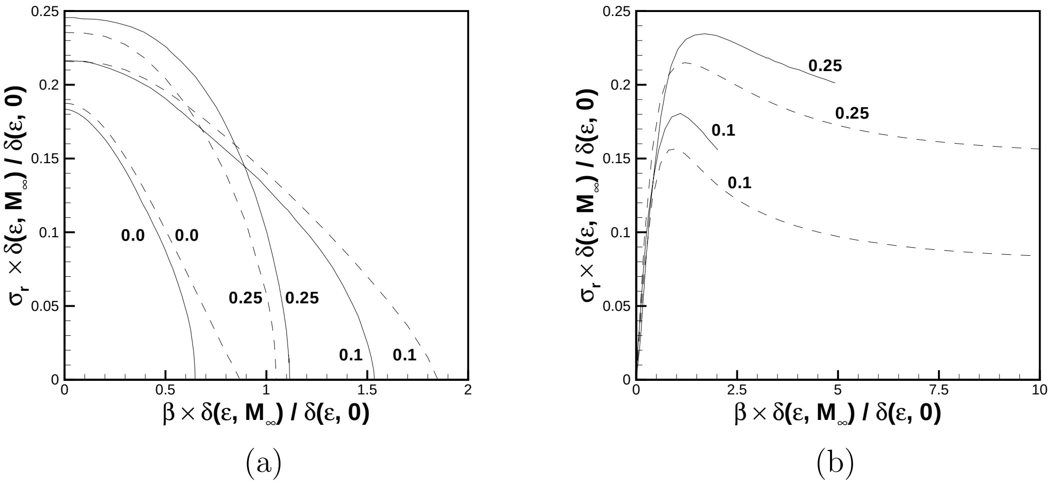

Figure 3.2: Solid lines [72], dashed lines results from CSV runs with $M_\infty = 0.01$. Labels represent the value of the vortex core size parameter. (a): Helical Pairing instability, $\alpha = 0.5$. (b): Translative instability, $\alpha = 0.0$.

follows that this mode is not an extension of any parallel flow instability. The growth rates are shown in figure 3.2(b). When $\epsilon \to 0$ (parallel base flow), the growth rates fall identically to zero. In the incompressible limit, the maximum growth rates of this instability, for fixed ϵ, is just smaller than that of the 2-D pairing instability.

3.3.2 Compressible instabilities

2-D Subharmonic Instabilities

We first discuss two-dimensional modes with $\beta = 0$. Generally, the discrete spectrum consisted of three distinct real eigenvalues. The growth rates of the largest of these eigenvalues are shown in figure 3.3. This eigenvalue always attains its maximum value for the subharmonic mode $\alpha = 0.5$, which seeds the pairing instability. To compute the mode shape, the eigenvector is first normalized, and multiplied by the $e^{i\alpha x}$ phase factor. Each eigenmode is chosen so as to be purely real. The sign and absolute magnitude of these modes are arbitrary, but the magnitude of the perturbation variables relative to each other can be important, as it is an indicator of the dominant mech-

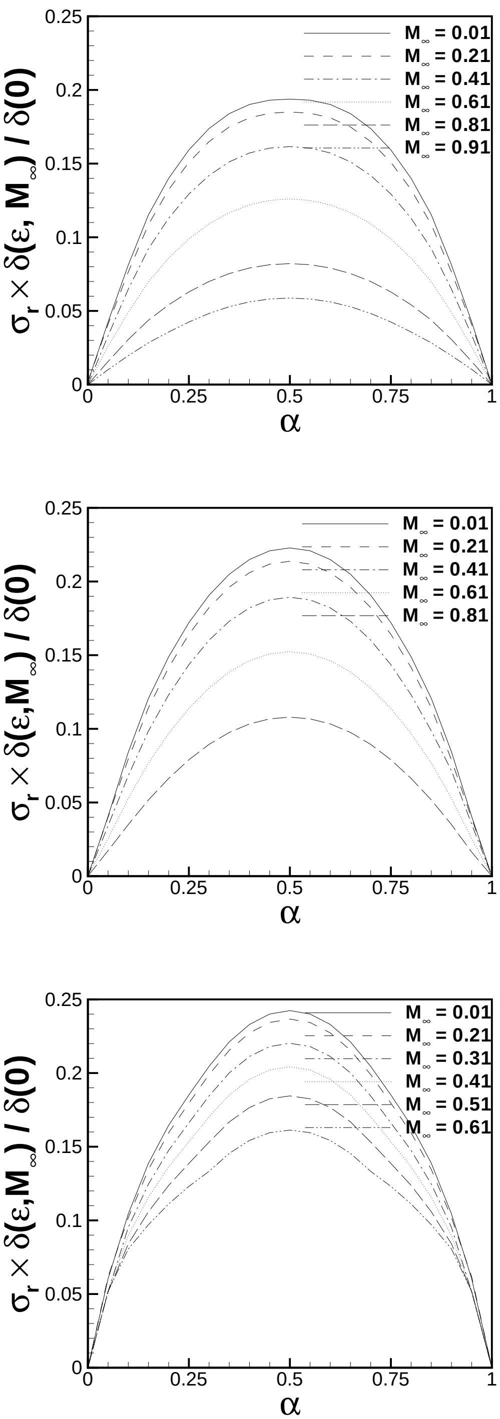

Figure 3.3: Pairing instability growth rates. (a): $\epsilon = 0.0283$, (b): $\epsilon = 0.2826$, (c): $\epsilon = 0.8871$.

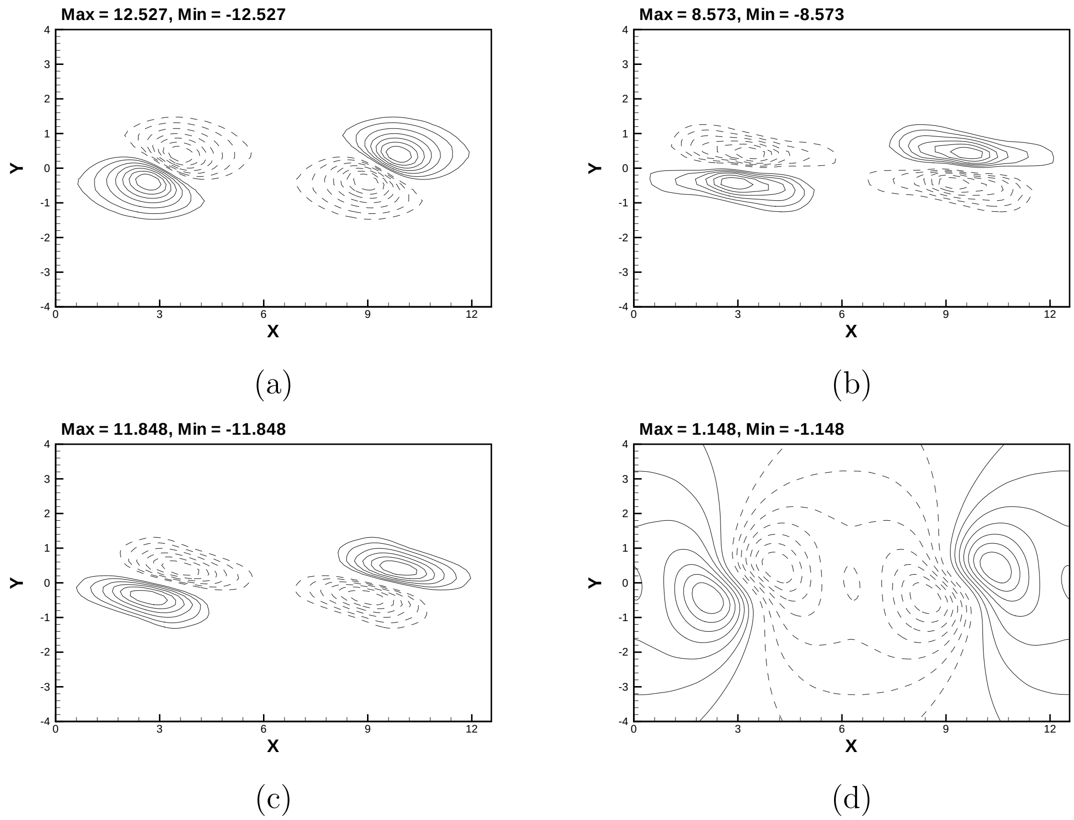

Figure 3.4: 2-D pairing instability, $\epsilon = 0.8871$, (a): $M_\infty = 0.01$, contours of spanwise vorticity. (b): $M_\infty = 0.61$, contours of spanwise vorticity. (c): $M_\infty = 0.61$, contours of dilatation. (d): $M_\infty = 0.61$ contours of density.

anisms by which the linear instability acts in any given area of the parameter space. Figure 3.4 shows contour plots of selected eigenmodes from case C runs. For Case A and B runs, the smaller values of ϵ produce thin, flat base flow vortices, figure 2.1. This is reflected in the eigenmode structure for these case runs, which show similar features to the case C modes. As with parallel base flows, the density perturbation is unimportant for the low Mach number runs, being four orders of magnitude smaller than either of the velocity perturbations. The density eigenmodes keep the same basic shape across the Mach number range, but by $M_\infty = 0.61$ these modes have increased by four orders of relative magnitude.

Two examples of vorticity eigenmodes (obtained from the velocity eigenvectors) are shown in figure 3.4. These resemble a skewed vortex dipole, which become flat-

M_∞	case A	case B	case C
0.01	2.5°	17.1°	28.1°
0.61	0.8°	5.5°	6.1°
0.81	0.5°	3.2°	-

Table 3.3: Values of $|\phi_1|$ for the various mass fluxes investigated.

tened and elongated as M_∞ increases. This eigenmode has a nodal line which runs through the center of the unperturbed vortex. The angle that this nodal line makes with the positive x-axis will be labeled ϕ_1, $-90° < \phi_1 < 0°$. The presence of a sloped nodal line implies that this eigenmode initiates the clockwise rotation of the vortices at $x = \pi$ and $x = 3\pi$ about each other, which ultimately leads to pairing. The more negative ϕ_1, the more effective the eigenmode is at initiating a pairing event. The angle between the line connecting the maximum negative and positive values of vorticity and the nodal line will be denoted ϕ_2, and is a measure of the skewness of the eigenmode. Over the range of M_∞ investigated, ϕ_2 remains almost constant for each of the different case runs; $\phi_2 \sim 28°$ for case A, $\phi_2 \sim 50°$ for case B, and $\phi_2 \sim 68°$ for case C. In contrast, increasing M_∞ has a dramatic effect on ϕ_1, with the slope of the nodal line becoming less negative as M_∞ increases; table 3.3. Thus, increasing compressibility not only damps the growth rate of the pairing instability, but it also decreases the eigenmode's effectiveness in initiating the pairing process, as seen in figure 3.5.

A Parallel Instability

The next most vigorously amplified instability is largely independent of mass flux. Its growth rate behavior and that of an instability to a parallel CD profile show remarkable similarity, figure 3.6. Indeed, growth rates from case A and B runs agree with two- and three-dimensional CD growth rates to within four figures. The eigenmode structure, less the $e^{i\alpha x}$ prefactor, is independent of x, and bears a striking likeness to the structures arising from a CD base profile. This suggests that it corresponds to an instability occurring on the parallel shear layer, and is therefore denoted the *parallel*

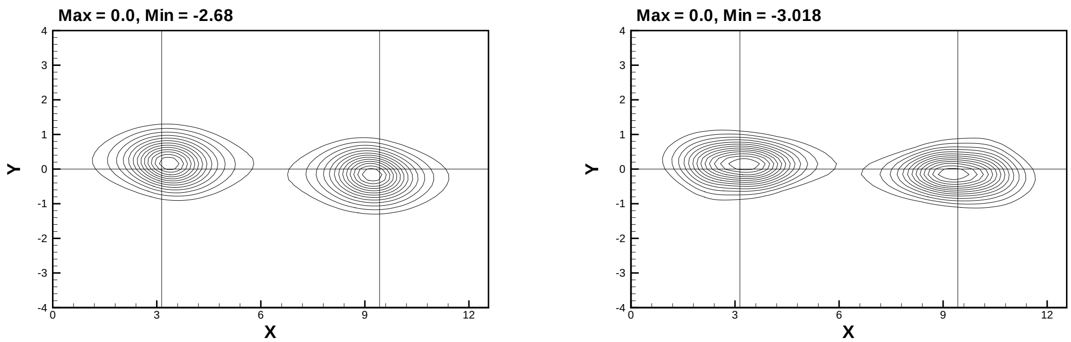

(a) (b)

Figure 3.5: Base flow vorticity in the spanwise direction plus an eigenmode. The eigenmode is computed at a time t_1 such that the maximum value of vorticity of the eigenmode is 20% that of the vorticity in the base flow, $t_1 \propto \sigma_r^{-1}$. The cross marks the center of an unperturbed vortex. (a): $\epsilon = 0.8871$, $M_\infty = 0.01$. (b): $\epsilon = 0.8871$, $M_\infty = 0.61$.

instability. Its presence implies that even after non-linear processes have caused the primary roll up of the parallel flow, the instability which initiated the roll up remains active and relatively unaltered, except that it becomes sub dominant to the more unstable pairing instability.

The real part of the third largest eigenvalue decays rapidly as either M_∞ or ϵ is increased, being extremely weakly amplified for case C runs. For the most part, it maximizes at $\alpha = 0.5$, and so may be considered subharmonic. Over a certain range of the base flow parameters it becomes bimodal, figure 3.7. Its eigenmodes indicate that it tends to alter the strength of neighboring vortices, enhancing one while diminishing another. It may be linked to the *draining instability* discovered by KP, and can be seen as an aid to the pairing process; Winant & Browand [92]. The eigenmodes show some small-scale structure, indicating that these higher order modes are sensitive to numerical inaccuracy and inaccuracy in the inviscid physical model. Due to its weak amplification at higher values of ϵ and M_∞, the 3-D properties of this instability are not investigated exhaustively.

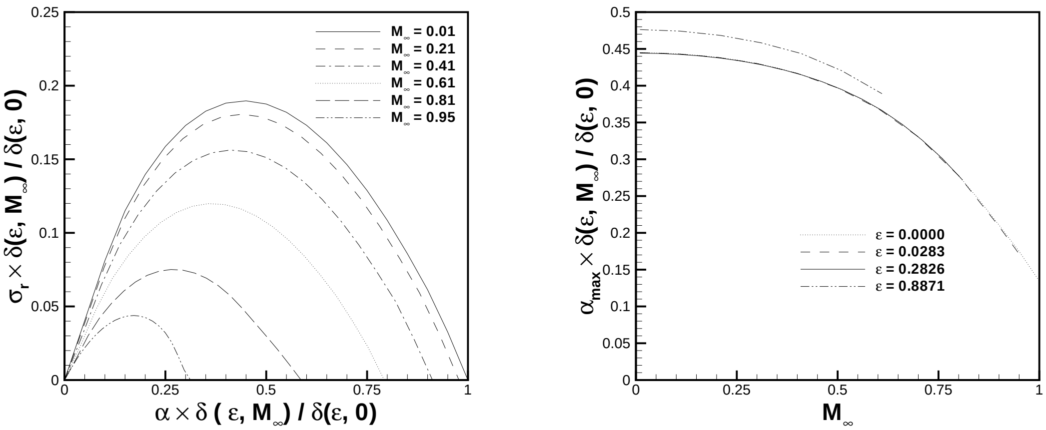

(a) (b)

Figure 3.6: (a): 2-D parallel instability growth rates computed at different mach numbers for $\epsilon = 0.0283$. (b): $\alpha_{max} \times \delta(\epsilon, M_\infty)/\delta(\epsilon, 0)$ vs M_∞; $\epsilon = 0.0$ represents the parallel CD base flow.

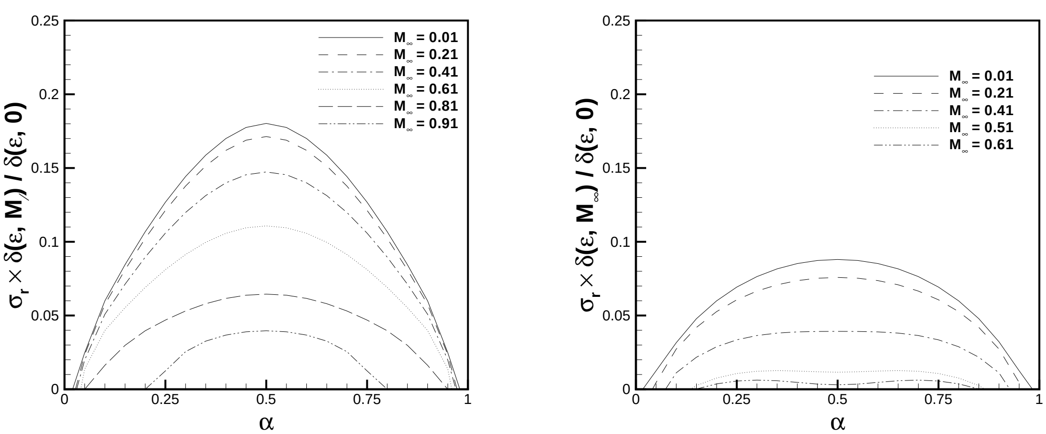

(a) (b)

Figure 3.7: Draining instability; (a) $\epsilon = 0.0283$, (b) $\epsilon = 0.2826$. $\sigma_r \times \delta(\epsilon, M_\infty)/\delta(\epsilon, 0)$ vs α.

3-D Subharmonic Instabilities

We now discuss results obtained for the pairing and parallel instabilities, the two most unstable in two dimensions, for non-zero values of β. Relevant growth rates are shown in figure 3.8. The parallel mode again behaves as if it were an instability on a parallel shear layer, and for $M_\infty < 0.6$, is most unstable in the two-dimensional limit. The pairing mode is also most unstable in the two-dimensional limit below some critical value of M_∞, which decreases as ϵ is increased. The pairing mode remains subharmonic, with $\alpha_{max} = 0.5$ for all values of β and M_∞. Note that for case C runs, above the transitional value of M_∞, for $\beta < 0.25$ the growth rate curves are relatively flat, indicating that there is no single dominating spanwise wavelength. In contrast to the parallel instability, the shortwave cutoff for the pairing mode shows strong dependence on both M_∞ and ϵ. This may be due to thin, flat, vortex-like structures, present in low ϵ base flows, supporting small-scale instabilities, which are all damped by the stabilizing effect of self induced rotation of the more compact vortex cores present in high ϵ base flows, Rosenhead [80].

The z-dependence of the vorticity eigenmodes may be deduced from the symmetry properties of the governing equations. The anti-nodal points of the spanwise vorticity are located at $\beta z = 0, \pm\pi, \pm 2\pi...$, which correspond to the nodal points of both the streamwise and transverse modes. At low Mach numbers, $M_\infty < 0.4$, the spanwise vorticity structure is similar to figure 3.4(a), with difference that ϕ_1 decreases slightly as β increases. PW suggested that the helical pairing mode would promote localized pairing of neighboring vortices. This would lead to phase dislocations in the spanwise direction, Chandrsuda *et al.* [17], and the generation of coherent 3-D structures connecting the spanwise vortices like those seen in plan views of low Mach number mixing layers, Clemens & Mungal [21]. For $M_\infty > 0.4$ the spanwise vorticity assumes a wavy structure, figure 3.9(a). At $\beta z = 0$, the vortex at π is no longer shifted up and to the right, so that localized pairing may occur, rather it now moves up and slightly to the left. Thus, the base flow tends to resist the action of the linear instability. Upon consideration of the streamwise vorticity eigenmode, it is plausible that the

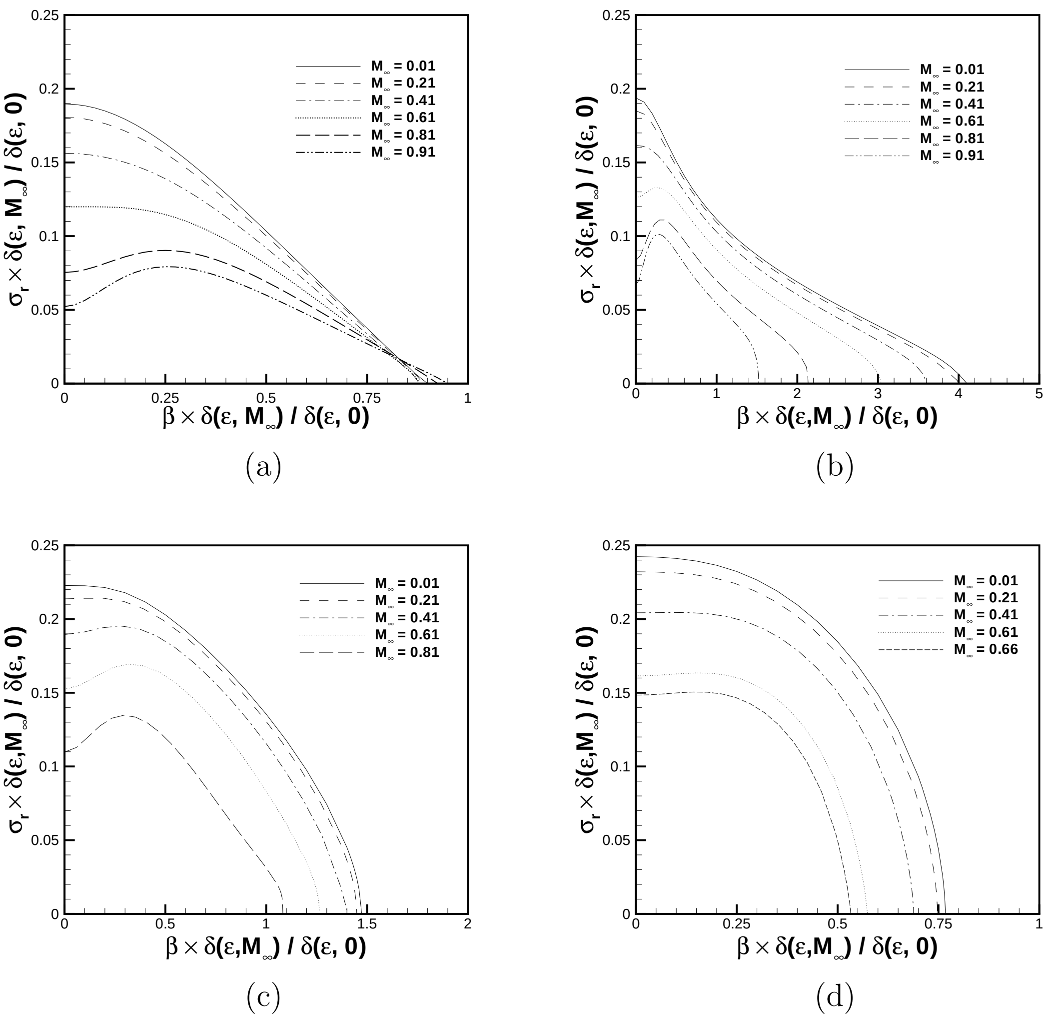

Figure 3.8: Scaled growth rates versus spanwise wavenumber. The streamwise wavenumber is held at its two-dimensional α_{max} value, which depends on M_∞, as β is varied. (a): Parallel instability, $\epsilon = 0.0283$. (b): Helical pairing instability, $\epsilon = 0.0283$. (c): Helical pairing instability, $\epsilon = 0.2826$. (d): Helical pairing instability, $\epsilon = 0.8871$.

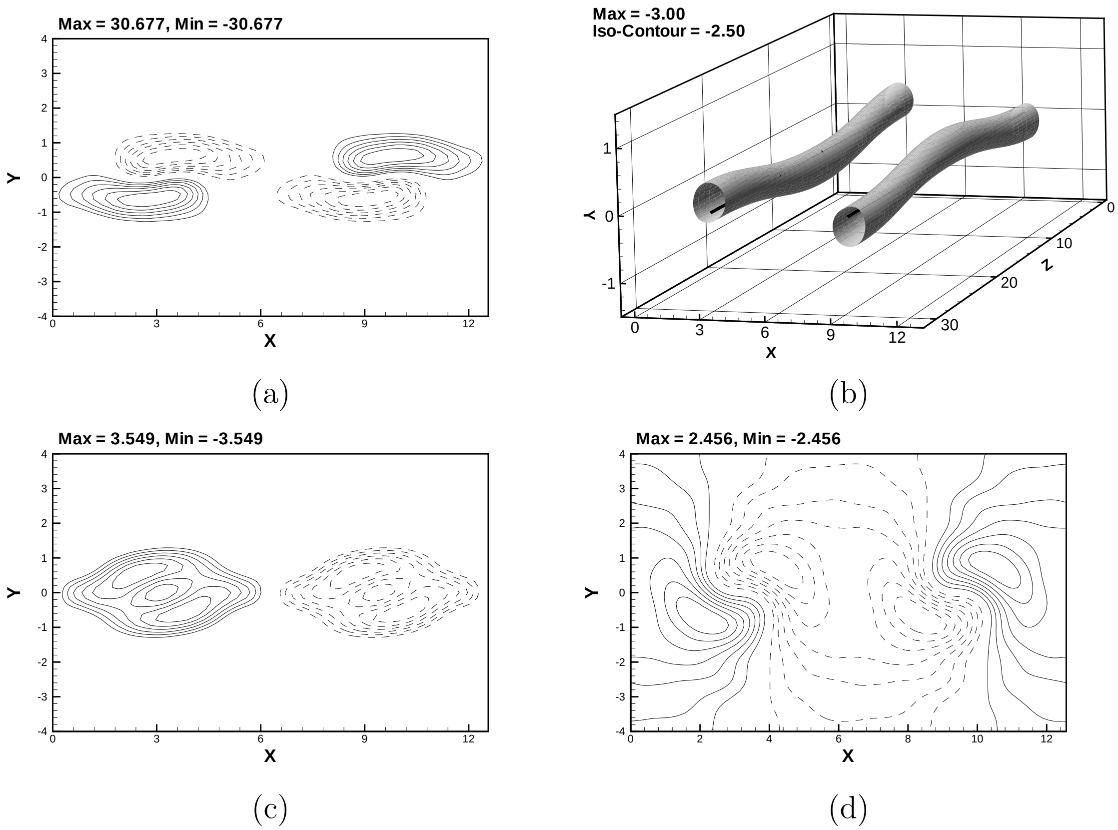

Figure 3.9: Helical pairing eigenmodes, $\beta = \beta_{max} = 0.211$, $\epsilon = 0.8871$, $M_\infty = 0.61$. (a): Spanwise vorticity. (b): Base vorticity plus spanwise perturbation with amplitude chosen so that its max is 20% that of the base flow. (c): Streamwise vorticity. (d): Density.

perturbation of figure 3.9 would lead to a hairpin type structure, with the heads of the hairpin located at $\beta z = 0, 2\pi ...$ and the legs at $\beta z = \pi/2, 3\pi/2...$, Sandham & Reynolds [86]. The fact that these structures are not readily identifiable in mixing layer experiments at low Mach numbers may be due to a combination of effects. The small relative magnitude of the streamwise vorticity eigenmode, combined with the showtwave cutoff in β, implies that the instability would saturate before non-linear processes take over. Therefore, as with two-dimensional subharmonic modes, as M_∞ increases, the subharmonic instabilities do not trigger interactions between neighboring vortices.

3-D Fundamental Modes

These modes have the same periodicity in the streamwise direction as the base flow. For finite β the spanwise vorticity eigenmode is anti-symmetric about its center, and remains so even as M_∞ is increased; figure 3.10. This implies that the instability causes a net translation of the vortex cores, up and to the right at spanwise locations $\beta z = 0, \pm 2\pi ...$, rather than a bulging. A fundamental mode with no spanwise variation is neutrally stable, and shifts the vortex row an infinitesimal distance. For these reason, PW labeled this mode the translative instability.

The linear incompressible mechanism by which regions of two-dimensional elliptical streamlines can generate three dimensional flows is denoted the *elliptical instability*. It's localized in the vortex core, with growth rates tending to a finite value as the wavelength along the vortex axis tends to zero; Pierrehumbert [71], Bayly [2]. In viscous flows this inviscid mechanism leads to real vortex instability, with a short wavelength cutoff imposed by the action of viscosity, Landman & Saffman [40]. The instability allows the vorticity to stay in the stretching direction, as a result of an exact cancellation of the various tilting terms, leading to an exponential growth rate equal to the strain rate of the base flow, Waleffe [91], and may exist in a relatively unaltered state in compressible subsonic gases, where the growth rates and eigenmodes depend only on the local velocity gradient tensors of the basic flow, Lifschitz & Hameiri [46]. Thus, the translative mode's structure, figure 3.10, and growth rates, figure 3.11, link it to an instability of the elliptical type. It's unique to non-parallel flows, for parallel or near parallel flows it's not present, or weakly amplified.

The normalized strain, $s_c(\pi, 0)/\frac{1}{2}\omega(\pi, 0)$, of the unperturbed vortex cores yields a measure of the local ellipticity of the CSV streamlines. A value of zero gives locally circular streamlines, while a value of one implies infinite ellipticity, that is a locally plane Couette flow. The agreement between growth rates from the translative instability, parameterized by the normalized strain, and from pure elliptical flows is marginal, figure 3.11(d). However, this may explain why the translative instability shows little damping with increased levels of compressibility. For case C runs, with $M_\infty > 0.2$, this mode represents the most unstable perturbation to the CSV.

PW speculated that the deposition of streamwise vorticity, by the eigenmodes and a tilting process induced by the base flow, would lead to the creation of counter rotating streamwise vortices. Sandham & Reynolds [86] simulated a translative type instability and showed how the straining field of this type of instability can pull the vorticity into the braid regions, leading to the formations of streamwise vortices, Lin & Corcos [48]. A feature necessary for a streaky streamwise structure to occur is a single dominant spanwise wavenumber emerging from a random perturbation. As M_∞ increases figure 3.11 implies that this scenario is highly unlikely. It is not clear that a superposition of many translative instabilities, with the same growth rate but different spanwise wavelengths, could produce a coherent three-dimensional structure.

3.3.3 Comparison with experiment

In incompressible flows, large eddies play an important role in both entrainment and in determining the growth rates of the shear layer through pairings and amalgamations. For the CSV, the pairing type instabilities maximize at subharmonic streamwise wavelengths over the entire M_∞ range. However, their ability to trigger interactions between neighboring vortices becomes very much depreciated as the convective Mach number is increased. This is consistent with visualizations from Papamoschou & Bunyajitradulya [67], who for $M_c > 0.5$, find no evidence of pairing in their compressible

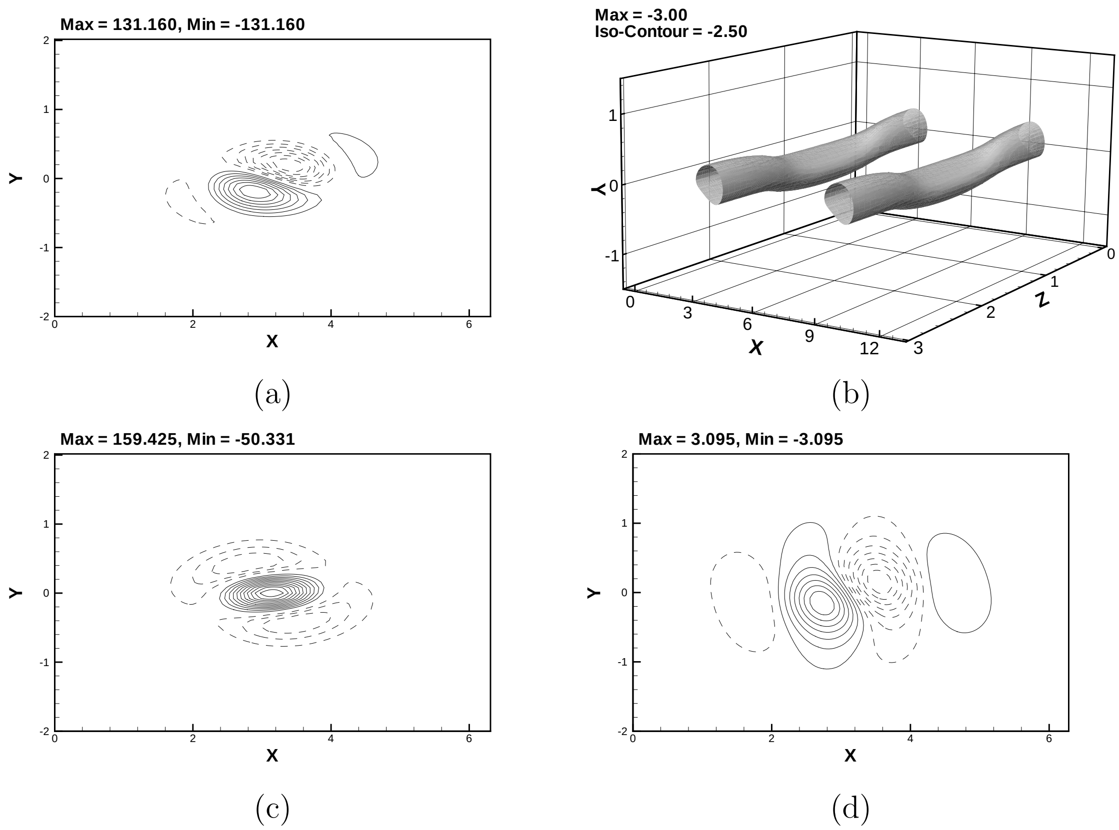

Figure 3.10: Translative instability eigenmodes, $\beta = \beta_{max} = 2.226$, $M_\infty = 0.61$, $\epsilon = 0.8871$. A full period is shown in all cases. (a): Spanwise vorticity perturbation. (b): Base vorticity plus spanwise perturbation with amplitude chosen so that its max is 20% that of the base flow. (c): Streamwise vorticity perturbation. (d): Density eigenmode.

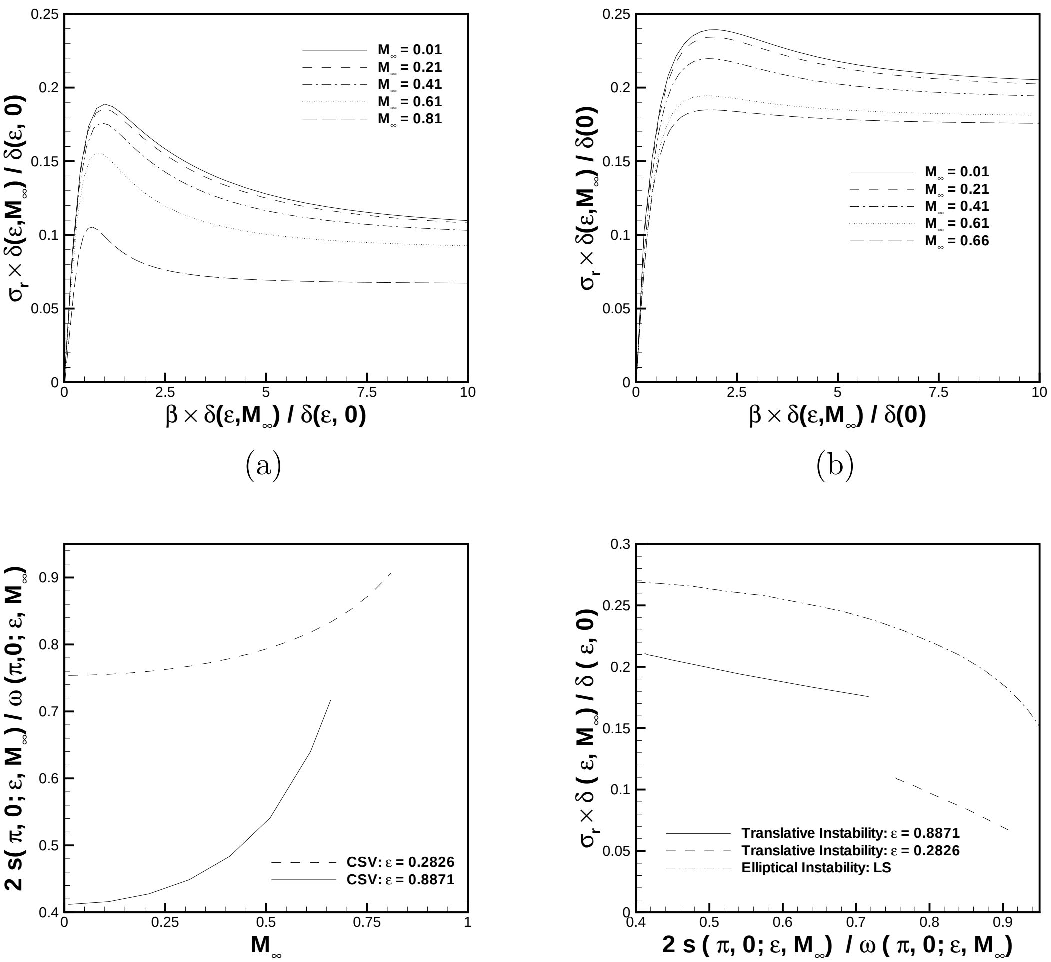

(a) (b) (c) (d)

Figure 3.11: 3-D translative instability growth rates, computed at various values of M_∞, $\alpha = 0.0$. (a): $\epsilon = 0.2826$, (b): $\epsilon = 0.8871$, (c): Normalized vortex core strain versus M_∞. (d): Growth rates of the translative instability, where $\beta \times \delta(\epsilon, M_\infty)/\delta(\epsilon, 0) = 10$, compared to those from an elliptical instability plotted against the normalized strain rate, LS $\rightarrow$ [40].

shear layers. They also speculate that the lack of organization in both the side and plan views suggests the coexistence of both two and three dimensionalities in the flow. Again this is consistent with the picture obtained from the CSV, where the growth rates of the pairing, helical pairing and translative modes are very similar over much of the Mach number range.

Stability analysis of parallel base flows suggests that at a given Mach number there is one spanwise wavelength which has maximum amplification. However, the plan views from Papamoschou & Bunyajitradulya [67] show that the chaotic patterns reveal every possible oblique angle to the free stream flow. A possible explanation for this may be found in figures 3.12(a), 3.8 and 3.11. These suggest that the range of spanwise wavenumbers with similar growth rates is quite large. Indeed for the higher Mach number case C runs the growth rates for the translative instability reduce by as little as 5% from its maximum value as the spanwise wavenumber increases by a factor of five.

In order to compare data from different experiments, the growth rates obtained must be normalized by the growth rates of an incompressible shear layer with the same density and velocity ratios. A variety of models, containing one or more free parameters, have been used for this purpose; Bogdanoff [8], Ragab & Wu [73], Clemens & Mungal [21], Slessor *et al.* [89]. These different normalization methods, combined with a non-injective density ratio to convective Mach number relationship, lead to substantial scatter in experimental growth rate data. The normalized growth rate trends for the three different mass fluxes investigated, as a function of M_c, are shown with results from various experimental investigations in figure 3.12. At any given M_c, the scaled growth rates from the CSV stability calculation lie in the mid to high range of the various experimental results. We remark that the present study yields temporal linear growth rates, whereas experiments measure the spatial growth of the mixing layer. Our results and those of Papamoshcou & Bunyajitradulya [67] indicate a distinct lack of interaction between eddies in supersonic shear layers. Their slow evolution may be due a combinations of decreased growth rates and this lack of interaction. Whatever the reason it is difficult to see their importance in governing

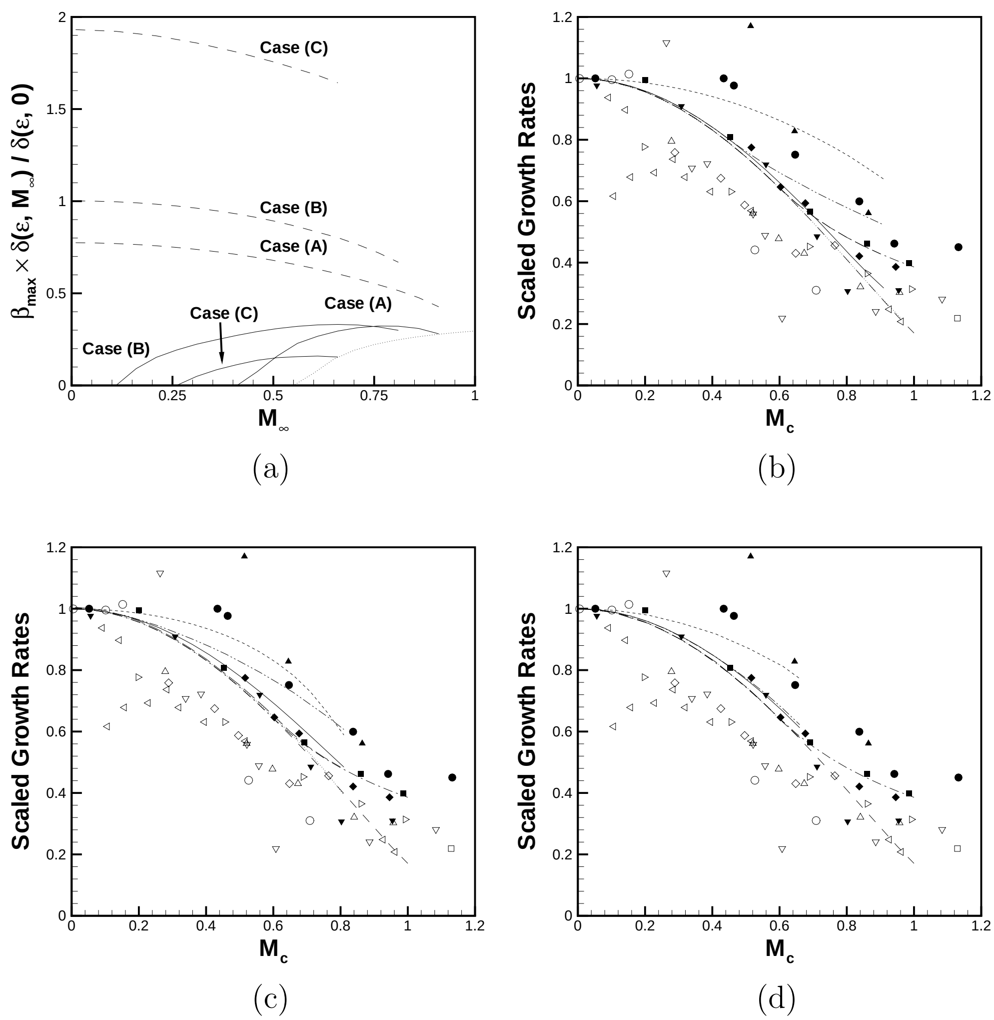

Figure 3.12: (a): $\beta_{max} \times \delta(\epsilon, M_\infty)/\delta(\epsilon, 0)$ vs M_∞. Solid lines represent the 3-D helical pairing instability. Dashed lines represent the 3-D translative instability. Dotted line for the 3-D parallel instability, $\epsilon = 0.0$ (b): Case A. (c): Case B. (d): Case C. Figure (b), (c) and (d) plot legend, □ [87], △ [19] (S & CM), ▽ [69], ▷ [26] (S), ◁ [28], ♢ [21], ○ [88], ■ [26] (CM), ▲ [83], ▼ [68] ♦ [19](RW), ● [66], dashed: CD 2-D modes, dash-dot: CD 3-D modes, solid: CSV 2-D pairing, dotted: CSV 2-D parallel, dash-dot-dot: CSV 3-D helical pairing, long-dash: CSV 3-D parallel, short-dash: CSV 3-D translative. Initials after the experimentalists name, indicate by whom the results have been normalized. S→Slessor, CM→Clemens and Mungal, RW→Ragab and Wu.

the entrainment process in supersonic shear layers.

3.4 Interpretation and remarks

The link between the linear stability of the CD profile and the steady CSV base flow, established in section 2.2, partially motivates the extension of the theory of stability of plane parallel flows to include the stability of the spatially nonuniform CSV states themselves. This has been done presently using a spectral-collocation method. As a physical model for the dynamics of compressible shear layers, the CSV structure is not without limitations, principally, that for a fixed mass flux within a vortex core, the homentropic solution branch terminates at a subsonic free stream Mach number. Thus, while the CSV state cannot apparently be extended to supersonic free-stream flow, it nonetheless provides a useful base-state for assessing the effect of compressibility on the stability properties of nonuniform compressible flows.

Three main classes of instabilities on the CSV were investigated; subharmonic, translative and a new parallel mode, each within the parameter space of the free-stream Mach number, the finite mass flow inside a closed vortex core and the wavenumber space of the perturbations. For any value of spanwise wave number it was found that the largest of the eigenvalues maximizes at either subharmonic or fundamental streamwise frequencies. The parallel instability which might be interpreted physically as having initiated a primary roll up producing a CSV-like structure, remains active and relatively unaltered. The persistence of this instability for the strongly nonlinear CSV flows may explain the success of linear growth rates, obtained from parallel shear flows, in postdicting experimentally observed growth rates in the compressible turbulent mixing layer.

In agreement with Pierrehumbert & Widnall [72], we found that for low Mach numbers the subharmonic mode has its greatest growth rate for eigenmodes with no spanwise variation, where it can be linked to an instability of the pairing type. As the Mach number increases this perturbation becomes three dimensional and the term pairing instability no longer applies, since it can no longer be interpreted as an initiating mechanism for interactions between neighboring vortices. This is in agreement with experimental observations that the structures in compressible shear layers are largely inert. Not only do the subharmonic instabilities loose their ability to pair neighboring vortices at higher Mach numbers, but this instability becomes sub-dominant to the more vigorous translative instability. The translative instability shows a broadband nature with respect to spanwise wave numbers. This can be interpreted to be compatible with experimental observations, where structures at every possible oblique angle are observed.

Finally, the growth of non-homentropic disturbances to non-parallel base flows may be important. These may be investigated using a CSV constructed using a homenthalpic continuation to finite M_∞ of the incompressible Stuart vortex. The entropy equation does not decouple from the system represented by (3.3)-(3.7), which may be physically relevant if the initial disturbances to experimental compressible shear layers were not approximately homentropic.

Chapter 4 Transonic flow in an array of counter-rotating vortices

Numerical solutions to the steady compressible Euler equations corresponding to a compressible analogue of the Mallier & Maslowe [51] vortex (a periodic array of counter-rotating vortices parameterized by the mass flow rate between adjacent cortex cores) are presented. The appropriate steady compressible Euler equations are derived for homentropic flow using a stream-function density formulation. These equations are solved using a spectral method, thereby continuing the Mallier & Maslowe vortex to finite c_∞, where c_∞ is defined as the sound speed at infinity. This is called the compressible Mallier & Maslowe vortex, and may be viewed as a crude model for the counter-rotating vortices arising from the single- and multi-mode Richtmyer-Meshkov instability. A solution branch is parameterized by the inverse of the sound speed at infinity, c_∞^{-1}, and the mass flow rate of the corresponding incompressible solution. Two methods for continuing the Mallier & Maslowe vortex to finite c_∞ are proposed. The first approach is to hold the mass flow rate fixed at its incompressible value as c_∞^{-1} is increased. The second is to compute the mass flow rate as part of the overall solution, so that it is allowed vary along a solution branch. It was found necessary, for well-posedness, to introduce an eigenvalue into the vorticity and energy equations for the stream-function and density, equivalent to Meiron, Moore & Pullin's [52] non-linear eigenvalue when extending the Stuart [90] vortex to the compressible regime. An extra construction parameter, unique to the CMMV, was required to maintain a constant circulation for each vortex as c_∞^{-1} was increased. All solution branches followed numerically were found to terminate at a finite value of c_∞^{-1}, where numerical evidence for the existence of large regions of smooth, steady, supersonic flow is presented.

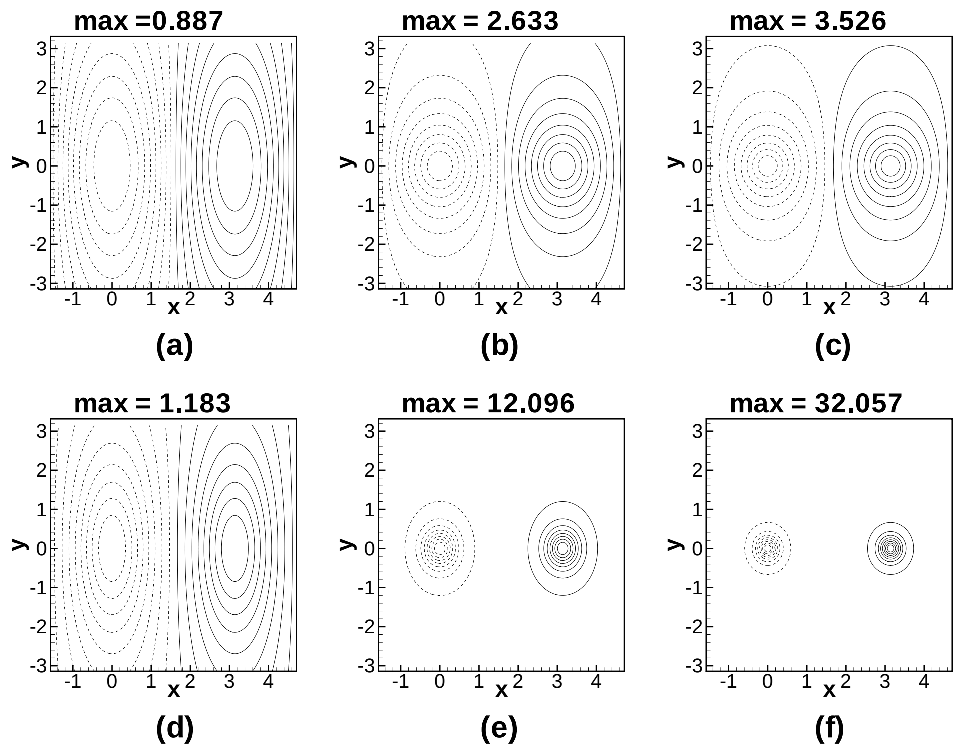

Figure 4.1: Stream-function $\psi_0(x,y)$: (a)$\kappa = 1.10$, (b)$\kappa = 2.0$, (c)$\kappa = 3.0$. Vorticity $\omega(x,y)$: (d)$\kappa = 1.10$, (e)$\kappa = 2.0$, (f)$\kappa = 3.0$. Dashed lines imply negative contours.

4.1 Mallier & Maslowe vortex

Mallier & Maslowe [51], henceforth referred to as MM, proposed an exact nonlinear, steady solution to the incompressible two-dimensional Euler equations, representing a periodic row of counter-rotating vortices. The MM vortex is a model of the longitudinal vortices which have been observed in boundary layers and two-dimensional Poiseuille flows. The periodic direction is denoted x, with y as the transverse coordinate. For a steady, two-dimensional, inviscid, incompressible flow the velocity field, $\mathbf{u}(x,y)$, and vorticity, $\omega(x,y)$, may be represented using a stream-function $\psi(x,y)$;

$$u = \frac{\partial \psi}{\partial y}, \quad v = -\frac{\partial \psi}{\partial x}, \quad \omega = -\nabla^2 \psi. \tag{4.1}$$

κ	s_n	E
1.10	-3.52088×10^{-1}	5.76083
2.00	-7.13227×10^{-2}	1.33272
3.00	-5.64881×10^{-2}	1.11974

Table 4.1: Normalized strain and aspect ratio for the solutions shown in figure 4.1

The vorticity is chosen to be a function of ψ alone, which satisfies the requirement that any steady solution of the incompressible Euler equations has constant vorticity along path-lines. The MM vortex corresponds to the choice

$$\nabla^2\psi = -\frac{1}{2\kappa^2}\sinh(2\psi), \tag{4.2}$$

where $1 \leq \kappa < \infty$ is a parameter defining the family. This is a form of the sinh-Gordon equation (Stuart's [90] solution satisfies Liouville's equation) where the family of exact solutions are given by

$$\psi_0(x,y) = \log\left(\frac{\kappa\cosh\left(\frac{\sqrt{\kappa^2-1}}{\kappa}y\right) - \sqrt{\kappa^2-1}\cos(x)}{\kappa\cosh\left(\frac{\sqrt{\kappa^2-1}}{\kappa}y\right) + \sqrt{\kappa^2-1}\cos(x)}\right). \tag{4.3}$$

By construction the flow is 2π periodic in x, and the total circulation, Γ_v, associated with each vortex is independent of κ and equal to 4π. As κ increases the core size decreases, implying the maximum vorticity must increase to conserve circulation. When $\kappa \to \infty$, ψ_0 can be shown to describes the potential flow produced by an array of counter-rotating point vortices, while $\kappa = 1$ represents fluid at rest.

The iso-contours of the stream-function and vorticity are elliptical, figure 4.1, with their major axis oriented in the vertical direction. Increasing κ decreases the ellipticity of the vortices. The vortex cores are located at the points $x = n\pi$, n integer. The stream-function at these points may be characterized by the strain, $s_0(n\pi, 0; \kappa)$, and vorticity, $\omega_0(n\pi, 0; \kappa)$, there

$$\psi_0(n\pi,0) \sim -\left(\frac{1}{2}\omega_0(n\pi,0) - s_0(n\pi,0)\right)x^2 - \left(\frac{1}{2}\omega_0(n\pi,0) + s_0(n\pi,0)\right)y^2. \tag{4.4}$$

For an elliptical stagnation point the condition $|s_0| < \frac{1}{2}|\omega_0|$ must be satisfied. The normalized strain yields a measure of the local ellipticity of the stream-lines

$$s_n = \frac{2s_0(n\pi, 0)}{\omega_0(n\pi, 0)}, \qquad -1 \leq s_n \leq 0. \tag{4.5}$$

Zero gives locally circular streamlines, while a value of -1 implies infinite ellipticity. The ratio of minor to major axis is,

$$E = \sqrt{(\frac{1}{2}\omega_0 - s_0)/(\frac{1}{2}\omega_0 + s_0)}, \qquad 1 \leq E < \infty. \tag{4.6}$$

Table 4.1 gives the normalized strain and ellipticity for the representative values of κ shown in figure 4.1.

4.2 Compressible formulation

The governing equations are the compressible Euler equations:

$$\begin{aligned} \boldsymbol{\omega}^* \times \mathbf{u}^* &= -\nabla\left(\frac{1}{2}\mathbf{u}^{*2}\right) - \frac{1}{\rho^*}\nabla p^*, && (4.7)\\ \nabla \cdot (\rho^* \mathbf{u}^*) &= 0, && (4.8)\\ (\mathbf{u}^* \cdot \nabla)\, s^* &= 0, && (4.9) \end{aligned}$$

where $\mathbf{u}$, $\boldsymbol{\omega}$, ρ and p denote fluid velocity, vorticity, density, and pressure, respectively and '*' indicates a dimensional quantity. Equation (4.9) states that entropy is conserved along streamlines. For a calorically perfect gas, the equation of state is

$$\frac{p^*}{p_r^*} = \left(\frac{\rho^*}{\rho_\infty^*}\right)^\gamma \exp\left(\frac{s^* - s_\infty^*}{c_v}\right), \qquad \gamma = \frac{c_p}{c_v}, \tag{4.10}$$

where c_v, c_p are the constant specific heats and the subscript ∞ refers to uniform reference quantities as $y \to \pm\infty$, where the flow is stationary. The reference pressure is $p_r^* = u_v^{*2}\rho_\infty^*$, with the characteristic vortex velocity defined as $u_v^* = \Gamma_v^*/l^*\Gamma_v$. Γ_v is the circulation of an individual vortex, which is held constant by construction.

In the following, fluid quantities are made non-dimensional against these reference values, and entropy is scaled against c_v. The reference free stream sound speed is

$$c_\infty = \left(\frac{\gamma\, p_\infty}{\rho_\infty}\right)^{1/2}. \tag{4.11}$$

For the incompressible MM vortex the mass flow rate, ϵ, between adjacent vortices can be defined in terms of κ,

$$\epsilon = \psi_0(\pi, 0) - \psi_0(0, 0) = 2 \log\left(\frac{\kappa + \sqrt{\kappa^2 - 1}}{\kappa - \sqrt{\kappa^2 - 1}}\right) \qquad \Longrightarrow \qquad \kappa = \cosh\left(\frac{\epsilon}{4}\right), \tag{4.12}$$

where $0 \leq \epsilon < \infty$. The main idea is to write the steady Euler equations for plane compressible flow in terms of a stream-function, ψ, and density, ρ. Writing $\boldsymbol{\omega} = \omega(x, y)\mathbf{k}$, where $\mathbf{k}$ is taken to be a unit vector in the span-wise direction, and satisfying the continuity equation by introducing the stream-function

$$\rho u = \frac{\partial \psi}{\partial y}, \qquad \rho v = -\frac{\partial \psi}{\partial x}, \tag{4.13}$$

the vorticity can be written as

$$\omega(x, y) = -\frac{1}{\rho}\, \nabla^2 \psi + \frac{1}{\rho^2}\, \left(\nabla \psi \cdot \nabla \rho\right). \tag{4.14}$$

The entropy equation is satisfied by $s = s(\psi)$. Using the total enthalpy

$$h = \frac{1}{2}\mathbf{u}^2 + \frac{c_\infty^2}{(\gamma - 1)}\, \frac{p}{\rho}, \tag{4.15}$$

and the equation of state, together with thermodynamic relations, equation (4.7) may be rewritten as

$$\boldsymbol{\omega} \times \mathbf{u} = -\nabla h + \frac{c_\infty^2}{\gamma\,(\gamma - 1)}\, \tau\, \nabla s. \tag{4.16}$$

To proceed further requires a closure relationship connecting s, h and ψ. In general this is arbitrary, but two choices are $s = const$, $h = h(\psi)$ (homentropic flow), and $h = const$, $s = s(\psi)$ (homenthalpic flow). We choose to use a homentropic continuation, for which (4.14) and (4.16) can be written, after some algebra, as

$$\frac{1}{\rho^2}\nabla^2\psi - \frac{1}{\rho^3}\left(\nabla\psi\cdot\nabla\rho\right) = \frac{dh}{d\psi} \equiv -V(\psi), \tag{4.17}$$

where $V(\psi) = \omega/\rho$, is a function to be specified. A second equation may be obtained from relation (4.15) by writing this equation in terms of ψ and ρ to give,

$$\frac{1}{\rho^2}\left(\nabla\psi\right)^2 + c_\infty^2\,\frac{\rho^{\gamma-1}}{\gamma-1} = h_\infty - \int_\infty^\psi V(\psi')\,d\psi'. \tag{4.18}$$

It remains to specify a functional form for $V(\psi)$. In order to obtain MM's solution as $c_\infty^{-1} \to 0$ we choose

$$V(\psi) = \frac{\Gamma_c}{2\cosh^2\frac{\epsilon}{4}}\sinh(2\mu\psi) \tag{4.19}$$

where μ and Γ_c are to be found as part of the solution; of course $\mu \to 1$ and $\Gamma_c \to 1$ as $c_\infty^{-1} \to 0$. The parameter μ is necessary for well-posedness, while Γ_c is a construction parameter introduced so that the circulation can be held constant. The homentropic equations for momentum and energy may now be written in the following compact form

$$\begin{aligned}
\nabla^2\psi - \frac{1}{\rho}\left(\nabla\psi\cdot\nabla\rho\right) &= -\frac{\rho^2\Gamma_c}{2\cosh^2\frac{\epsilon}{4}}\sinh(2\mu\psi), &(4.20)\\
\frac{1}{2c_\infty^2}\left(\nabla\psi\right)^2 + \frac{\rho^2\left(\rho^{\gamma-1}-1\right)}{\gamma-1} &= \frac{\rho^2\Gamma_c}{4\mu c_\infty^2\cosh^2\frac{\epsilon}{4}}\left(1-\cosh(2\mu\psi)\right). &(4.21)
\end{aligned}$$

On the semi-infinite rectangle, $\mathcal{R} = \{(x,y) : -\pi/2 \le x \le \pi/2,\ 0 \le y < \infty\}$, the boundary conditions are

$$\begin{array}{llll}
\dfrac{\partial\psi}{\partial y} = 0 & \text{on} & (y = 0, -\pi/2 \le x \le \pi/2), & \\
\dfrac{\partial\psi}{\partial x} = 0 & \text{on} & (x = \pm\pi/2, 0 \le y \le \infty), & \\
\psi \to 0 & \text{as} & y \to \infty, \quad -\pi/2 \le x \le \pi/2, & \\
\rho \to 1 & \text{as} & y \to \infty, \quad -\pi/2 \le x \le \pi/2, &
\end{array} \tag{4.22}$$

To characterize solutions to (4.20)-(4.21) requires two further conditions. The first is a constraint on the total dimensionless circulation,

$$\int_{\mathcal{R}} \omega(x,y)\,dx\,dy \equiv \frac{\Gamma_c}{2\cosh^2\frac{\epsilon}{4}} \int_{\mathcal{R}} \rho(x,y)\sinh\Big(2\mu\psi(x,y)\Big)\; dxdy = -2\pi. \tag{4.23}$$

The second is a constraint on ψ and can be formulated in two ways.

Formulation A: The mass flux along a solution branch is held constant at its initial incompressible value, ϵ, as c_∞^{-1} is increased,

$$\psi(\pi,0) - \psi(0,0) = \epsilon. \tag{4.24}$$

Formulation B: The mass flux along a solution branch can vary, and must be found as part of the solution.

$$\psi(\pi,0) - \psi(0,0) = \epsilon\Gamma_c \tag{4.25}$$

Note, ϵ is constant along a branch, but the mass flux is now $\epsilon \times \Gamma_c$. Solution branch B will be different to solution branch A as ϵ appears non-linearly in the vorticity and enthalpy equations and the circulation constraint. Treating the mass flux in this way produces an alternate, independent set of governing equations.

The unknowns are $\psi(x,y;c_\infty^{-1},\epsilon)$, $\rho(x,y;c_\infty^{-1},\epsilon)$, $\mu(c_\infty^{-1},\epsilon)$, and $\Gamma_c(c_\infty^{-1},\epsilon)$.

4.3 Numerical method

A spectral collocation method, similar to that used by MMP, was employed to solve the boundary-value problem defined by equations (4.20), (4.20), (4.23) and one of

(4.24) or (4.25). To start, ψ and ρ were written as

$$\begin{aligned}\psi &= \sum_{n=0}^{N-1}\sum_{m=0}^{M-1} a_{mn}\cos(mx)\Phi_{2n}(y)\\ \rho &= 1+\sum_{n=0}^{N-1}\sum_{m=0}^{M-1} b_{mn}\cos(mx)\Phi_{2n}(y),\end{aligned} \tag{4.26}$$

where a_{mn} and b_{mn} are coefficients to be determined. The functions $\Phi_n(y)$ are basis functions, which decay as $y \to \infty$. The interval $(0, 1)$ was stretched onto $(0, \infty)$ using the algebraic stretching, $Y = y/\sqrt{\eta^2 + y^2}$, where η is the stretching parameter. The functions $\Phi_n(y)$ are combinations of Chebyschev polynomials satisfying the boundary conditions. Letting $\phi_n(y(Y)) = T_n(Y)$, then $\Phi_n(y) = \phi_0(y) - \phi_{n+2}(y)$. The collocation points are $(x_i, y(Y_j))$, $i = 1, ...M$, $j = 1, ...N$, where x_i are the zeros of $\cos(Mx)$ between $-\pi/2$ and $\pi/2$, and Y_j are the zeros of $T_{2N}(Y)$ between 0 and 1.

Equations (4.26) were substituted into each of (4.20) and (4.21) and satisfied at the collocation points. This combined with equation (4.23) and one of (4.24) or (4.25) yielded $2 \times M \times N + 2$ nonlinear equations for the $2 \times M \times N + 2$ unknowns a_{mn}, b_{mn}, μ and Γ_c. The solution branches obtained using equation (4.24) as the mass flux constraint are denoted branches A, while those obtained using equation (4.25) are denoted branches B. These equations were solved by a standard Newton method with analytical evaluation of the Jacobian, which was full. All numerical solutions reported have residuals less that 10^{-10}.

4.4 Results

To continue the MM vortex to finite c_∞, ϵ was fixed and a numerical solution obtained for $c_\infty^{-1} = 0$ by using as an initial approximation a set of coefficients a_{mn} calculated using equation (4.3), $b_{mn} = 0$, $\mu = 1$ and $\Gamma_c = 1$. For formulation A, *the mass flux was held fixed*, as c_∞^{-1} was incrementally increased. Alternatively, for formulation B, ϵ *was held constant*, while the effective mass flux, $\epsilon \times \Gamma_c$, was solved for. The spectral solutions reported use $[M, N] = [40, 40], [60, 60]$, $\eta = 1.5$. The accuracy of the method

κ	$\lvert\Gamma_c(\kappa, c_\infty^{-1} = 0) - 1.0\rvert$	$\lvert\mu(\kappa, c_\infty^{-1} = 0) - 1.0\rvert$
1.05	2.77367×10^{-5}	2.33066×10^{-5}
1.10	2.90704×10^{-5}	2.12376×10^{-5}
1.25	3.01181×10^{-5}	1.64405×10^{-5}
1.50	2.77684×10^{-5}	1.41310×10^{-5}
2.00	2.10549×10^{-5}	6.41758×10^{-5}
3.00	1.23583×10^{-5}	2.85193×10^{-5}

Table 4.2: *Formulation A*. Error in the circulation constraint parameter, Γ_c, and the non-linear eigenvalue, μ: $[M, N] = [60, 60]$.

was tested by comparing numerical results with the analytical solution at $c_\infty^{-1} = 0$. Table 4.2 shows errors for formulation A, similar results were found for formulation B.

4.4.1 Solution technique A

Using formulation A solutions were obtained with $\kappa = 1.05, 1.10, 1.25, 1.50, 2.00, 3.00$, over a range of c_∞ varying from $c_\infty^{-1} = 0$ to a maximum value to be discussed. Figure 4.2 show contour plots of ψ,ρ, ω, $\nabla \cdot \mathbf{u}$ for $\kappa = 3.0$, $c_\infty^{-1} = 0.1686$. The local Mach number, M_l, is defined as

$$M_l = c_\infty^{-1} \left(\frac{(\frac{\partial \psi}{\partial x})^2 + (\frac{\partial \psi}{\partial y})^2}{\rho^{\gamma+1}} \right)^{\frac{1}{2}}. \tag{4.27}$$

The maximum Mach number, M_{max}, occurs on the symmetry line, $y = 0$, near the vortex core boundary where the vertical velocity is maximum, figure 4.3

The effect of increasing compressibility on the MM vortex *at fixed mass flux* is shown in figures 4.4-4.6. Plotted are $\mu(c_\infty^{-1}, \kappa)$ and $\Gamma_c(c_\infty^{-1}, \kappa)$ in figures 4.4 (a) and (b), $2s_c(n\pi, 0)/\omega(n\pi, 0)$ and M_{max} in figures 4.5 (a) and (b) and finally $\rho(n\pi, 0)$ and $\omega(\pi, 0)$ in figures 4.6 (a) and (b). The non-linear eigenvalue, μ, increases with increasing c_∞^{-1}, as does the absolute value of normalized strain. The straining field causes a net elongation of the vortex cores with increasing compressibility, thereby increasing the aspect ratio E, equation (4.6). The maximum vorticity at the core also

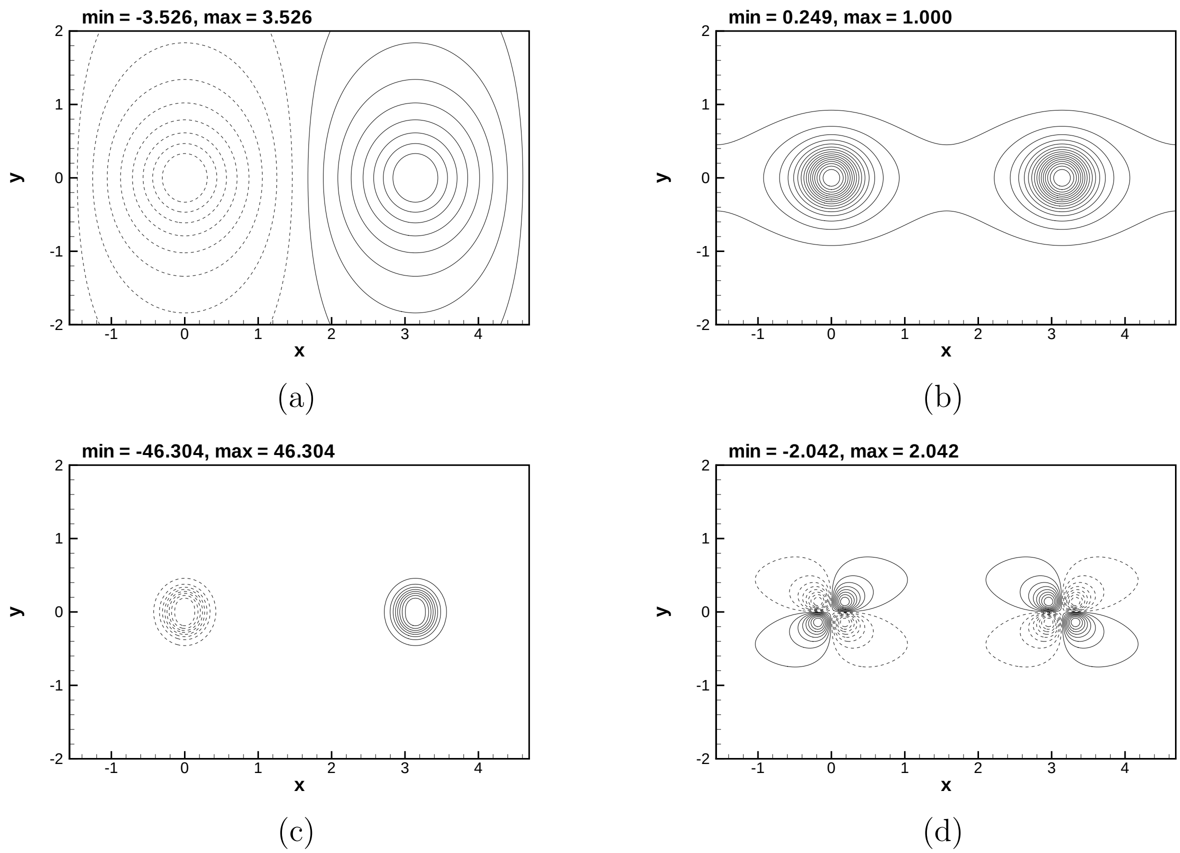

Figure 4.2: *Formulation A*, Compressible MM vortex; $\kappa = 3.0$, $c_\infty^{-1} = 0.1686$. (a) Stream-function. (b) Density. (c) Vorticity. (d) Dilatation.

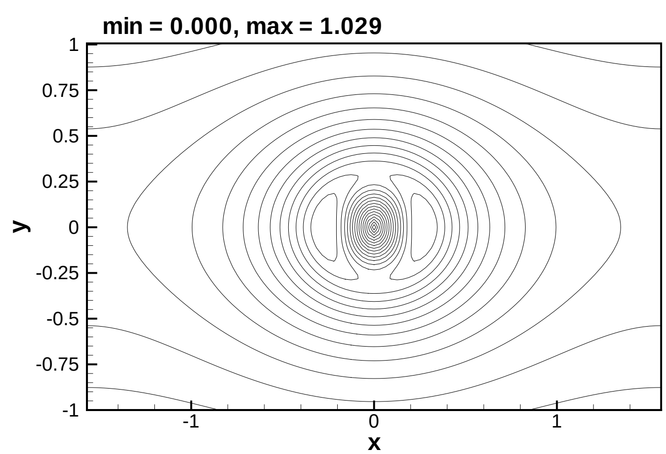

Figure 4.3: *Formulation A*. Contour of local Mach number, M_l; $\kappa = 3.00$, $c_\infty^{-1} = 0.1686$

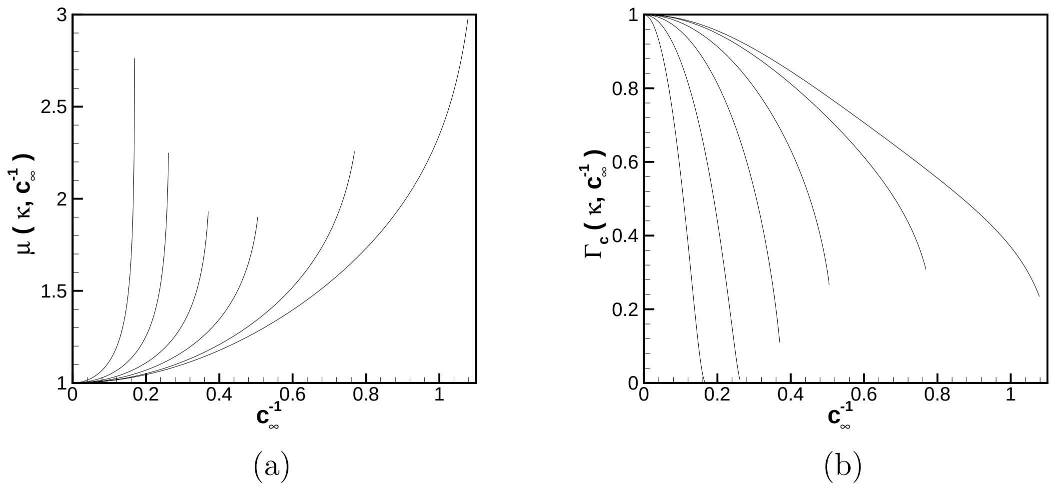

Figure 4.4: *Formulation A*. (a) Non-linear eigenvalue μ versus c_∞^{-1}. (b) Circulation constraint Γ_c versus c_∞^{-1}. $\kappa = 1.05$, 1.10, 1.25, 1.50, 2.00, 3.00, increasing right to left.

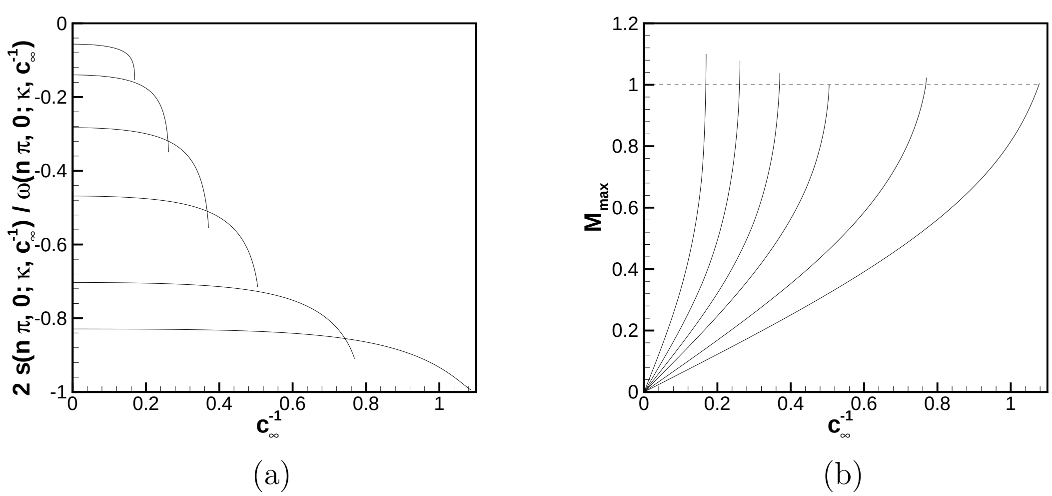

Figure 4.5: *Formulation A*. (a) Normalized strain versus c_∞^{-1}. (b) M_{max} versus c_∞^{-1}. Values of κ as in figure 4.4, κ increasing bottom to top in the first graph, and right to left in the second.

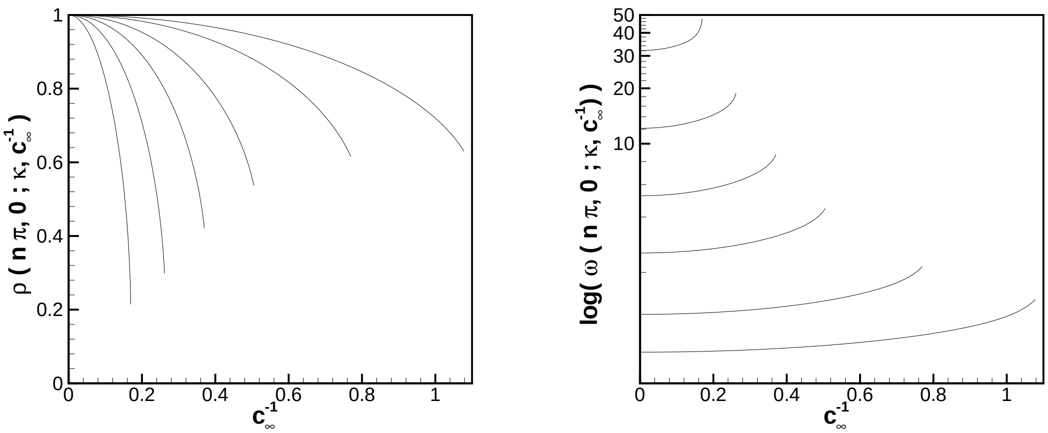

(a) (b)

Figure 4.6: *Formulation A*. (a) Minimum density versus c_∞^{-1}. (b) Maximum vorticity versus c_∞^{-1}. Values of κ as in figure 4.4, increasing right to left in the first graph and bottom to top in the second.

increases with c_∞^{-1}, implying that size of the vortex cores must decrease so that the circulation can remain constant. Γ_c and ρ decrease with increasing c_∞^{-1}. For $\kappa = 3.00$, the core density was seen to drop as low as 0.216 along that solution branch. For all values of κ investigated M_{max} becomes larger than unity above some critical value of c_∞^{-1}, the value of which depends on κ. This implies that for values of c_∞^{-1} greater than this critical value, the solutions contain locally smooth regions of supersonic flow on the vortex core boundaries, centered about $y = 0$.

4.4.2 Solution technique B

Using formulation B solutions were obtained with $\kappa = 1.10, 1.50, 2.00, 3.00, 5.00$, over a range of c_∞ varying from $c_\infty^{-1} = 0$ to a maximum value, which will be addressed later. Figure 4.7 show contour plots of ψ,ρ, ω, $\nabla \cdot \mathbf{u}$ for $\kappa = 5.0$, $c_\infty^{-1} = 0.3250$. The local Mach number is shown in figure 4.8, where it is evident that M_{max} is again achieved near the vortex core boundary, at $y = 0$. Note, the fields displayed in figures 4.2 and 4.7 produce the same maximum local Mach number, despite the fact that the vorticity, density and dilatational profiles are quite different. The

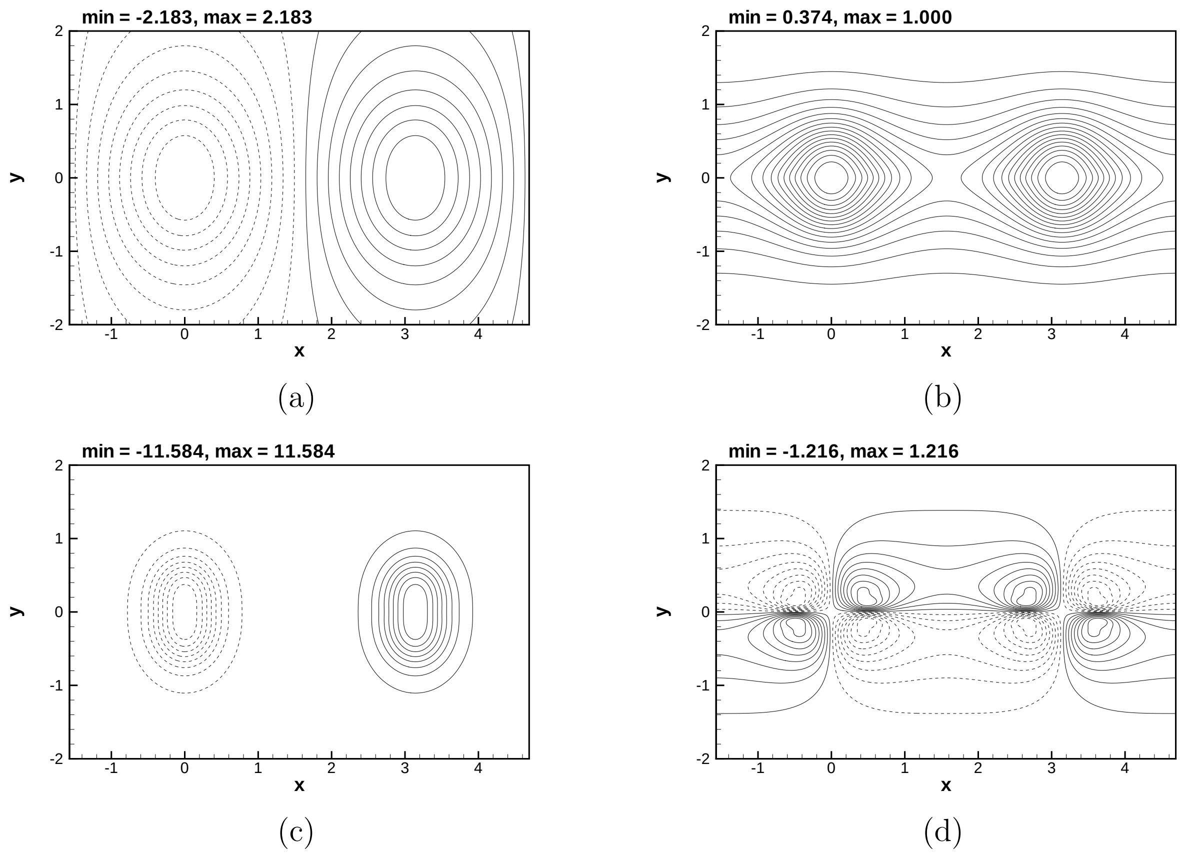

Figure 4.7: *Formulation B*. Compressible MM vortex; $\kappa = 5.0$, $c_\infty^{-1} = 0.3250$. (a) Stream-function. (b) Density. (c) Vorticity. (d) Dilatation.

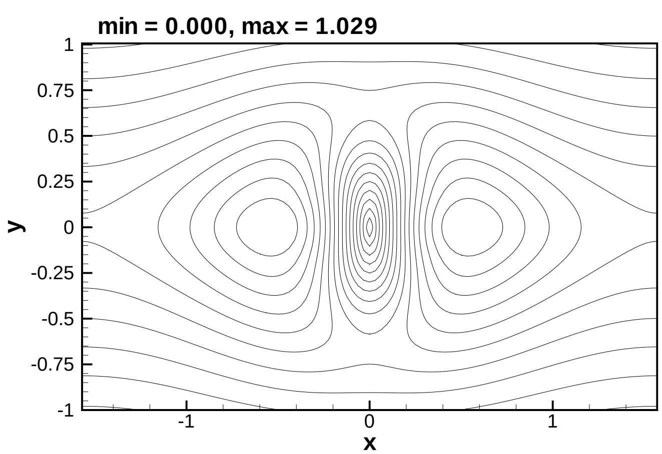

Figure 4.8: *Formulation B*. Contour of local Mach number, M_l; $\kappa = 5.00$, $c_\infty^{-1} = 0.3250$

effect of increasing compressibility on the MM vortex, *at fixed ϵ but variable mass flux*, is shown in figures 4.9-4.12. Plotted are $\mu(c_\infty^{-1}, \kappa)$ and $\Gamma_c(c_\infty^{-1}, \kappa)$ in figures 4.9 (a) and (b), $\Gamma_c(c_\infty^{-1}, \kappa) \times \epsilon(\kappa)$ and $\cosh(\Gamma_c(c_\infty^{-1}, \kappa) \times \epsilon(\kappa)/4)$ in figures 4.10 (a) and (b), $2s_c(n\pi, 0)/\omega(n\pi, 0)$ and M_{max} in figures 4.11 (a) and (b) and finally $\rho(n\pi, 0)$ and $\omega(\pi, 0)$ in figures 4.12 (a) and (b).

Clearly, there are marked differences between solutions obtained from formulations A and B. Increasing c_∞^{-1} decreases Γ_c, figure 4.9(b), which in turn decreases the effective mass flow rate between the vortex cores, figure 4.10(a). This leads to a very large increase in the absolute value of the normalized strain, 4.11(a), and so the vortices are stretched substantially in the vertical direction. In fact, along all the solution branches investigated the ellipticity, E, increased by at least a factor of five from its incompressible value. Figure 4.12(b) shows that the maximum value of vorticity, which is realized at the vortex cores, also decreases as c_∞^{-1} is increased (in contrast with results from formulation A). To maintain a constant circulation, the vortex cores become less compact, implying that the core density does not decrease as quickly when compared with results from formulation A, figures 4.6(a) and 4.12(a). Never the less, for formulation B the low density region inside the vortex cores extends further into the high velocity region between the cores. This process increasing the maximum local Mach number attainable.

Figure 4.11(b) shows that under formulation B, the onset of locally, smooth supersonic flow depends on κ. At low vales of κ, the flow remains entirely subsonic, and the the bound $|s_c(n\pi, 0)/\frac{1}{2}\omega(n\pi, 0)| < 1$, necessary for locally elliptical streamlines becomes close to being violated. Indeed for $\kappa = 1.10$, $c_\infty^{-1} = 2.00$, $s_c(n\pi, 0)/\frac{1}{2}\omega(n\pi, 0) = -0.993$. If this bound were broken, the stagnation points at the vortex cores would change in nature from elliptical to hyperbolic. In this regime, increasing compressibility causes the low mass flux of the initially incompressible solution to tend to zero, figure 4.10. The vortices become weaker and less compact, so that following this solution branch further would eventually lead to quiescent flow. For large values of κ above a critical c_∞^{-1}, the value of which depends on κ, the solutions admit the existence of smooth regions of supersonic flow on the vortex core

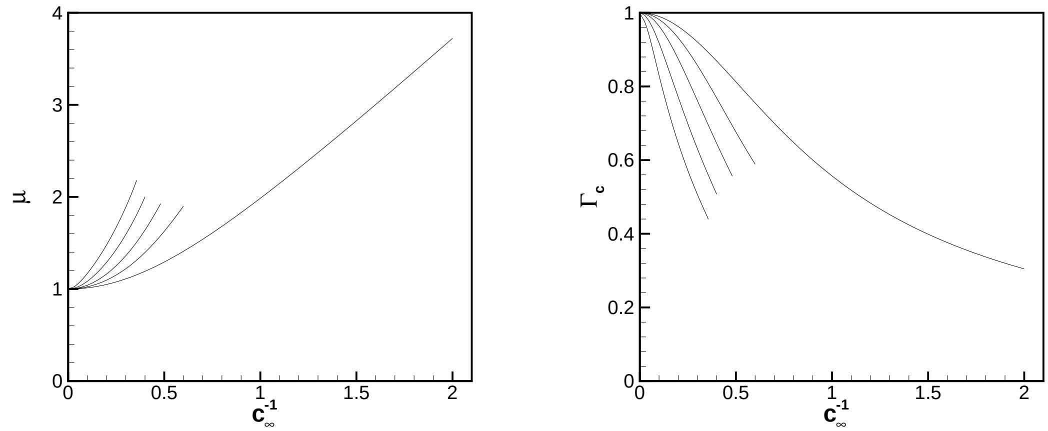

(a) (b)

Figure 4.9: *Formulation B.* (a) Non-linear eigenvalue μ versus c_∞^{-1}. (b) Circulation constraint Γ_c versus c_∞^{-1}. $\kappa = 1.10,\ 1.50,\ 2.00,\ 3.00,\ 5.00$, κ increasing right to left.

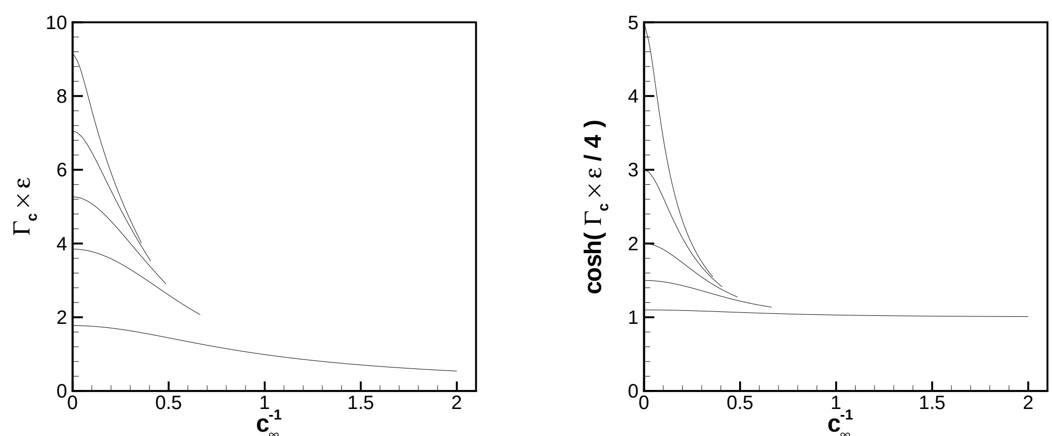

(a) (b)

Figure 4.10: *Formulation B.* (a) Effective mass flux $\epsilon \times \Gamma_C$ versus c_∞^{-1}. (b) $\cosh(\epsilon\Gamma_c/4)$ versus c_∞^{-1}. Values of κ as in figure 4.9, κ increasing bottom to top in both graphs.

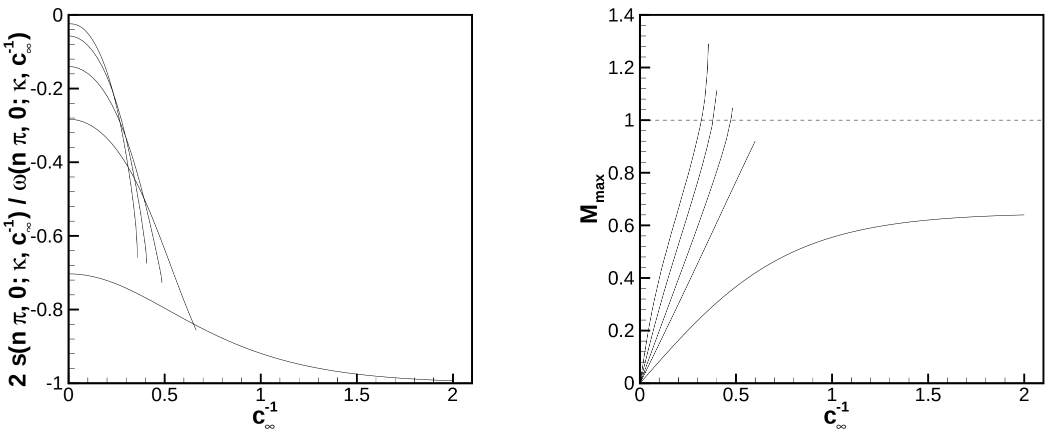

(a) (b)

Figure 4.11: *Formulation B.* (a) Normalized strain versus c_∞^{-1}. (b) M_{max} versus c_∞^{-1}. Values of κ as in figure 4.9, κ increasing bottom to top in the first graph, and right to left in the second.

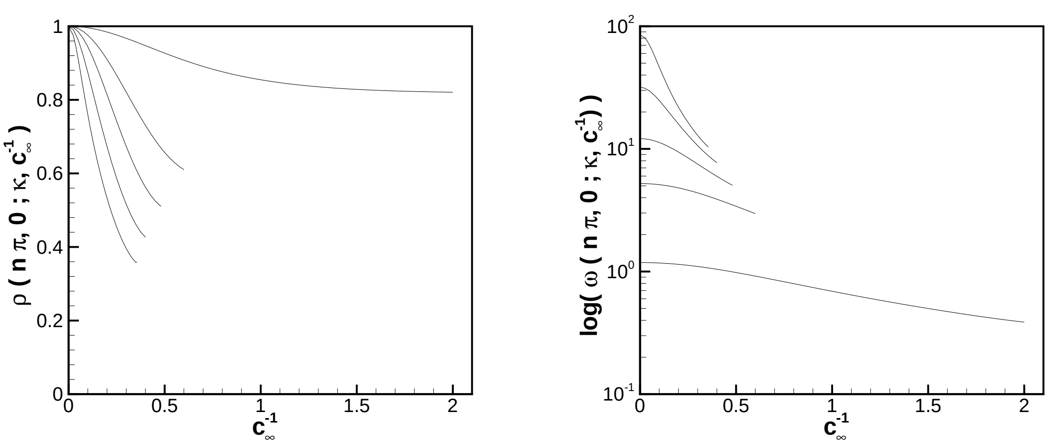

(a) (b)

Figure 4.12: *Formulation B.* (a) Minimum density versus c_∞^{-1}. (b) Maximum vorticity versus c_∞^{-1}. Values of κ as in figure 4.9, increasing top to bottom in the first graph and bottom to top in the second.

boundaries, centered about $y = 0$.

4.4.3 Convergence

To address the question of convergence, the decay of the coefficients a_{mn} and b_{mn} with respect to m was examined. The magnitude of the coefficients was assumed to have an exponential form;

$$|a_{mn}| \sim exp\left(\alpha_m(n;\kappa,c_\infty^{-1})m\right), \quad |b_{mn}| \sim exp\left(\beta_m(n;\kappa,c_\infty^{-1})m\right), \tag{4.28}$$

with n fixed. Exponential convergence is lost when any of the exponents pass through zero; $\alpha_n \geq 0$ or $\beta_m \geq 0$. Least-squares fits of $\log(|a_{mn}|)$ and $\log(|b_{mn}|)$ versus m was made for several values of n. The slopes of these fits give estimates of α_m and β_m, thus yielding a criterion on when convergence is lost. In general, a solution branch is said to terminate when the Newton method fails to find converged solutions along a particular branch. Nevertheless, for small values of κ (under formulation B) the convergence of the spectral series is not lost along a particular branch. These branches appear to lead to quiescent flow and do not to terminate due to loss of convergence. Figure 4.13 shows the spectral coefficients a_{mn} and b_{mn} for two case B runs at $[M, N] = [60, 60]$. There appears to be exponential decay, indicating convergence of the series (4.26). Figure 4.14 shows computed estimates of α_m and β_m, at several values of n, for solution branches from both formulation A and formulation B. Note that the range of m used to create these fits is parameter dependent.

Numerical solutions were obtained by continuing in c_∞^{-1} with fixed ϵ. In order to verify that branch termination was not a result of choice of c_∞^{-1} as a continuation parameter, arc-length continuation in the space of all unknowns was employed, which would allow the solution branch to negotiate a turning point without terminating. A fixed arc-length increment was used to initialize the iterative technique, and fourth order extrapolation in arc-length to estimate the next approximation. This gave no change in the value of c_∞^{-1} at which the Newton method failed to find converged solutions, and would indicate that the branch termination was genuine. Under for-

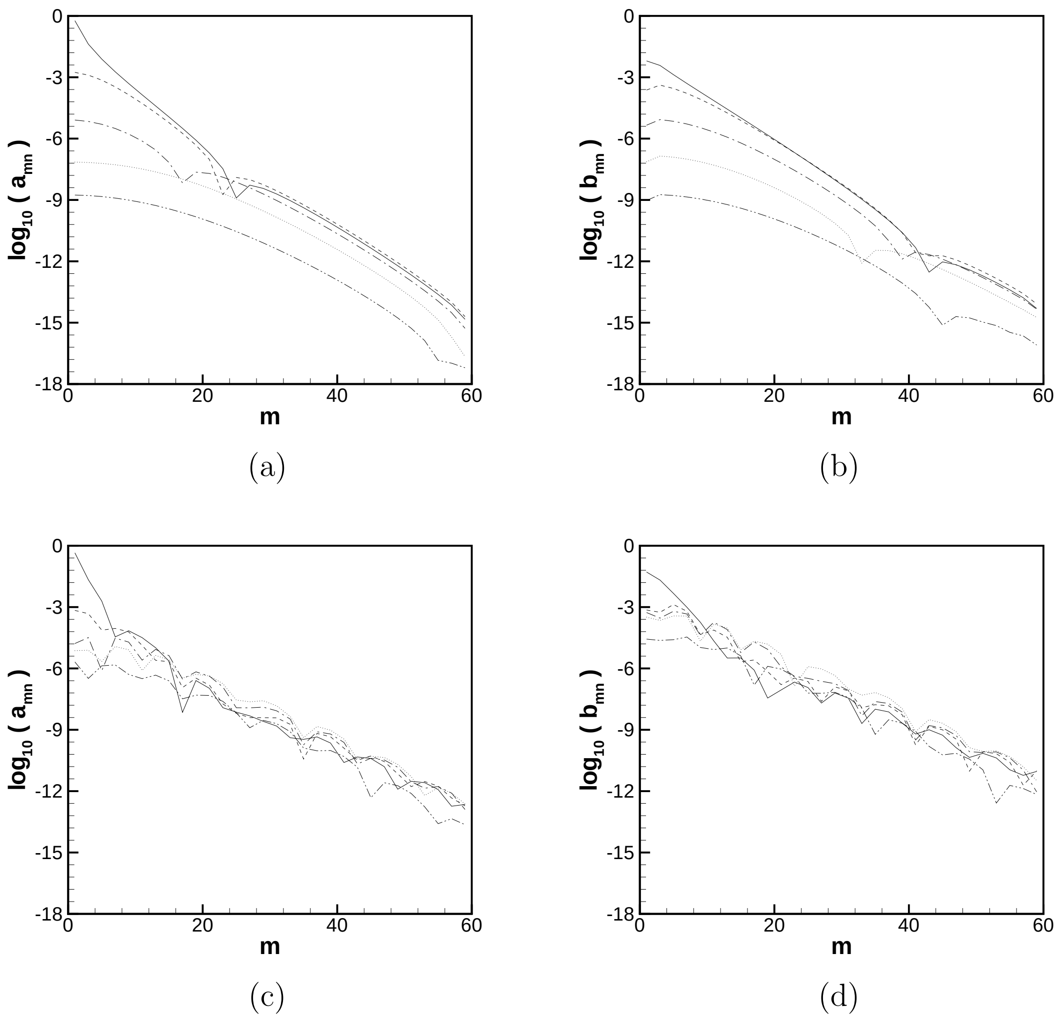

Figure 4.13: *Formulation B.* $\kappa = 5.00$, $c_\infty^{-1} = 0.200$: (a) $\log_{10} a_{mn}$ versus m. (b) $\log_{10} a_{mn}$ versus m. $\kappa = 5.00$, $c_\infty^{-1} = 0.325$: (a) $\log_{10} a_{mn}$ versus m. (b) $\log_{10} a_{mn}$ versus m. Plot legend n =0 (solid), 15 (dashed), 30 (dash-dot), 45 (dotted), 59 (dash-dot-dot).

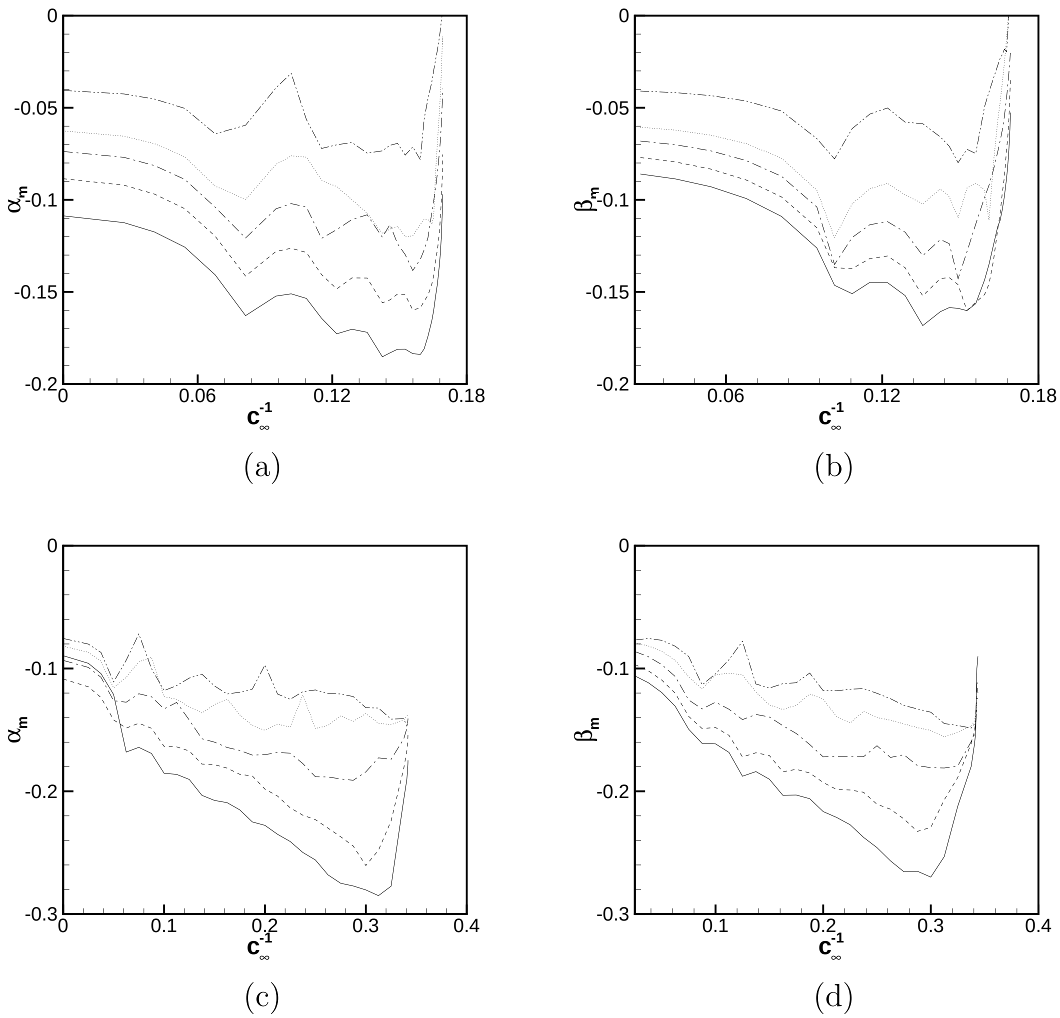

Figure 4.14: *Formulation A.* $\kappa = 3.00$: (c) α_m versus c_∞^{-1}. (d) β_m versus c_∞^{-1}. *Formulation B.* $\kappa = 5.00$: (c) α_m versus c_∞^{-1}. (d) β_m versus c_∞^{-1}. Plot legend n =0 (solid), 15 (dashed), 30 (dash-dot), 45 (dotted), 59 (dash-dot-dot).

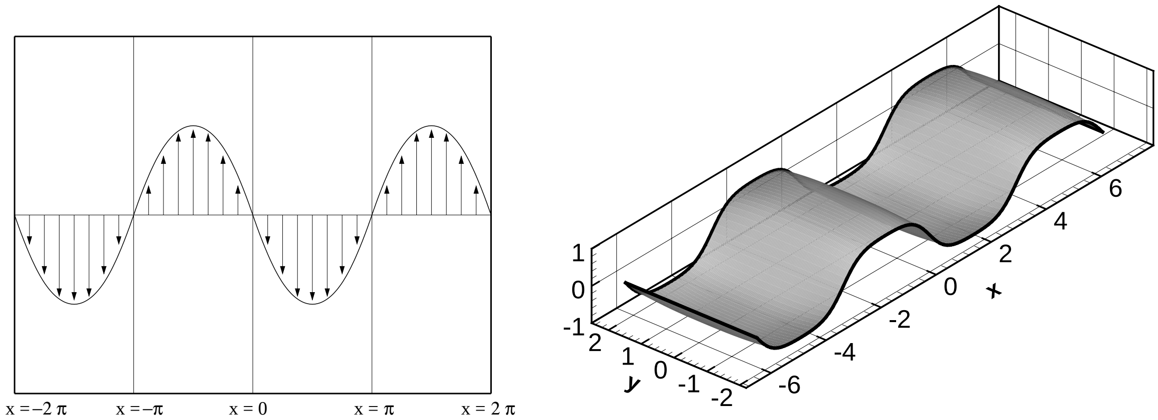

(a) (b)

Figure 4.15: *Formulation A.* (a) Graphical representation of the flow field for small κ close to branch termination. (b) $\kappa = 1.05$, $c_\infty = 1.08$, $v(x, y)$, computed vertical velocity.

mulation A all branches were found to terminate at a finite value of c_∞^{-1}, at which $M_{max} > 1$.

Locally parallel flows: The effect of the increasing strain rate with compressibility is most notable for small values of κ. It stretches the vortices in the vertical direction, increasing the local measure of ellipticity of the streamlines by an order of magnitude. Under formulation A, $\kappa = 1.05$ and $c_\infty^{-1} = 0.0$, $E = 10.700$, while $E = 364.980$ for the same value of κ but with $c_\infty^{-1} = 1.080$. Under formulation B, $\kappa = 1.10$ and $c_\infty^{-1} = 0.0$, $E = 5.735$, while $E = 295.708$ for the same values of κ but with $c_\infty^{-1} = 2.00$. The flow field approaches a locally parallel vertical shear flow, where the ratio of horizontal to vertical velocities goes to zero as the absolute value of the normalized strain approaches unity, figure 4.15.

Formulation A local supersonic flow: Figure 4.5(b) indicates that there exists a moderate combination of the parameters c_∞ and κ for which formulation A admits the existence of smooth transonic flow. For $\kappa = 3.0$, three-point interpolation gives $M_{max} = 1.00$ at $c_\infty = 0.1683$, where the coefficients a_{mn} and b_{mn} decay exponentially fast with respect to m, and the solution appears smooth. At this value of κ the final

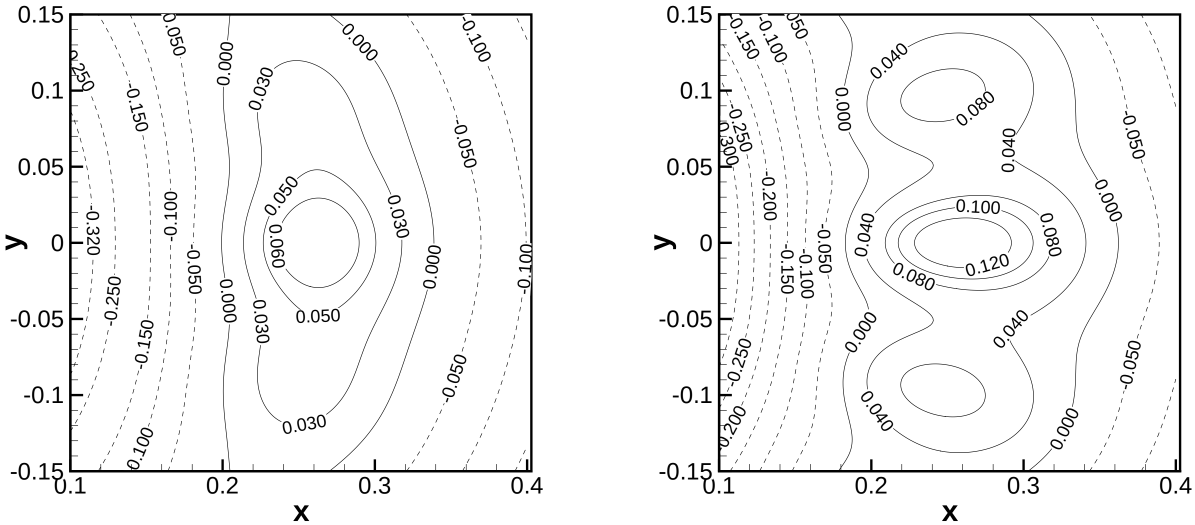

Figure 4.16: *Formulation A*. Contours of local Mach number, $M_l - 1.0$. Solid lines indicate regions of supersonic flow. (a)$\kappa = 3.00$, $c_\infty = 0.1690$. (b)$\kappa = 3.00$, $c_\infty = 0.1694$.

converged solution was obtained at $c_\infty = 0.1691$, $M_{max} = 1.071$, above which the exponential decay of a_{mn} and b_{mn} was lost, figures 4.14(a) and (b).

Figure 4.16 shows contours of $M_l - 1$ for both $c_\infty^{-1} = 0.1690$ and $c_\infty^{-1} = 0.1694$, windowed on a region near the vortex core boundary where the flow is locally supersonic. For $c_\infty^{-1} = 0.1690$ the extent of the supersonic region is rather small, considering the maximum value of $M_l - 1$. Similar plots of $\nabla \cdot u$ indicate smooth flow for this value of c_∞^{-1}. At $c_\infty^{-1} = 0.1694$ exponential convergence is lost, and the three local maxima in the Mach number form. The dilatational field begins to show irregularity, increasing sharply between the local maxima. As did MMP, we postulate that this may indicate the formation of incipient weak shocks, which causes convergence failure for the cosine series.

Formulation B locally supersonic flow: Under formulation B, much larger ranges of c_∞^{-1} and κ were found which yield solution showing smooth regions of supersonic flow, figure 4.11(b). For $\kappa = 5.0$ the numerical solutions show the onset

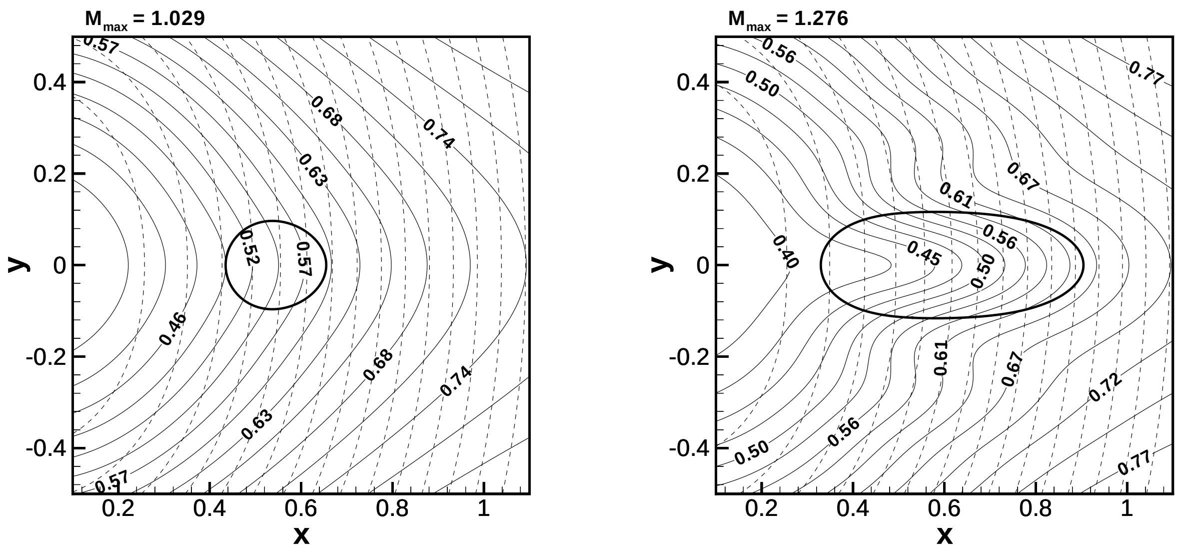

Figure 4.17: *Formulation B.* $\kappa = 5.00$; Heavy solid line $\rightarrow$ sonic line, $M_l = 1.0$. The flow contained in this region is supersonic. Dashed contours $\rightarrow$ stream-function. Solid, labeled contours $\rightarrow$ density. (a) $c_\infty^{-1} = 0.325$. (b) $c_\infty^{-1} = 0.342$.

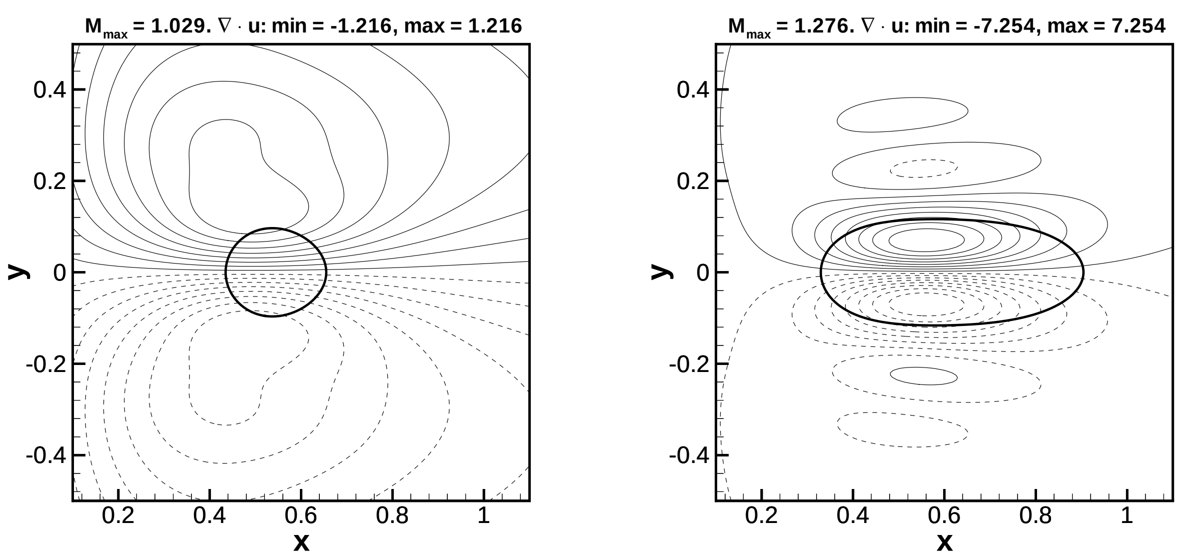

Figure 4.18: *Formulation B.* $\kappa = 5.00$; Heavy solid lines $\rightarrow$ sonic line, $M_l = 1.0$. Divergence of the velocity, $\nabla \cdot \mathbf{u}$, with dashed lines implying negative contours. (a) $c_\infty^{-1} = 0.325$. (b) $c_\infty^{-1} = 0.342$.

of transonic flow for c_∞^{-1} in the range 0.319 to 0.342. Three-point interpolation gives $M_{max} = 1.00$ at $c_\infty^{-1} = 0.3187$. At $c_\infty^{-1} = 0.342$, $M_{max} = 1.275$. Figures 4.14(c) and (d) show that convergence is not quite lost for $c_\infty^{-1} = 0.342$, however, the sharp upturn in the coefficients α_m and β_m indicate that if it were possible to find solutions at larger c_∞^{-1}, it is unlikely they would show exponential decay of the spectral coefficients.

Figures 4.17 and 4.18 show that the supersonic region is of sizable extent. The low vortex core density bulges into this region, so that following a streamline we see a substantial decrease in density, followed by a matching increase to preserve symmetry about the x-axis. This causes the magnitude of the divergence in velocity to increase, and show steep gradients inside the sonic bubble.

4.5 Remarks

Spectrally accurate numerical solutions to the steady compressible two dimensional Euler equations, representing two continuations to finite c_∞ of the Mallier & Maslowe [51] vortex, have been obtained. As in Meiron, Moore & Pullin [52] an eigenvalue was introduced into the vorticity-density-streamfunction relationship to continue the MM vortex to the compressible regime. Unexpectedly, it was also required that an extra parameter, Γ_c, be intercalated so that the circulation constraint could be enforced. Their values were determined as part of the overall solution, and were seen to vary with both mass flux between the vortex cores, and the sound speed at infinity. Increasing compressibility was seen to appreciably increase the aspect ratio of the vortices, while reducing the minimum value of density at the vortex core.

Numerical evidence for the existence of an substantial range of free stream sound speeds for which, at fixed ϵ, the solution corresponded to smooth transonic flow was presented. Under formulation B, at a value of ϵ corresponding to a value of the incompressible Maillier & Maslowe vortex parameter $\kappa = 5.00$, regions of smooth supersonic flow were found between $0.319 < c_\infty^{-1} < 0.342$. Branch termination is credited to to the large vertical dilatational gradients inside the locally supersonic region, which may indicate the formation of weak shocks there.

An interesting exercise would be to try use the Munk & Prim [64] transformation to try relate solutions from formulations A and B. Finally, it may be possible to formulate an number of interesting variation on the CMMV proposed here. One would be to look for a bifurcation to solutions which enable the stagnation points at the vortex cores to become hyperbolic. Another would be to allow a formulation for which symmetry about the x-axis is not enforced. A possible bifurcation to a non-symmetric state may allow for greater regions of locally supersonic flow before the solution branch terminates.

Chapter 5 Small perturbation theory of shock interactions

It is desirable to develop an approximate, semi-analytical method to compute the net effect of the passage of a planar shock through a steady compressible vortex. To facilitate this, we Fourier decompose the steady pre-shock vortex into a sum of frozen sinusoidal modes, treat the shock as an instantaneous event, and analytically compute the interaction of each frozen mode with the shock wave. The post-shock fields are then obtained by numerically resuming the shocked Fourier modes. Generally, the steady compressible, vortices considered are solutions of the steady, compressible, Euler equations. This implies that an individual pre-shock mode will not be bound by the linearized Euler equations, rather the sum of all the Fourier modes satisfies the non-linear, compressible, Euler equations exactly.

In this chapter we develop a theory for computing the interaction of a planar shock wave with a weak, inviscid, frozen sinusoidal disturbance in the upstream vorticity, dilatation, temperature and entropy. For an individual pre-shock mode, the flow is not bound by the compressible Euler equations. It is held steady until it has been processed by the shock-wave, after which time it's required that it evolve according to the compressible Euler equations, linearized about a uniform flow. This formulation is an extension of Ribner [74], who investigated the convection of a steady incompressible pattern of vorticity through a shock. The vorticity fields he considered are equivalent to the steady vorticity eigenmodes admitted by the linearized Euler equations. The Rankine-Hugoniot relations are used to derive the boundary conditions for the governing equations at the shock wave. The analysis gives the refraction and modification of the upstream disturbance into the three basis modes permitted by the linearized Euler equations (namely vortical, acoustic and entropy modes) in terms of transfer and phase functions, which depend on the shock Mach

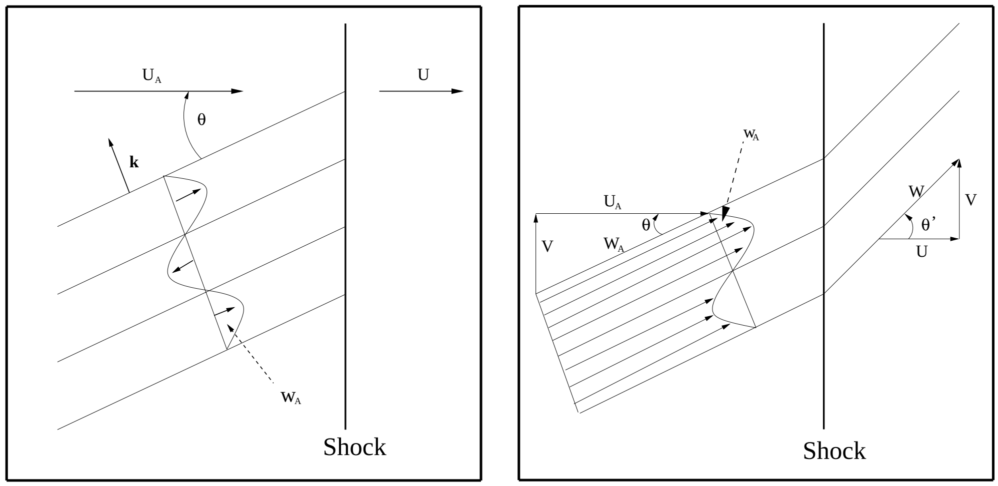

(a) (b)

Figure 5.1: (a) Convection of an inclined plane sinusoidal shear wave through a stationary shock, unsteady flow problem, Ribner [74]. (b) Equivalent steady flow problem.

number and inclination of the frozen perturbation to the shock. Also computed is the shock perturbation angle, which is shown to be phase shifted with respect to the initial upstream perturbation.

5.1 Ribner (1954): Incompressible shear wave

In what follows, pre-shock variables will be denoted with a subscript A, post-shock variables with no subscript and vectors with boldface symbols. Capital letters will indicate constant mean base flow quantities, while lower case letters imply perturbational variables. For convenience, table 5.1 gathers some of the important definitions of the basic variables used in this chapter.

Ribner [74], henceforth referred to as R54, analyzed the flow behind a plane normal stationary shock wave due to the convection through the shock of a steady inclined plane sinusoidal shear wave with speed U_A. The downstream normal velocity is $\mathbf{U}$, with M_U as the corresponding Mach number, $M_U < 1$. Presently, the wave vector of the incident shear wave will be denoted $\mathbf{k}$ and its velocity vector $\mathbf{w}_A$. The angle between the vector $\mathbf{k}$ and the unperturbed shock is θ, where, due to the incompress-

U_A	Pre-shock mean velocity in the x-direction.
$W_A = U_A/\cos(\theta)$	Pre-shock mean main-stream velocity in the moving frame of reference.
C_A	Pre-shock mean sound speed.
U	Post-shock mean velocity in the x-direction.
$W = U/\cos(\theta')$	Post-shock mean main-stream velocity in the moving frame of reference.
C	Post-shock mean sound speed.
$M_S = U_A/C_A$	Shock Mach number.
$M_U = U/C$	Post-shock normal mean Mach number in a frame of reference where the shock is stationary.
$\nu = U_A/U$	Velocity ratio.
ξ_1	Post-shock main-stream direction in moving frame of reference.
ξ_2	Post-shock cross-stream direction in moving frame of reference.
$\mathbf{w}_A$	Pre-shock perturbational velocity vector.
$\mathbf{w} = (w^{(1)}, w^{(2)})$	Post-shock perturbational velocity vector.
$w^{(1)}$	Post-shock perturbation velocity in the main-stream direction ξ_1.
$w^{(2)}$	Post-shock perturbation velocity in the cross-stream direction ξ_2.
$\mathbf{k}$	Pre-shock wave vector.
$\mathbf{k}'$	Post-shock shear-entropy wave vector.
$\mathbf{k}''$	Post-shock pressure wave vector.
θ	Angle between $\mathbf{k}$ and the unperturbed shock.
θ'	Angle between $\mathbf{k}'$ and the unperturbed shock.
θ''	Angle between $\mathbf{k}''$ and the unperturbed shock.
$\sigma(y)$	Perturbation to shock inclination angle.

Table 5.1: Reference table containing important basic variables used extensively in this chapter.

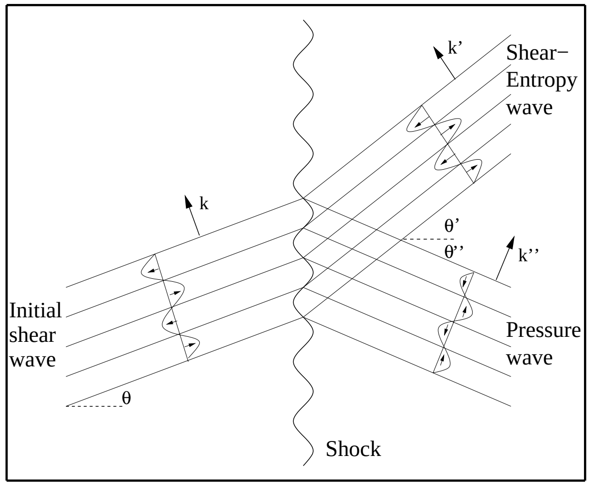

Figure 5.2: Interaction of an incompressible shear wave with a shock, Ribner [74].

ibility of the shear wave, $\mathbf{w_A} \cdot \mathbf{k} = 0$, figure 5.1(a). To ensure small perturbations to the mean flow, Ribner assumed that $w_A/U_A \ll 1$. The interaction shown in figure 5.1(a) is an unsteady process, the nodal lines of the perturbations move down along the shock with speed $V = U_A \tan(\theta)$. To convert to an equivalent steady flow problem, Ribner made a transformation to a frame of reference where the observer moves down along the shock with speed V, seeing what appears to be a steady sinusoidal shear flow passing through an oblique stationary shock wave. In this frame of reference the upstream main-stream velocity is denoted $\mathbf{W_A}$ ($\mathbf{w_A} \parallel \mathbf{W_A}$), figure 5.1(b). Downstream of the oblique shock, the main-stream velocity $\mathbf{W}$, which makes an angle θ' with the normal shock velocity $\mathbf{U}$, may be either subsonic or supersonic depending on the incident angle θ, that is $M_U/\cos(\theta') \gtrless 1$.

Ribner formulated the analysis as a boundary value problem for the velocity field in the region downstream of the shock, where the governing equations are the Euler equations linearized about a uniform stream flow, with boundary conditions at the shock derived from the oblique shock relations. Small shock curvature was accounted for, and the Rankine-Hugoniot relationship for the entropy jump across a shock was used to compute certain elements of the governing equation. The associated pressure perturbation was recovered from a linearized version of the Bernoulli equation. A linearized equation of state was then used to recover the density field from the pressure and entropy perturbations.

The incompressible vorticity wave excites all three modes permitted by the linearized Euler equations in the downstream flow: vorticity, entropy and acoustic, figure 5.2. The shear-entropy wave produced has wave vector $\mathbf{k}'$, while the pressure wave has wave vector $\mathbf{k}''$. These vectors make angles θ' and θ'' with the unperturbed shock respectively. In Ribner's special steady frame of reference, for values of θ less than some critical angle, θ_{crit}, the downstream flow is subsonic, $M_U/\cos(\theta') < 1$. In this regime, the pressure wave exponentially attenuates with downstream distance from the shock, implying that far downstream of the shock the flow is incompressible, with a fluctuating vorticity and entropy field. For θ greater than θ_{crit} the pressure wave is unattenuated, and can be recognized as an acoustic wave. For super critical incident angles, the angle between the shear-entropy wave and the acoustic wave is the Mach angle, $\theta' - \theta'' = \mu_M$, where $\mu_M = \operatorname{arccot}\left(\sqrt{(M_U/\cos(\theta'))^2 - 1}\right)$. The amplitude and phase of the ripples, developed in the shock by the passage of the shear wave were also computed. The shock corrugation progressively lags the initial shear wave as θ is increased, until the sonic condition, $M_U/\cos(\theta') = 1$, is reached. At this point the lag is $\pi/2$, and is maintained at this value throughout the range $M_U/\cos(\theta') > 1$.

5.2 Compressible disturbance

Reference base flow thermodynamic variables are designated (R, P, S, T), the density, pressure, entropy and temperature respectively. We consider the problem of a plane sinusoidal wave, with perturbations in velocity, temperature and entropy, $(\mathbf{w}_A, \tau_A, s_A)$, convected through a stationary normal shock (where the shock is aligned with the y-axis) with velocity $\mathbf{U}_A$ in the positive x-direction, figure 5.3(a). The corresponding perturbations in pressure and density are denoted p_A and ρ_A respectively. The perturbations are assumed small, $(|\mathbf{w}_A|/U_A, \tau_A/T_A, s_A/c_v) \ll 1$, and are inclined at an angle θ to the stream velocity U_A, $-\pi/2 \leq \theta \leq \pi/2$. The initial wave is frozen, meaning that the perturbations in velocity, temperature and entropy do not obey

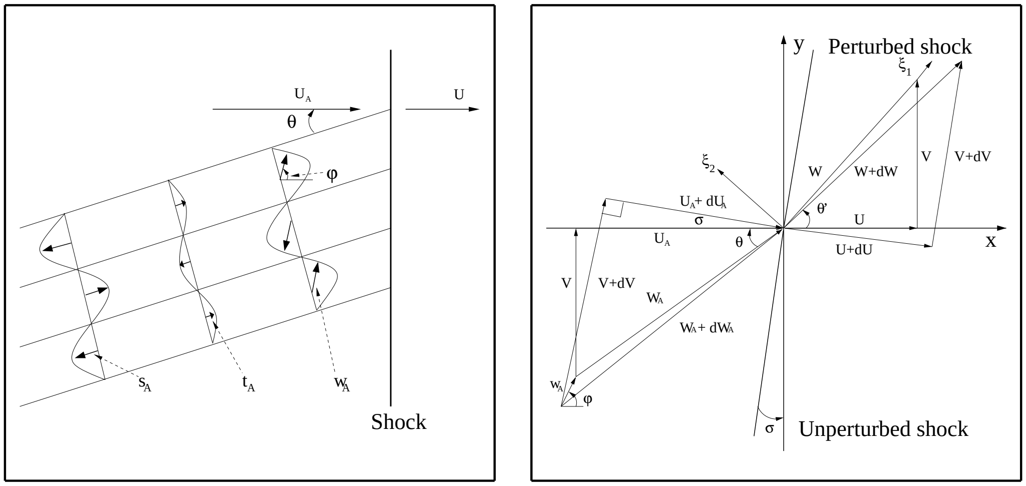

(a) (b)

Figure 5.3: (a) Convection of a frozen inclined plane sinusoidal disturbance in vorticity, dilatation, entropy and temperature through a stationary normal shock, unsteady problem. (b) The local perturbed axis of the equivalent steady flow problem.

any particular relationship in the upstream flow. They are held steady till they have been processed by the shock, after which, in the downstream medium, they will be required to satisfy the Euler equations linearized about a uniform flow. The only caveat here is that a linear equation of state is satisfied by the pre-shock perturbed thermodynamic variables, so that a perturbation in sound speed, and subsequently in normal Mach number, may be defined.

As in R54, it proves convenient to transform to a reference frame in which the interaction is steady. An observer moving down along the shock with speed $V = U_A \tan(\theta)$, sees a steady perturbation passing through a stationary oblique shock. The angle between the resultant pre-shock main-stream velocity, $\mathbf{W}_A$, and the perturbation velocity, $\mathbf{w}_A$, is $(\varphi - \theta)$, figure 5.3(b). The pre-shock perturbation velocity will be decomposed into a main-stream component, representing disturbances in the upstream vorticity field, and cross-stream component, representing disturbances in the upstream dilatational field; $\mathbf{w}_A = (w_A^{(1)}, w_A^{(2)})$ where $(w_A^{(1)} \parallel \mathbf{W}_A,\, w_A^{(2)} \perp \mathbf{W}_A)$. In the moving reference frame the main-stream and cross-stream directions are denoted ξ_1

and ξ_2 and respectively.

$$\xi_1 = x\cos(\theta') + y\sin(\theta'), \quad \xi_2 = -x\sin(\theta') + y\cos(\theta'). \tag{5.1}$$

In the moving frame of reference the post-shock main-stream velocity is $\mathbf{W}$, in the direction ξ_1. The upstream perturbations are chosen to be functions of the cross-stream ordinate, ξ_{2A}, alone.

5.2.1 Perturbed variables

By geometry, figure 5.3(b), the stream velocity components normal and tangential to the undisturbed shock are

$$U_A = W_A\cos(\theta), \quad V = W_A\sin(\theta). \tag{5.2}$$

The pre-shock disturbances provide a perturbation to the shock wave angle, $\sigma(y)$ in figure 5.3(b), the magnitude of which is initially undetermined. The perturbations to U_A and V may be written in terms of this perturbed quantity and the perturbation in velocity:

$$\begin{aligned} U_A + dU_A &= |\mathbf{W}_A + \mathbf{w}_A|\cos(\varphi + \sigma), \\ V + dV &= |\mathbf{W}_A + \mathbf{w}_A|\sin(\varphi + \sigma). \end{aligned} \tag{5.3}$$

Linearizing the respective expressions for the differentials in equation (5.3), about expression (5.2) yields

$$\begin{aligned} dU_A &= w_A^{(1)}\cos(\theta) - w_A^{(2)}\sin(\theta) - \sigma W_A\sin(\theta), \\ dV &= w_A^{(1)}\sin(\theta) + w_A^{(2)}\cos(\theta) + \sigma W_A\cos(\theta). \end{aligned} \tag{5.4}$$

The perturbation in sound speed, C_A, is given by

$$dC_A = C_A\frac{\tau_A}{2T_A}, \tag{5.5}$$

from which, with equation (5.4), the perturbation to the normal Mach number may be obtained,

$$dM_S = \frac{w_A^{(1)}}{C_A}\cos(\theta) - \frac{w_A^{(2)}}{C_A}\sin(\theta) - \sigma\frac{W_A}{C_A}\sin(\theta) - M_S\frac{\tau_A}{2T_A}. \tag{5.6}$$

The first term is due to the perturbation in upstream vorticity, the second arises through variable compressibility in the upstream disturbance, the third comes from the perturbation to the shock, and the fourth is due to the temperature perturbation.

5.2.2 Governing equation

In the post-shock region the fluid is assumed steady, two-dimensional, adiabatic and inviscid. The governing equations are then the Euler equations linearized about a uniform stream flow. The linearized continuity, momentum, energy and state equations allow for a stream-function formulation,

$$w^{(1)} = \psi_{\xi_2}, \quad w^{(2)} = -\left(1 - \frac{M_U^2}{\cos^2(\theta')}\right)\psi_{\xi_1}. \tag{5.7}$$

Expressing the vorticity in terms of gradients of entropy and total enthalpy yields a single equation for ψ, the derivation of which can be found in R54,

$$\left(1 - \frac{M_U^2}{\cos^2(\theta')}\right)\psi_{\xi_1\xi_1} + \psi_{\xi_2\xi_2} = \frac{h_{\xi_2}}{W} - \frac{Ts_{\xi_2}}{W}, \tag{5.8}$$

where H is the stagnation enthalpy. The form of equation (5.8) resembles a forced Prandtl-Glauert equation. The flow assumptions downstream of the shock imply that the enthalpy and entropy are constant along streamlines, which in the linear theory are approximated by lines of constant ξ_2. Consequently, if expressions for h_{ξ_2} and Ts_{ξ_2} can be derived at the shock and are found to be independent of ξ_1, the linear theory implies that these expressions will be valid everywhere in the downstream flow, thus enabling a governing equation valid everywhere downstream of the shock to be derived. To do this the Rankine-Hugoniot conditions for temperature, entropy and normal velocity are employed.

The first use of the normal shock jump relations comes in defining the velocity ratio, ν, which is defined as the ratio of upstream normal mean velocity to downstream normal mean velocity in a frame of reference in which the shock is stationary,

$$\nu = \frac{U_A}{U} = \frac{\frac{1}{2}(\gamma+1)M_S^2}{1+\frac{1}{2}(\gamma-1)M_S^2}. \tag{5.9}$$

The angle θ' (see figure 5.3) is defined in terms of this compression factor by means of the oblique-shock relation

$$\theta' = \arctan\left(\nu\tan(\theta)\right). \tag{5.10}$$

Upstream of the shock the total enthalpy can be written as

$$\begin{aligned} h &= c_p\left(T_A+\tau_A\right)+\frac{1}{2}\left(\mathbf{W}_A+\mathbf{w}_A\right)^2, \\ &\sim \frac{C_A^2}{\gamma-1}\left(1+\frac{\tau_A}{T_A}\right)+\frac{1}{2}W_A^2\left(1+2\frac{w_A^{(1)}}{W_A}\right). \end{aligned} \tag{5.11}$$

The total enthalpy is constant across the shock, therefore along the shock

$$\frac{\partial h}{\partial \xi_2} = \frac{C_A^2}{\gamma-1}\frac{\partial}{\partial \xi_2}\left(\frac{\tau_A}{T_A}\right)+W_A^2\frac{\partial}{\partial \xi_2}\left(\frac{w_A^{(1)}}{W_A}\right). \tag{5.12}$$

To derive the temperature and entropy jumps across a normal shock requires a second use of the Rankine-Hugoniot jump conditions. These are given in terms of the upstream normal Mach number, reference [65] (equations (115) and (120)),

$$\frac{T+\tau}{T_A+\tau_A} = \frac{\left(2\gamma\left(M_S+dM_S\right)^2-(\gamma-1)\right)\left((\gamma-1)\left(M_S+dM_S\right)^2+2\right)}{(\gamma+1)^2\left(M_S+dM_S\right)^2}, \tag{5.13}$$

$$\frac{1}{c_v}\left(S - S_A + s - s_A\right) = \log\left(\frac{2\gamma\left(M_S + dM_S\right)^2 - (\gamma - 1)}{\gamma + 1}\right)$$
$$-\gamma\log\left(\frac{(\gamma+1)\left(M_S + dM_S\right)^2}{(\gamma+1)\left(M_S + dM_S\right)^2 + 2}\right). \quad (5.14)$$

Equations (5.9), (5.13) and (5.14), together with linearization and differentiation with respect to ξ_2, imply that at the downstream side of the shock

$$\frac{\partial s}{\partial \xi_2} = \frac{\partial s_A}{\partial \xi_2} + 2(\nu - 1)\frac{U^2}{T}\frac{\partial}{\partial \xi_2}\left(\frac{w_A^{(1)}}{W_A} - \tan(\theta)\frac{w_A^{(2)}}{W_A} - \tan(\theta)\sigma - \frac{\tau_A}{2T_A}\right). \quad (5.15)$$

Equations (5.12) and (5.15) cast the right hand side of equation (5.8), evaluated at the downstream side of the shock, entirely in terms of the input perturbations, and the perturbation to the shock inclination angle. To establish that the gradients in enthalpy and entropy, evaluated at the shock, are independent of the main-stream ordinate, ξ_1, a form for the pre-shock perturbations must be chosen.

$$\begin{aligned} \frac{w_A^{(1)}}{W_A} &= \epsilon_1 \cos(\mathbf{k}\cdot\mathbf{x}), \qquad & \frac{w_A^{(2)}}{W_A} &= \epsilon_2 \cos(\mathbf{k}\cdot\mathbf{x}), \\ \frac{\tau_A}{T_A} &= \epsilon_3 \cos(\mathbf{k}\cdot\mathbf{x}), \qquad & \frac{s_A}{c_v} &= \epsilon_4 \cos(\mathbf{k}\cdot\mathbf{x}), \end{aligned} \quad (5.16)$$

where $\mathbf{k}$ is a wave vector making an angle θ with the positive y axis (so that it points in the ξ_{2A} direction) and $(\epsilon_1, \epsilon_2, \epsilon_3, \epsilon_4) \ll 1$. A formulation in which the temperature and entropy perturbations were chosen to be out of phase with the velocity perturbations was also considered, although that analysis is not currently presented. At the shock the arguments of the pre-shock and post-shock waves must match, so that

$$k\xi_{2A} = k'\xi_2, \quad \frac{k}{k'} = \frac{\cos(\theta')}{\cos(\theta)}, \quad \text{along the shock}, \quad (5.17)$$

where k' is the wave number of the refracted wave. Equations (5.16) and (5.17) imply that the perturbation to the shock inclination angle also has a sinusoidal form, although a phase shift is allowed for,

$$\sigma(y) = a\cos(k'\xi_2) + b\sin(k'\xi_2). \tag{5.18}$$

The parameters a and b are linear functionals of $(\epsilon_1, \epsilon_2, \epsilon_3, \epsilon_4)$, and are determined, through a matching process at the shock, as part of the solution. For this choice of upstream perturbations expressions (5.12) and (5.15) are indeed independent of ξ_1, and may be substituted into equation (5.8) to obtain an intermediate form of the governing equation, valid everywhere downstream of the shock.

$$\begin{aligned}\left(1 - \frac{M_U^2}{\cos^2(\theta')}\right)\psi_{\xi_1\xi_1} + \psi_{\xi_2\xi_2} = {} & U\left(\frac{\nu^2\cos(\theta)}{(\gamma-1)M_S^2}\frac{\partial}{\partial\xi_2}\left(\frac{\tau_A}{T_A}\right) + \nu^2\frac{\cos(\theta')}{\cos(\theta)^2}\frac{\partial}{\partial\xi_2}\left(\frac{w_A^{(1)}}{W_A}\right)\right) \\ & - U\left(\frac{\cos(\theta')}{\gamma(c_p - c_v)M_U^2}\frac{\partial s_A}{\partial\xi_2} + (\nu-1)^2\cos(\theta)\right. \\ & \left.\times\frac{\partial}{\partial\xi_2}\left(\frac{w_A^{(1)}}{W_A} - \tan(\theta)\frac{w_A^{(2)}}{W_A} - \tan(\theta)\sigma - \frac{\tau_A}{2T_A}\right)\right)\end{aligned} \tag{5.19}$$

Using equations (5.16), with $k\xi_{2A} = k'\xi_2$, allows the final form of the governing equation to be derived.

$$\begin{aligned}\left(1 - \frac{M_U^2}{\cos^2(\theta')}\right)\psi_{\xi_1\xi_1} + \psi_{\xi_2\xi_2} = {} & -k'U\left(\epsilon_1(\Omega)_1^{GE} + \epsilon_2(\Delta)_1^{GE} + \epsilon_3(\Theta)_1^{GE} + \epsilon_4(\Lambda)_1^{GE}\right. \\ & \left. + \, a(\Sigma)_1^{GE}\right)\sin(k'\xi_2) + k'U\left(b(\Sigma)_1^{GE}\right)\cos(k'\xi_2),\end{aligned} \tag{5.20}$$

where

$$0 < \xi_1 < \infty, \quad -\infty < \xi_2 < \infty. \tag{5.21}$$

The terms due to vorticity (Ω), compressibility (Δ), temperature (Θ), entropy (Λ) and shock curvature (Σ) are defined in Appendix C. Equation (5.20) changes in nature, from elliptic to hyperbolic, as the sonic threshold in the downstream flow is crossed. Thus, the final flow pattern depends crucially on whether $M_U/\cos(\theta') \gtrless 1$.

5.2.3 Pressure and density

Equation (5.20) governs the velocity perturbations downstream of the shock, however, it does not contain information about the about the pressure and density perturbations there. This information is recovered by considering a special type of velocity field which can be decomposed into the sum of a potential flow and a rotational flow in the following manner,

$$w^{(1)}(\xi_1, \xi_2) = w_p^{(1)}(\xi_1, \xi_2) + w_s^{(1)}(\xi_2), \quad w^{(2)}(\xi_1, \xi_2) = w_p^{(2)}(\xi_1, \xi_2), \tag{5.22}$$

where the subscript p denotes potential, and s rotational. It will be seen that this decomposition naturally arises for solutions to equation (5.20). Equation (5.22) allows the linearized momentum equations to be reduced to a linearized Bernoulli equation, which relates the pressure to the main-stream potential velocity component,

$$\frac{p}{R} + W w_p^{(1)} = 0. \tag{5.23}$$

The entropy perturbation is given by equation (5.15) and is related to the vorticity through equation (5.8). Thus, it is associated with the main-stream rotational component of the velocity field, $w_s^{(1)}$. The linearized equation of state then relates the density perturbation to the pressure and entropy perturbations, see R54,

$$\frac{\rho}{R} = -\frac{M_U^2}{\cos^2(\theta')} \frac{w_p^{(1)}}{W} - \frac{s}{c_p}. \tag{5.24}$$

Physically this implies that for flows which can be decomposed into the form given by equation (5.22), the pressure perturbation arises from the main-stream potential component of the velocity, $w_p^{(1)}$, through equation (5.23), while the density perturbation depends on both the main-stream potential and rotational components of the velocity perturbation through equation (5.24).

5.2.4 Boundary conditions

By logarithmic differentiation of equation (5.9), which gives the Rankine-Hugoniot condition for jump in normal velocity across a stationary shock, it can be shown that

$$\frac{dU}{U} = \frac{dU_A}{U_A} - 2\frac{dM_S}{M_S}\left(1 - \frac{\gamma - 1}{\gamma + 1}\nu\right). \tag{5.25}$$

At the shock, on the downstream side, denoted by the subscript o, the velocity perturbation in the main-stream and cross-stream directions may be written as

$$\begin{aligned} w_0^{(1)} &= (U + dU)\cos(\theta' + \sigma) + (V + dV)\sin(\theta' + \sigma) - W \\ w_0^{(2)} &= -(U + dU)\sin(\theta' + \sigma) + (V + dV)\cos(\theta' + \sigma). \end{aligned} \tag{5.26}$$

Using equation (5.6) in (5.25), and subsequently equation (5.25) in (5.26), a corresponding set of boundary conditions to those in R54 may be derived,

$$\begin{aligned} \frac{w_0^{(1)}}{U} &= -\left(R_1 + C_1 + T_1\right)\cos(\theta') + (R_2 + C_2)\sin(\theta'), \\ \frac{w_0^{(2)}}{U} &= (R_1 + C_1 + T_1)\sin(\theta') + (R_2 + C_2)\cos(\theta') - \sigma\sec(\theta'), \end{aligned} \tag{5.27}$$

with the pre-factors of $\sin(\theta')$ and $\cos(\theta')$ defined in Appendix D. Again, using equations (5.16) in equations (5.27), the final form of the boundary conditions may be derived.

$$\begin{aligned} \frac{w_0^{(1)}}{U} &= \left(\epsilon_1(\Omega)_1^{BC} + \epsilon_2(\Delta)_1^{BC} + \epsilon_3(\Theta)_1^{BC} + a(\Sigma)_1^{BC}\right)\cos(k'\xi_2) + \left(b(\Sigma)_1^{BC}\right)\sin(k'\xi_2), \\ \frac{w_0^{(2)}}{U} &= \left(\epsilon_1(\Omega)_2^{BC} + \epsilon_2(\Delta)_2^{BC} + \epsilon_3(\Theta)_2^{BC} + a(\Sigma)_2^{BC}\right)\cos(k'\xi_2) + \left(b(\Sigma)_2^{BC}\right)\sin(k'\xi_2), \end{aligned} \tag{5.28}$$

where the terms due to vorticity, compressibility, temperature and shock curvature are defined in Appendix D. Equations (5.28) give the boundary conditions, dictated by the shock, on the perturbation to the stream velocity in the ξ_1 and ξ_2 directions immediately behind the shock. Equation (5.20) is the linear partial differential equa-

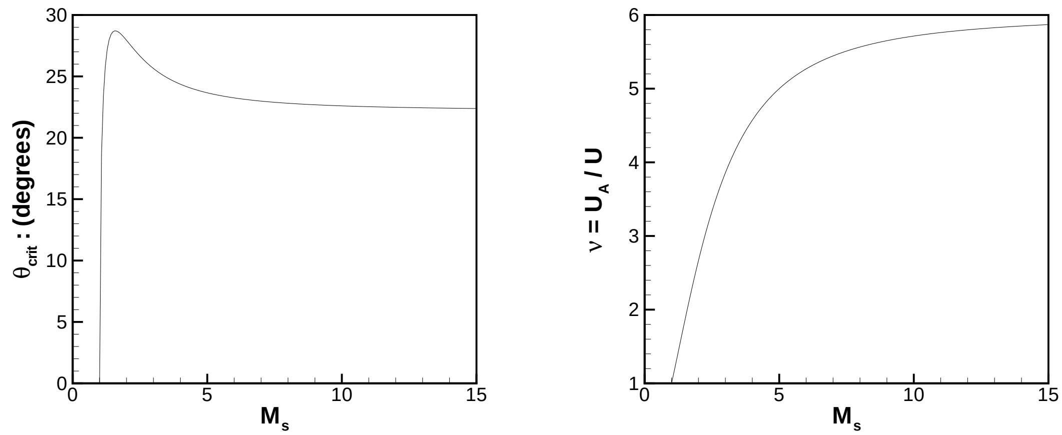

(a) (b)

Figure 5.4: (a) θ_{crit} versus the shock Mach number, M_s. (b) ν versus M_s.

tions to be satisfied by the flow downstream of the shock, subject to these boundary conditions.

To better illustrate the solution technique, and the means by which the constants a and b are decided, the solution for a horizontal wave, $\theta = 0$, for which the governing equation and boundary conditions are greatly reduced, is presented in Appendix E. For the general case, $\theta \neq 0$, the stream velocity W may be subsonic or supersonic depending on the initial Mach number, M_S, and the incident angle, θ. The dividing line, $M_U/\cos(\theta') = 1$, is conveniently expressed in terms of a critical angle as

$$\theta_{crit} = \pm \arctan \sqrt{\frac{(\gamma+1)(\nu-1)}{2\nu^2}}. \tag{5.29}$$

Figure 5.4 shows the critical angle and the velocity ratio, ν, over a range of shock Mach numbers. For $\theta < \theta_{crit}$ the mean downstream velocity is subsonic, for $\theta > \theta_{crit}$ it's supersonic. Separate solutions, described below, are required for each case.

5.2.5 Subsonic solution: $M_U/\cos(\theta') < 1$

The current analysis follows R54 closely, and uses results from R54 as a consistency check to the limiting case of $\epsilon_2 = \epsilon_3 = \epsilon_4 = 0$. Constraining the mean velocity W to be subsonic behind the oblique shock, ensures that the governing equation are elliptic.

Defining $\beta_w^2 = 1 - (M_U/\cos(\theta'))^2$, equation (5.20) becomes

$$\begin{aligned}\beta_w^2 \psi_{\xi_1\xi_1} + \psi_{\xi_2\xi_2} &= -k'U\left(A\sin(k'\xi_2) + B\cos(k'\xi_2)\right),\\ A &= \epsilon_1(\Omega)_1^{GE} + \epsilon_2(\Delta)_1^{GE} + \epsilon_3(\Theta)_1^{GE} + \epsilon_4(\Lambda)_1^{GE} + a(\Sigma)_1^{GE},\\ B &= b(\Sigma)_1^{GE}.\end{aligned} \tag{5.30}$$

The constants A and B are determined, through a and b, by matching the solution of the governing equation to the boundary conditions at the shock. The solution is written as the sum of a particular integral and a complementary function, where the particular integral is given by

$$\psi_p(\xi_2) = U\left(\frac{A}{k'}\sin(k'\xi_2) - \frac{B}{k'}\cos(k'\xi_2)\right). \tag{5.31}$$

For $M_U/\cos(\theta') < 1$ the complementary function is expected to attenuate exponentially with downstream distance from the shock. At the shock, the boundary conditions stipulate that it possess a purely sinusoidal behavior with a predefined argument. Writing $\beta_u^2 = 1 - M_U^2$, $x = \xi_1\cos(\theta') - \xi_2\sin(\theta')$ and using R54 as a guide, the complementary function is shown to be

$$\begin{aligned}\psi_c(\xi_1,\xi_2) = U\exp&\left(-\frac{k'\beta_w}{\beta_u^2}\cos(\theta')\left[\xi_1\cos(\theta') - \xi_2\sin(\theta')\right]\right)\\ &\times\left[\frac{c}{k'\beta_w\cos(\theta')}\cos\left(\frac{k'\cos(\theta)}{\beta_u^2}(\xi_1\sin(\theta') + \beta_w^{(2)}\xi_2\cos(\theta'))\right)\right.\\ &+\left.\frac{d}{k'\beta_w\cos(\theta')}\sin\left(\frac{k'\cos(\theta)}{\beta_u^2}(\xi_1\sin(\theta') + \beta_w^{(2)}\xi_2\cos(\theta'))\right)\right],\end{aligned} \tag{5.32}$$

where c and d are integration constants. As for the horizontal wave solution, Appendix E, expressions (5.31) and (5.32) are used in equation (5.7) to derive the velocity perturbations valid everywhere downstream of the shock. These are then matched to the boundary conditions at the shock, yielding a system of linear algebraic equations for the constants (a, b, c, d).

$$\begin{aligned} H_1 a + H_2 c + H_3 d &= \epsilon_1(\Omega)_1 + \epsilon_2(\Delta)_1 + \epsilon_3(\Theta)_1 + \epsilon_4(\Lambda)_1, \\ H_1 b - H_3 c + H_2 d &= 0, \\ H_4 a + \beta_w H_3 c - \beta_w H_2 d &= \epsilon_1(\Omega)_2 + \epsilon_2(\Delta)_2 + \epsilon_3(\Theta)_2, \\ H_4 b + \beta_w H_2 c + \beta_w H_3 d &= 0. \end{aligned} \tag{5.33}$$

The derivations and definitions of equations (5.33), with their solution, are given in Appendix F.

5.2.6 Supersonic solution: $M_U/\cos(\theta') > 1$

Supersonic downstream mean velocity implies that the solution must exhibit Mach waves. In the unsteady frame of reference convected downstream with velocity U, these waves must be plane sound waves moving normal to the wave fronts with sonic velocity.

In this regime equation (5.20) is hyperbolic. The particular integral remains unchanged, and is given by equation (5.31). It is found that for in phase perturbations, the final solution gives $b = 0$, so that $B = 0$. This term is then excluded from the outset and the particular integral reduces to

$$\psi_p(\xi_2) = \frac{U}{k'} A \sin(k'\xi_2), \tag{5.34}$$

where A is given by equation (5.30). The complementary function represents the irrotational component of the downstream flow, from which the pressure perturbations will be seen to originate, Section 5.3. If the solution exhibits Mach waves, ψ_c cannot be exponentially attenuated with downstream distance from the shock.

$$\psi_c(\xi_1, \xi_2) = \frac{Uc}{k'\beta_w \cos(\theta)} \sin\left(\frac{k'\left(\xi_1 + \beta_w \xi_2\right)}{\beta_w + \tan(\theta')}\right), \tag{5.35}$$

where $\beta_w = \sqrt{(M_U/\cos(\theta'))^2 - 1}$ and c is the constant of integration. The function ψ_c is constant along lines inclined from the ξ_1-axis by the Mach angle, $\mu_M = \text{arccot}(\beta_w)$. Equation (5.32) is only valid for $0 \leq \theta \leq \pi/2$. It can be shown that, for a finite shock strength $\mu_M > \pi/2 - |\theta'|$, which implies that if θ is in the range $-\pi/2 \leq \theta \leq 0$, equation (5.35) corresponds to disturbances overtaking the shock from behind. These waves should not arise, as the disturbance originates at the shock. The transformation $\beta_w \to -\beta_w$, applied to the constants a and c and equation (5.35), generates physically sensible solutions for negative incident angles.

The velocity perturbations are derived by substitution of expressions (5.34) and (5.35) into equation (5.7), which are matched to boundary conditions (5.28) to obtain two linear algebraic equations determining the constants a and c.

$$\begin{aligned} G_1 a + G_2 c &= \epsilon_1(\Omega)_1 + \epsilon_2(\Delta)_1 + \epsilon_3(\Theta)_1 + \epsilon_4(\Lambda)_1, \\ G_3 a + \beta_w G_2 c &= \epsilon_1(\Omega)_2 + \epsilon_2(\Delta)_2 + \epsilon_3(\Theta)_2. \end{aligned} \tag{5.36}$$

The derivations and definitions of equations (5.36), with their solution, are given in Appendix G.

5.3 Results

The analysis has been carried out in Ribner's special frame of reference, where the flow is steady. Formula are given relative to this frame of reference, although if results in a frame of reference convected by the mean flow are required, the following transformation can be used,

$$\begin{aligned} \xi_1 \to \xi_1 + Wt, &\qquad \xi_2 \to \xi_2 \\ x \to x + Ut, &\qquad y \to y + Vt. \end{aligned} \tag{5.37}$$

The results presented below are given for $0 \leq \theta \leq \pi/2$, if results for negative incident angles are required, they can be obtained by use of symmetry of the flow with respect to θ and in turn θ'.

Subsonic main-stream velocity: For subsonic resultant downstream velocity, the velocity perturbations are written in the form

$$\begin{aligned}\frac{w^{(1)}}{W_A} &= \sum_{j=1}^{4} \epsilon_j S_j \cos\left(\mathbf{k}' \cdot \mathbf{x} + \delta_{s_j}\right) + \epsilon_j e^{-\frac{\beta_w}{\beta_u^2} x k' \cos(\theta')} \Pi_j \cos\left(\mathbf{k}'' \cdot \mathbf{x} + \delta_{p_j}\right), \\ \frac{w^{(2)}}{W_A} &= \sum_{j=1}^{4} \epsilon_j \beta_w e^{-\frac{\beta_w}{\beta_u^2} x k' \cos(\theta')} \Pi_j \sin\left(\mathbf{k}'' \cdot \mathbf{x} + \delta_{p_j}\right).\end{aligned} \tag{5.38}$$

The wave vector $\mathbf{k}'$ makes an angle θ' with the positive y-axis and points in the ξ_2 direction. The angle θ' is defined by means of an oblique shock relation, equation (5.10). The vector $\mathbf{k}''$ makes an angle θ'' with the positive y-axis.

$$\theta'' = -\arctan\left(\frac{M_U^2 \tan(\theta')}{\beta_u^2}\right). \tag{5.39}$$

The angle θ'' is obtained from expression (5.32) for ψ_c (the subsonic solution to the homogeneous governing equation). The transfer functions $S_j(M_S, \theta)$ and $\Pi_j(M_S, \theta)$, and phase leads/lags $\delta_{s_j}(M_S, \theta)$ and $\delta_{p_j}(M_S, \theta)$ are:

$$\begin{aligned}S_j &= \frac{\cos(\theta)}{\nu}\sqrt{A_j^2 + B_j^2}, \qquad \delta_{s_j} = \arctan\left(\frac{-B_j}{A_j}\right), \\ \Pi_j &= \frac{\cos(\theta)}{\nu\beta_u}\sqrt{c_j^2 + d_j^2}, \qquad \delta_{p_j} = \arctan\left(\frac{c_j\beta_w - d_j \tan(\theta')}{d_j\beta_w + c_j \tan(\theta')}\right),\end{aligned} \tag{5.40}$$

where subsonic expressions for A_j, B_j, c_j and d_j are given in Appendix F.

Supersonic main-stream velocity: For supersonic mean downstream velocity, the velocity perturbations are written as:

$$\begin{aligned}\frac{w^{(1)}}{W_A} &= \sum_{j=1}^{4} \epsilon_j S_j \cos\left(\mathbf{k}' \cdot \mathbf{x}\right) + \epsilon_j \Pi_j \cos\left(\mathbf{k}'' \cdot \mathbf{x}\right), \\ \frac{w^{(2)}}{W_A} &= \sum_{j=1}^{4} \epsilon_j \beta_w \Pi_j \sin\left(\mathbf{k}'' \cdot \mathbf{x}\right).\end{aligned} \tag{5.41}$$

Again, the wave vector $\mathbf{k}'$ makes an angle θ' with the positive y axis, while the vector $\mathbf{k}''$ makes an angle θ'' with the positive y-axis,

$$\theta'' = \theta' - \mu_M. \tag{5.42}$$

The transfer functions $S_j(M_S, \theta)$ and $\Pi_j(M_S, \theta)$ are:

$$S_j = \frac{\cos(\theta)}{\nu} A_j, \quad \Pi_j = \frac{\sin(\mu_M)}{\nu \beta_u} \frac{\cos(\theta)}{\cos(\theta'')} c_j, \tag{5.43}$$

where the supersonic expression for A_j and c_j are given in Appendix G.

Shear-entropy wave: The argument of the cosine in the S_j terms is constant along lines parallel to the velocity w, which points along the ξ_1-axis. Thus, the flow due to the S_j terms is an incompressible, plane, transverse, sinusoidal rotational wave. Ribner denoted this wave the post-shock shear wave, where the vorticity due to the wave has been computed earlier in terms of the gradients of enthalpy and entropy, equation (5.8). Figure 5.5 shows the amplification of the in and out of phase normalized main-stream velocity, $w_{sw}^{(1)}/(\epsilon_j W_A)$, due to the shear wave downstream of a $M_s = 1.5$ shock. There is a phase shift in the subsonic range ($M_U/\cos(\theta') < 1$) and none in the supersonic range ($M_U/\cos(\theta') > 1$). All four functions show cusp like minima or maxima at the sonic point, $\theta = \theta_{crit}$.

Pressure wave: The Π_j terms stem from the complementary function, ψ_c, which solves the homogeneous form of equation (5.8), that is, when the vorticity term on right hand side of this equation equals zero. The flow due to the Π_j terms is a compressible, irrotational, plane, longitudinal, sinusoidal wave whose argument is constant along lines which make an angle θ'' with the y-axis. Evidently, the perturbational velocities defined by equations (5.38) and (5.41) fit the special type of flow described by equation (5.22). This implies that pressure perturbation in the downstream flow depends solely on the main-stream velocity component of the Π_j terms through equation (5.23), and so this wave is denoted the post-shock pressure wave.

Equation (5.38) implies that in the subsonic regime the pressure wave is exponentially attenuated with downstream distance from the shock. Figure 5.6 shows the amplification of the in and out of phase components of the normalized main-stream velocity, $w_{pw}^{(1)}/(\epsilon_j W_A)$, due to the pressure wave downstream of a $M_s = 1.5$ shock. As for the shear wave, the out of phase components are non-zero in the subsonic regime $(M_U/\cos(\theta') < 1)$ and zero in the supersonic range $(M_U/\cos(\theta') > 1)$. The amplification of the cross-stream velocity due to the pressure wave, $w_{pw}^{(2)}/(\epsilon_j W_A)$, is obtained from this by multiplication by β_w.

Shock perturbation: The local perturbation in shock inclination angle is

$$\sigma(y) = \sum_{j=1}^{4} \epsilon_j \left(a_j^2 + b_j^2\right)^{\frac{1}{2}} \cos(k' y \cos(\theta') + \delta_{\sigma_j}), \qquad \delta_{\sigma_j} = \arctan \frac{-a_j}{-b_j}. \tag{5.44}$$

The in- and out-of-phase amplification of the shock corrugation, for a $M_s = 1.5$ shock, are shown in figure 5.7. The local deflection from the unperturbed shock plane is obtained by integration of this expression with respect to y. For the upstream vorticity wave, ϵ_1, the shock corrugation progressively lags the initial perturbation till the sonic point is reached. The lag is then $\pi/2$, and is maintained throughout the range $M_U/\cos(\theta') > 1$. For the upstream dilatational and entropy waves, ϵ_2 and ϵ_4, there is a phase opposition between the initial wave and the shock corrugation. As θ is increased this phase lead reduces to $\pi/2$, the value it achieves at the sonic point, and it maintained at this for $\theta > \theta_{crit}$. Finally, for the upstream temperature wave, the initial wave and shock corrugation are in phase at $\theta = 0$. As θ is increased, the phase lead of the corrugations increases to $\pi/2$, which is maintained throughout the supersonic regime.

Thermodynamic variables: Equations (5.23) and (5.24), from section 5.2.3, show how the pressure and density density perturbations may be recovered from the velocity perturbation. Using the linearized Bernoulli equation, along with the equations for the potential component of the velocity perturbation gives,

$$p = \frac{|w_A^{(1)}|}{U_A} p_1 \cos(\mathbf{k}'' \cdot \mathbf{x} + \delta_{p_1}) + \frac{|w_A^{(2)}|}{U_A} p_2 \cos(\mathbf{k}'' \cdot \mathbf{x} + \delta_{p_2}) + \sum_{j=3}^{4} \epsilon_j p_j \cos(\mathbf{k}'' \cdot \mathbf{x} + \delta_{p_j}) \quad (5.45)$$

where

$$\frac{p_j}{P} = -\frac{2\gamma\nu \sec(\theta')}{(\gamma+1)\nu - (\gamma-1)} \Pi_j, \quad (5.46)$$

and Π_j and δ_{p_j} are defined by equations (5.40) and (5.43). The normalized pressure perturbation, p_j/P, for a $M_s = 1.5$ shock are shown in figure (5.8). Equation (5.15) gives the downstream entropy field in terms of the upstream perturbations.

$$\frac{s}{c_p} = \frac{|w_A^{(1)}|}{U_A} \frac{s_1}{c_p} \cos(k'\xi_2 + \delta_{n_1}) + \frac{|w_A^{(2)}|}{U_A} \frac{s_2}{c_p} \cos(k'\xi_2 + \delta_{n_2}) + \sum_{j=3}^{4} \epsilon_j \frac{s_j}{c_p} \cos(k'\xi_2 + \delta_{n_j}), \quad (5.47)$$

where the functions s_j and δ_{n_j} are given in Appendix H (where the limits of many of the constants and transfer functions as $\theta \to \pi/2$ are also derived). The entropy perturbation, s_j/c_p, downstream of a $M_s = 1.5$ shock are shown in figure (5.9). Finally, the linearized equation of state, equation (5.24), is used to recover the density perturbation from the pressure and entropy.

5.4 Remarks

The flow downstream of a perturbed shock, where the perturbations have been induced by the convection of a frozen disturbance in vorticity, dilatation, temperature and entropy through the shock, has been computed. The analysis used to do this is a direct reformulation of Ribner [74]. As the frozen disturbance passes into the shock, a shear-entropy wave and a pressure wave is generated, figure 5.10. The direction and magnitude of these waves have been related to the initial direction and amplitude of the perturbations through a combination of the oblique shock relations, and matching a solution to the linearized Euler equations to the Rankine-Hugoniot jump conditions at the shock. These results have been expressed in a convenient form using refracted

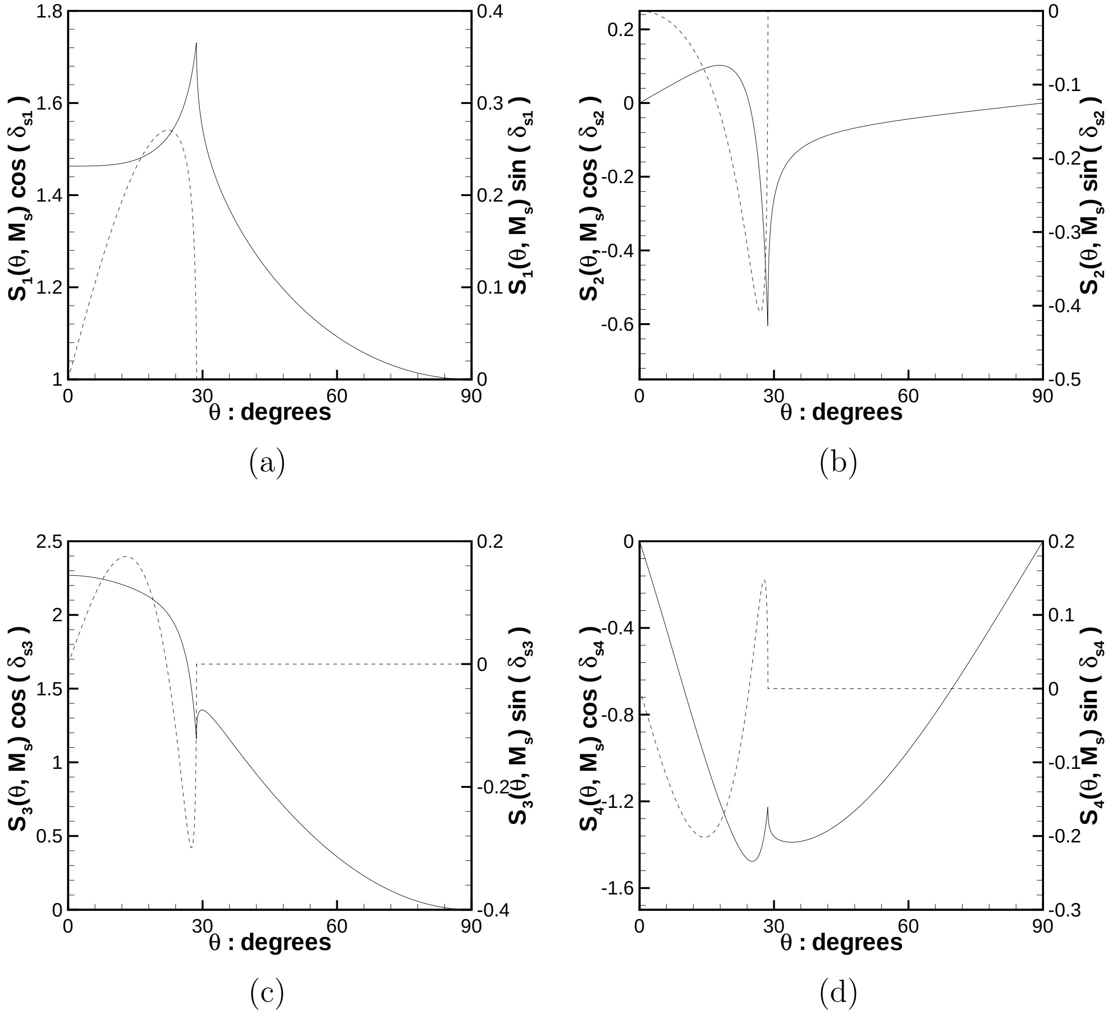

Figure 5.5: Transfer functions S_j. In- and out-of-phase main-stream shear velocity amplification, normalized by $\epsilon_j W_A$, due to passage of a frozen disturbance in vorticity, dilatation, temperature and entropy through a shock, $M_s = 1.5$. $S_j \cos(\delta_{s_j})$ vs. θ (solid), $S_j \sin(\delta_{s_j})$ vs. θ (dashed). (a) j = 1. (b) j = 2. (c) j = 3. (d) j = 4.

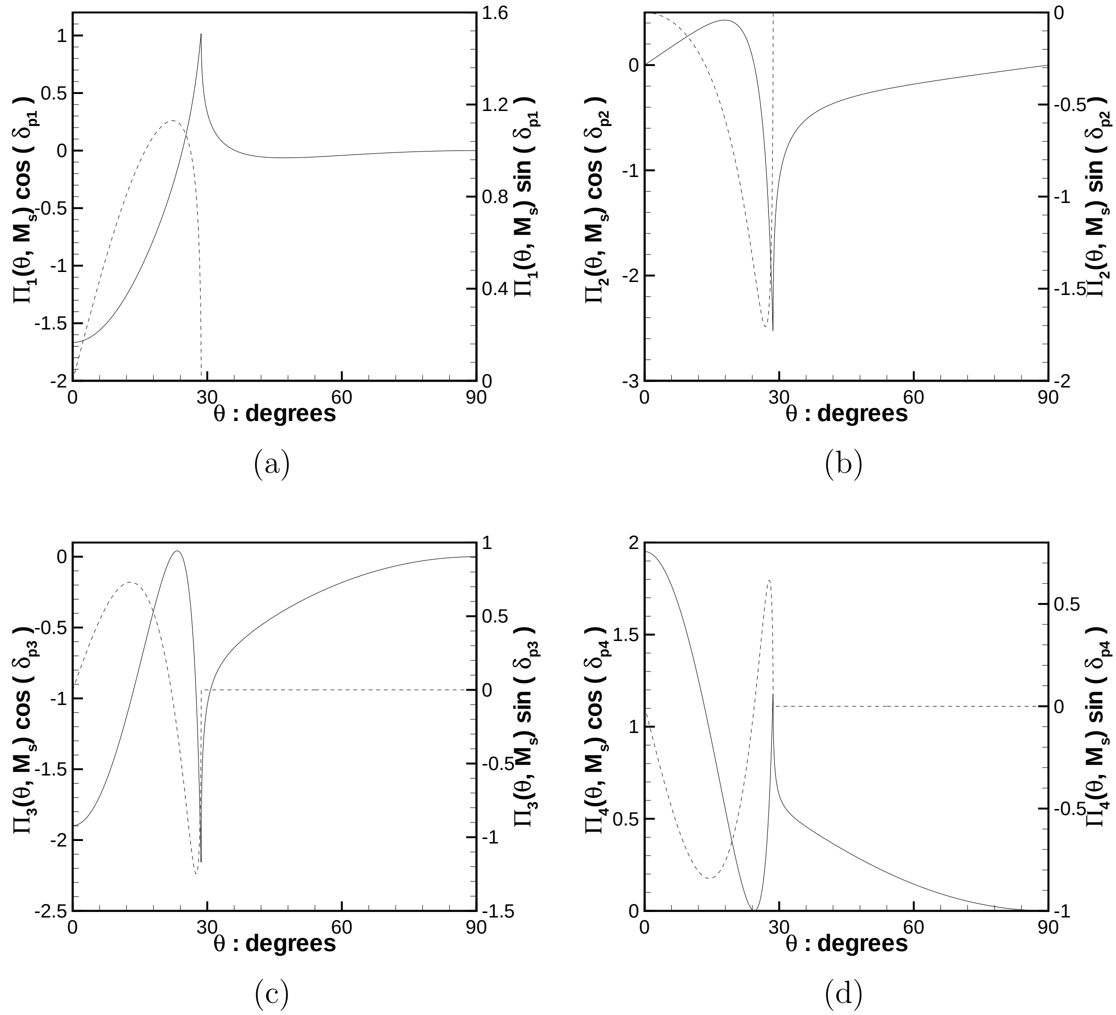

Figure 5.6: Transfer function Π_j. In and out of phase amplification of the main stream velocity component in the pressure wave generated by the passage of the frozen disturbance through a shock, $M_s = 1.5$. $\Pi_j \cos(\delta_{p_j})$ vs. θ (solid), $\Pi_j \sin(\delta_{p_j})$ vs. θ (dashed). (a) j = 1. (b) j = 2. (c) j = 3. (d) j = 4.

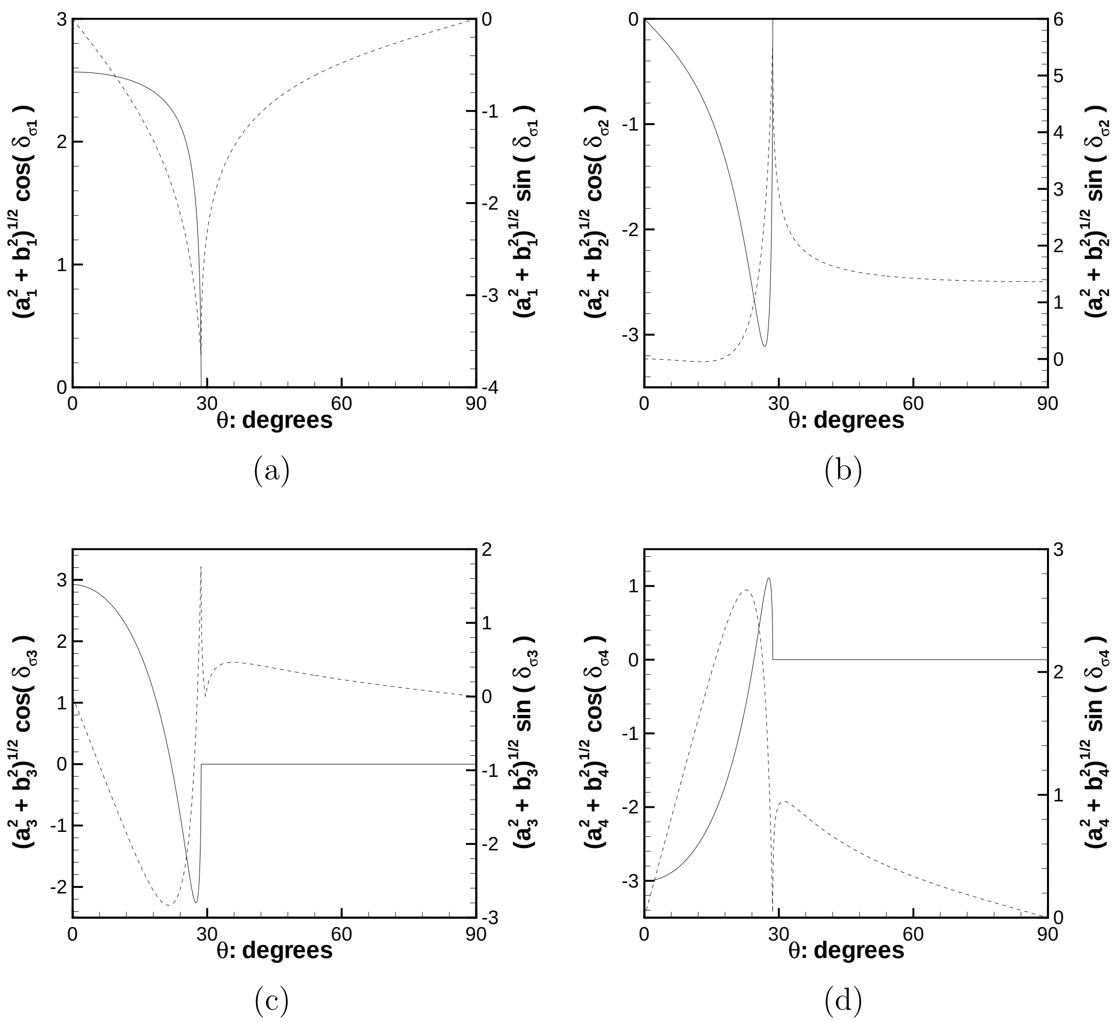

Figure 5.7: In and out of phase amplitude of ripples developed in shock by passage of the frozen compressible disturbance. $\left(a_j^2 + b_j^2\right)^{\frac{1}{2}} \cos(\delta_{\sigma_j})$ vs. θ (solid), $\left(a_j^2 + b_j^2\right)^{\frac{1}{2}} \sin(\delta_{\sigma_j})$ vs. θ (dashed). (a) j = 1. (b) j = 2. (c) j = 3. (d) j = 4.

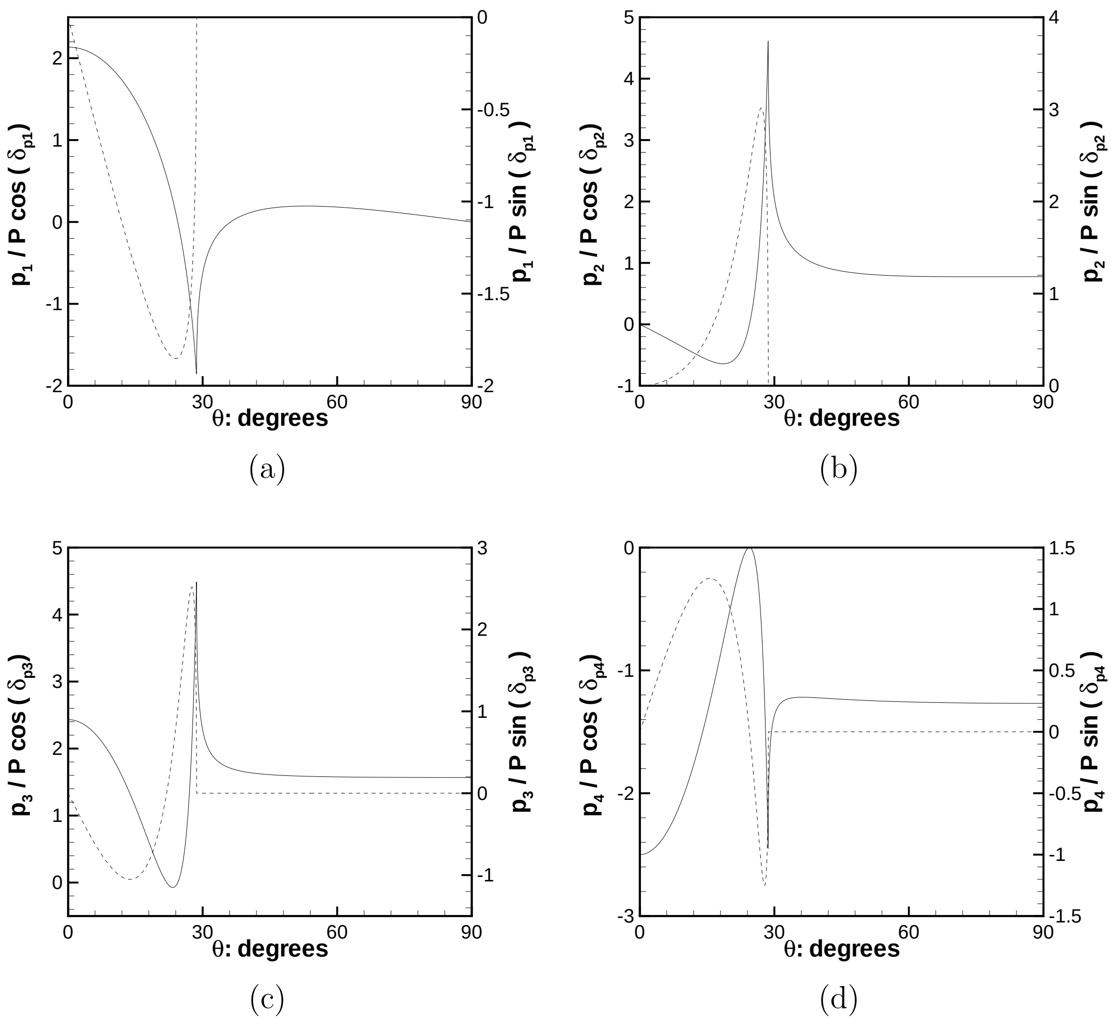

Figure 5.8: In and out of phase pressure amplification downstream of a $M_s = 1.5$ shock. $\frac{p_j}{P}\cos(\delta_{p_j})$ vs. θ (solid), $\frac{p_j}{P}\sin(\delta_{p_j})$ vs. θ (dashed). (a) j = 1. (b) j = 2. (c) j = 3. (d) j = 4.

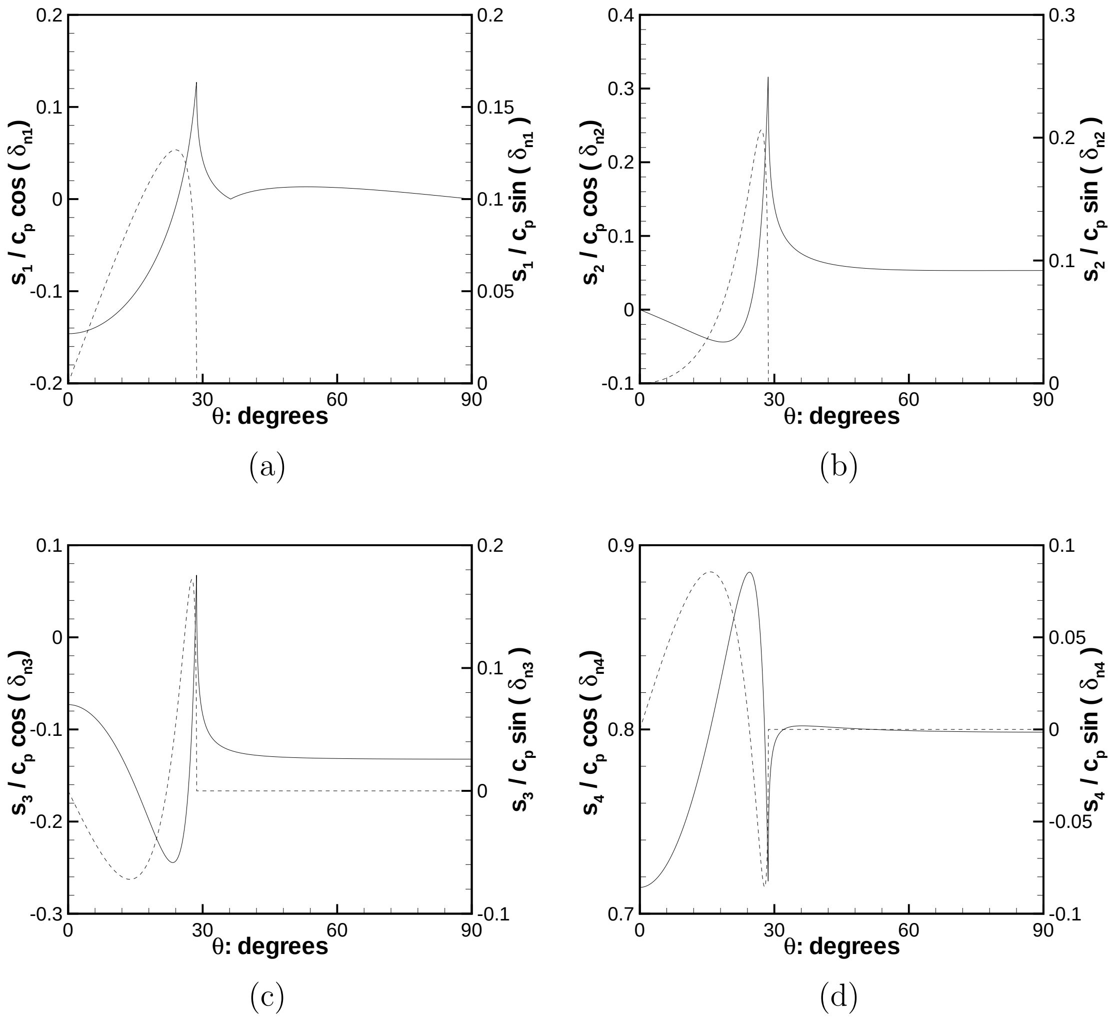

Figure 5.9: In and out of phase entropy amplification downstream of a $M_s = 1.5$ shock. $\frac{s_j}{c_p}\cos(\delta_{n_j})$ vs. θ (solid), $\frac{s_j}{c_p}\sin(\delta_{n_j})$ vs. θ (dashed). (a) j = 1. (b) j = 2. (c) j = 3. (d) j = 4.

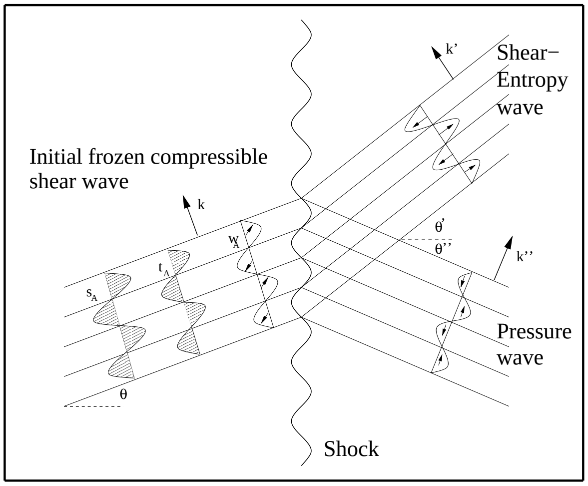

Figure 5.10: Interaction of the frozen sinusoidal disturbance with a planar shock.

wave vectors $\mathbf{k}'$ and $\mathbf{k}''$, the transfer functions S_j and Π_j and the phase lags/leads δ_{s_j} and δ_{p_j}. When the mean velocity in the downstream flow is subsonic both the shear-entropy waves and pressure waves are shifted in phase relative to the initial disturbance. The pressure wave is also exponentially attenuated with downstream distance from the shock. For supersonic downstream flow there are no phase shifts, and the pressure wave has the form of a plane, undamped, sinusoidal sound wave.

The perturbation to the shock inclination angle was also found to be sinusoidal in form, although it is phase shifted with respect to the initial disturbance. In the supersonic range the phase of the ripples on the shock were seen to either lead or lag the upstream perturbations by $\pi/2$.

Chapter 6 Approximate post-shock fields

The small perturbation theory developed in Chapter 5 is applied to the interaction of a planar shock wave with a steady compressible vortex. In particular, approximate post-shock states corresponding to shock-CSV interactions are computed. The passage of the shock is treated as an instantaneous event, an ansatz most suited to weak shocks, although small shock curvature is accounted for. The steady velocity, temperature and entropy fields are Fourier decomposed into a sum of frozen sinusoidal modes. The interaction of each frozen sinusoidal disturbance in the pre-shock vorticity, dilatation, temperature and entropy is computed analytically and then recombined, through Fourier integrals, to give the approximate post-shock fields. The individual upstream modes considered here are not bound by the linearized Euler equations, rather, their sum satisfies the steady non-linear compressible Euler equations exactly. Downstream of the shock it is required that each mode satisfy the linear Euler equations. This approximate theory takes into account the kinematic compression of the vortices, the baroclinic generation of vorticity and the deposition of vorticity due to shock curvature. The evolution of the approximate post-shock fields is compared with numerical solutions to actual initial-value problems. These simulations are done using AMROC, Deiterding [23], [24], [25], in conjunction with Hill & Pullin's [30] tuned-centered-difference-WENO method.

6.1 Overview

The goal of the present study is to devise an approximate technique by which the net effect of the passage of a planar shock through a compressible vortex can be analyzed. In particular, it is desired that this method yield a post-shock vortex, the evolution of which may be studied using a high order numerical scheme. In constructing the approximate method, we attempt to account for the vorticity and

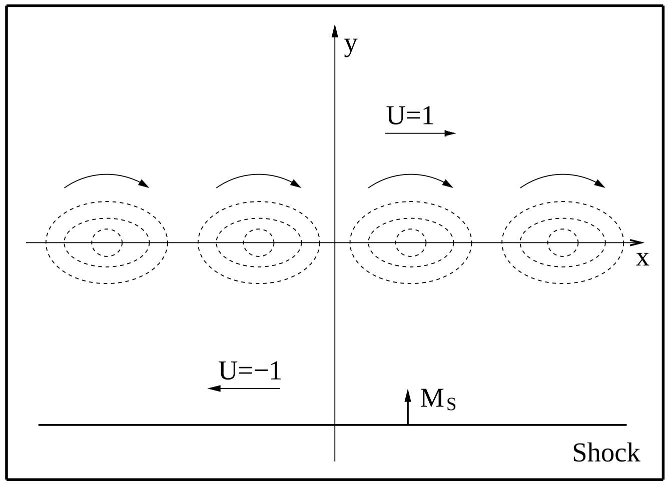

Figure 6.1: Graphical representation of a shock-CSV interaction. Curved lines represent contours of vorticity (dashed implies negative).

density enhancement due to shock compression, the baroclinic generation of vorticity as the shock encounters the variable density field of the compressible vortex, and the deposition of vorticity due to shock curvature.

To this end, we consider the interaction of a shock with a periodic array of compressible vortices in two dimensions, where the shock is aligned with the x-axis and propagates in the positive y-direction, figure 6.1. The shock arrives from $y = -\infty$ with Mach number M_S, where the flow field induced by the array of compressible vortices is uniform. To facilitate the approximate method, we must make two assumptions about the nature of the shock-vortex interaction. Primarily, we restrict the interaction of the shock and the vortex to be of the weak kind, as defined by Grasso and Piozzoli [27]. That is, we do not allow for interactions which exhibit any shock-reflection or other types of complex shock structure. The shock curvature is assumed to remain small as it passes through the vortex. This places a restriction (to be addressed in Section 6.3) on the compressibility of the pre-shock vortices which are considered in this study. Secondly, it is assumed that the interaction takes place instantaneously, so that entire flow field is shocked at time $t = 0$. This supposition is based on two conditions, the first being that the shock transit time through the vortex is small compared with some characteristic vortex time scale. The second, is that once the shock has passed through the vortex, it has little influence on the subsequent evolution of the vortex. This second requisite is best suited to weak shocks, as in a shock stationary frame the normal Mach number behind the shock increases to unity with decreasing shock Mach number. This condition becomes exact in the limit of an acoustic wave, where once the wave has passed through the compressible vortex it no longer exerts any influence on the vortex.

The foundational idea is to Fourier decompose the pre-shock flow fields into frozen sinusoidal modes, the sum of which satisfies the non-linear, steady compressible Euler equations exactly. The interaction of each mode with the shock is computed using the theory developed in Chapter 5, implying that each post-shock mode is required to satisfy the Euler equations linearized about a uniform horizontal flow. The post-shock flow fields are then obtained by Fourier summing these post-shock modes. This is similar to Ribner's [76, 78] work on the sound generated by the interaction of an incompressible vortex with a shock wave, the difference being that currently we using an array of compressible vortices and we estimate all the post-shock fields which are then used in an initial value computation. It will be seen that this method produces an adequate post-shock vorticity field, but does not completely capture the post-shock density or pressure fields.

6.2 Post-shock integrals

The pre-shock velocities in the x- and y-directions are denoted $\overline{u}_A(x, y)$ and $\overline{v}_A(x, y)$, while the pre-shock temperature and entropy fields are $\overline{\tau}_A(x, y)$ and $\overline{s}_A(x, y)$. It's assumed that a reference pre-shock sound speed, C_A, and temperature, T_A, can be defined. The pre-shock fields are Fourier decomposed, where the Fourier components are $\hat{u}_A(\mathbf{k})$, $\hat{v}_A(\mathbf{k})$, $\hat{\tau}_A(\mathbf{k})$ and $\hat{s}_A(\mathbf{k})$. The Fourier vector is $\mathbf{k} = (k_x, k_y)$, where the θ is defined as the angle between $\mathbf{k}$ and the positive k_x-axis. We require that

$$\frac{\hat{u}_A(\mathbf{k})}{M_S C_A} \ll 1, \quad \frac{\hat{v}_A(\mathbf{k})}{M_S C_A} \ll 1, \quad \frac{\hat{\tau}_A(\mathbf{k})}{T_A} \ll 1, \quad \frac{\hat{s}_A(\mathbf{k})}{c_v} \ll 1, \tag{6.1}$$

which ensures the deviation from planar of the incident shock is small, and allows us to use the linear theory described in Chapter 5. It's postulated that associated with each pre-shock Fourier component there is an independent post-shock shear-entropy wave, with wave vector $\mathbf{k}'$, and a post-shock pressure wave, with wave vector $\mathbf{k}''$. The refracted wave vectors make angles of θ' and θ'' with the unperturbed shock, and are determined by the initial wave vector, $\mathbf{k}$, and the shock Mach number, M_S. The amplification of the post-shock waves relative to the pre-shock disturbance can be obtained from the transfer functions, $S_j(\mathbf{k}, M_S)$ and $\Pi_j(\mathbf{k}, M_S)$, prescribed in the previous chapter. For incident angles less than the critical angle, the shear-entropy waves and pressure waves are phase shifted with respect to the incident waves, where the phase-shifts are given by the functions $\delta_{s_j}(\mathbf{k}, M_S)$ and $\delta_{p_j}(\mathbf{k}, M_S)$, also determined in the previous chapter. The transfer functions and phase-shifts have been defined with respect to the main- and cross-stream velocities in Ribner's moving frame of reference. Thus, it proves necessary to decompose the pre-shock velocity into components in these main- and cross-stream directions, which is accomplished by resolving the velocity perturbation $\hat{\mathbf{u}}_A = (\hat{u}_A, \hat{v}_A)$ into components parallel and perpendicular to the wave vector $\mathbf{k}$.

$$\begin{aligned} \hat{u}_A^{(1)}(\mathbf{k}) &= \sin(\theta)\frac{\hat{\mathbf{u}}_A \times \mathbf{k}}{k}, \quad \hat{v}_A^{(1)}(\mathbf{k}) = -\cos(\theta)\frac{\hat{\mathbf{u}}_A \times \mathbf{k}}{k}, \\ \hat{u}_A^{(2)}(\mathbf{k}) &= \cos(\theta)\frac{\hat{\mathbf{u}}_A \cdot \mathbf{k}}{k}, \quad \hat{v}_A^{(2)}(\mathbf{k}) = \sin(\theta)\frac{\hat{\mathbf{u}}_A \cdot \mathbf{k}}{k}. \end{aligned} \tag{6.2}$$

The superscripts (1) and (2) denotes the main-stream and cross-stream directions in Ribner's moving frame of reference. Velocity components in the x and y directions are denoted u and v respectively. The superscript (1) velocity components give the perturbation in upstream vorticity, while the superscript (2) velocity components give the perturbations in upstream dilatation.

Shear-entropy field: The incompressible rotational post-shock velocity field due to the shear-entropy wave is then defined as:

$$
\begin{aligned}
u_{sw}(x,y) = & \int_{-\infty}^{\infty}\int_{-\infty}^{\infty} \frac{\sin(\theta')}{\sin(\theta)} S_1(\mathbf{k}, M_S)\hat{u}_A^{(1)}(\mathbf{k}) e^{i\delta_{s_1}} e^{i\mathbf{k}'\cdot\mathbf{x}} \mathbf{dk} \\
& + \int_{-\infty}^{\infty}\int_{-\infty}^{\infty} \frac{\sin(\theta')}{\cos(\theta)} S_2(\mathbf{k}, M_S)\hat{u}_A^{(2)}(\mathbf{k}) e^{i\delta_{s_2}} e^{i\mathbf{k}'\cdot\mathbf{x}} \mathbf{dk} \\
& + M_S C_A \int_{-\infty}^{\infty}\int_{-\infty}^{\infty} \frac{\sin(\theta')}{\cos(\theta)} S_3(\mathbf{k}, M_S)\frac{\hat{\tau}_A(\mathbf{k})}{T_A} e^{i\delta_{s_3}} e^{i\mathbf{k}'\cdot\mathbf{x}} \mathbf{dk} \\
& + M_S C_A \int_{-\infty}^{\infty}\int_{-\infty}^{\infty} \frac{\sin(\theta')}{\cos(\theta)} S_4(\mathbf{k}, M_S)\frac{\hat{s}_A(\mathbf{k})}{c_v} e^{i\delta_{s_4}} e^{i\mathbf{k}'\cdot\mathbf{x}} \mathbf{dk},
\end{aligned}
\tag{6.3}
$$

$$
\begin{aligned}
v_{sw}(x,y) = & \int_{-\infty}^{\infty}\int_{-\infty}^{\infty} \frac{\cos(\theta')}{\cos(\theta)} S_1(\mathbf{k}, M_S)\hat{v}_A^{(1)}(\mathbf{k}) e^{i\delta_{s_1}} e^{i\mathbf{k}'\cdot\mathbf{x}} \mathbf{dk} \\
& - \int_{-\infty}^{\infty}\int_{-\infty}^{\infty} \frac{\cos(\theta')}{\sin(\theta)} S_2(\mathbf{k}, M_S)\hat{v}_A^{(2)}(\mathbf{k}) e^{i\delta_{s_2}} e^{i\mathbf{k}'\cdot\mathbf{x}} \mathbf{dk} \\
& - M_S C_A \int_{-\infty}^{\infty}\int_{-\infty}^{\infty} \frac{\cos(\theta')}{\cos(\theta)} S_3(\mathbf{k}, M_S)\frac{\hat{\tau}_A(\mathbf{k})}{T_A} e^{i\delta_{s_3}} e^{i\mathbf{k}'\cdot\mathbf{x}} \mathbf{dk} \\
& - M_S C_A \int_{-\infty}^{\infty}\int_{-\infty}^{\infty} \frac{\cos(\theta')}{\cos(\theta)} S_4(\mathbf{k}, M_S)\frac{\hat{s}_A(\mathbf{k})}{c_v} e^{i\delta_{s_4}} e^{i\mathbf{k}'\cdot\mathbf{x}} \mathbf{dk}.
\end{aligned}
\tag{6.4}
$$

The trigonometric fractions present in each of the integrands comes through transforming from Ribner's moving frame of reference, (ξ_1, ξ_2), to the Cartesian frame of reference, (x, y), convected by the mean flow down-stream of the shock, equation (5.37). Recall that we assume the shock-vortex interaction takes place instantaneously, so that $t = 0$. The divergence of the velocity field given by expressions (6.3) and (6.4) is identically zero.

The post-shock entropy field is obtained from the shear-entropy waves by a similar set of integrals, again taking care to transform correctly between the frames (ξ_1, ξ_2) and (x, y). Using the main- and cross-stream velocities in the y direction, the post-shock entropy is,

$$
\begin{aligned}
\frac{s_{sw}(x,y)}{c_p} = &- \int_{-\infty}^{\infty}\int_{-\infty}^{\infty} \frac{1}{\cos(\theta)} \frac{s_1(\mathbf{k})}{c_p} \frac{\hat{v}_A^{(1)}(\mathbf{k})}{M_S C_A} e^{i\delta_{n_1}} e^{i\mathbf{k}'\cdot x} \mathbf{dk} \\
&+ \int_{-\infty}^{\infty}\int_{-\infty}^{\infty} \frac{1}{\sin(\theta)} \frac{s_2(\mathbf{k})}{c_p} \frac{\hat{v}_A^{(2)}(\mathbf{k})}{M_S C_A} e^{i\delta_{n_2}} e^{i\mathbf{k}'\cdot x} \mathbf{dk} \\
&+ \int_{-\infty}^{\infty}\int_{-\infty}^{\infty} \frac{s_3(\mathbf{k})}{c_p} \frac{\hat{\tau}_A(\mathbf{k})}{T_A} e^{i\delta_{n_3}} e^{i\mathbf{k}'\cdot x} \mathbf{dk} \\
&+ \int_{-\infty}^{\infty}\int_{-\infty}^{\infty} \frac{s_4(\mathbf{k})}{c_p} \frac{\hat{s}_A(\mathbf{k})}{c_v} e^{i\delta_{n_4}} e^{i\mathbf{k}'\cdot x} \mathbf{dk}.
\end{aligned}
\tag{6.5}
$$

Note, the above integrals may be written with respect to $\mathbf{dk}'$, where the Jacobian of the transformations is $J(\mathbf{k}, \mathbf{k}') = 1/\nu$.

Pressure field: The velocity perturbations due to the compressible, irrotational pressure wave were seen to decay exponentially fast with downstream distance from the shock, for incident angles less than the critical angle, θ_{crit}. The shock-vortex interaction is assumed to take place instantaneously, so that, in this approximation, at time $t = 0^+$ the shock is located at $y = +\infty$. Therefore, for incident angles less than the critical angle, the contribution of these evanescent waves to the post-shock fields is disregarded. The integrals for the velocity field due to the post-shock pressure waves are:

$$
\begin{aligned}
u_{pw}(x,y) = &\int\int_{|\theta|>\theta_{crit}} \frac{\sin(\theta') + \beta_W \cos(\theta')}{\sin(\theta)} \Pi_1(\mathbf{k}, M_S) \hat{u}_A^{(1)}(\mathbf{k}) e^{i\mathbf{k}''\cdot\mathbf{x}} \mathbf{dk} \\
&+ \int\int_{|\theta|>\theta_{crit}} \frac{\sin(\theta') + \beta_W \cos(\theta')}{\cos(\theta)} \Pi_2(\mathbf{k}, M_S) \hat{u}_A^{(2)}(\mathbf{k}) e^{i\mathbf{k}''\cdot\mathbf{x}} \mathbf{dk} \\
&+ M_S C_A \int\int_{|\theta|>\theta_{crit}} \frac{\sin(\theta') + \beta_W \cos(\theta')}{\cos(\theta)} \Pi_3(\mathbf{k}, M_S) \frac{\hat{\tau}_A(\mathbf{k})}{T_A} e^{i\mathbf{k}''\cdot\mathbf{x}} \mathbf{dk} \\
&+ M_S C_A \int\int_{|\theta|>\theta_{crit}} \frac{\sin(\theta') + \beta_W \cos(\theta')}{\cos(\theta)} \Pi_4(\mathbf{k}, M_S) \frac{\hat{s}_A(\mathbf{k})}{c_v} e^{i\mathbf{k}''\cdot\mathbf{x}} \mathbf{dk},
\end{aligned}
\tag{6.6}
$$

$$
\begin{aligned}
v_{pw}(x,y) = & \int\int_{|\theta|>\theta_{crit}} \frac{\cos(\theta') - \beta_W \sin(\theta')}{\cos(\theta)} \Pi_1(\mathbf{k}, M_S) \hat{v}_A^{(1)}(\mathbf{k}) e^{i\mathbf{k}''\cdot\mathbf{x}} \mathbf{dk} \\
& + \int\int_{|\theta|>\theta_{crit}} \frac{-\cos(\theta') + \beta_W \sin(\theta')}{\sin(\theta)} \Pi_2(\mathbf{k}, M_S) \hat{v}_A^{(2)}(\mathbf{k}) e^{i\mathbf{k}''\cdot\mathbf{x}} \mathbf{dk} \\
& + M_S C_A \int\int_{|\theta|>\theta_{crit}} \frac{-\cos(\theta') + \beta_W \sin(\theta')}{\cos(\theta)} \Pi_3(\mathbf{k}, M_S) \frac{\hat{\tau}_A(\mathbf{k})}{T_A} e^{i\mathbf{k}''\cdot\mathbf{x}} \mathbf{dk} \\
& + M_S C_A \int\int_{|\theta|>\theta_{crit}} \frac{-\cos(\theta') + \beta_W \sin(\theta')}{\cos(\theta)} \Pi_4(\mathbf{k}, M_S) \frac{\hat{s}_A(\mathbf{k})}{c_v} e^{i\mathbf{k}''\cdot\mathbf{x}} \mathbf{dk}.
\end{aligned}
\tag{6.7}
$$

Again, the trigonometric fractions present in each of the integrands results from converting between the moving frame of reference and the present Cartesian frame of reference (x, y). The pressure field is defined as

$$
\begin{aligned}
\frac{p_{pw}(x,y)}{P} = & -\int\int_{|\theta|>\theta_{crit}} \frac{1}{\cos(\theta)} \frac{p_1(\mathbf{k})}{P} \frac{\hat{v}_A^{(1)}(\mathbf{k})}{M_S C_A} e^{i\mathbf{k}''\cdot\mathbf{x}} \mathbf{dk} \\
& + \int\int_{|\theta|>\theta_{crit}} \frac{1}{\sin(\theta)} \frac{p_2(\mathbf{k})}{P} \frac{\hat{v}_A^{(2)}(\mathbf{k})}{M_S C_A} e^{i\mathbf{k}''\cdot\mathbf{x}} \mathbf{dk} \\
& + \int\int_{|\theta|>\theta_{crit}} \frac{p_3(\mathbf{k})}{P} \frac{\hat{\tau}_A(\mathbf{k})}{T_A} e^{i\mathbf{k}''\cdot\mathbf{x}} \mathbf{dk} \\
& + \int\int_{|\theta|>\theta_{crit}} \frac{p_4(\mathbf{k})}{P} \frac{\hat{s}_A(\mathbf{k})}{c_v} e^{i\mathbf{k}''\cdot\mathbf{x}} \mathbf{dk}.
\end{aligned}
\tag{6.8}
$$

The curl of the velocity field given by expressions (6.6) and (6.7) is identically zero. The pressure-wave integrals may be written with respect to $\mathbf{dk}''$, where the Jacobian of the transformations is $J(\mathbf{k}, \mathbf{k}'') = \cos^2(\theta'')/\nu \cos(\theta') \times \partial\theta'/\partial\theta''$. When evaluating any of the the above integrands, care must be taken for $\theta \to 0, \pm\pi/2$. Some of these limits have been computed in Appendix H. The post-shock density field is obtained via the equation of state using expressions (6.5) and (6.8) for the entropy and pressure.

6.3 Shock-CSV interaction

As in Chapter 3, the CSV pre-shock base state is given by $\overline{u}(x, y)$, $\overline{v}(x, y)$ and $\overline{\tau}(x, y)$, representing the velocities in the x- and y-directions and the temperature. The CSV is homentropic, implying that there is no variation in the pre-shock entropy. The subscript ∞ is used to designate uniform, constant, reference, pre-shock quantities as $|y| \rightarrow \infty$, where the flow consists of opposed uniform streams with unit speed. Accordingly, the pre-shock free stream sound speed, Mach number and temperature are c_∞, $M_\infty = 1/c_\infty$ and $\overline{\tau}_\infty$, whereby the reference pre-shock sound speed and temperature are defined as $C_A = c_\infty$ and $T_A = \overline{\tau}_\infty$. The CSV family of solutions is parameterized by M_∞ and the mass flux inside a single vortex core, denoted ϵ, see equation (2.6).

Due to the fact that the theory used to derive equations (6.3)-(6.8) is linear in the pre-shock perturbation to the normal Mach number, it is possible to subtract a hyperbolic tangent profile from $\overline{u}(x, y)$. The pre-shock fields to which Ribner will be applied are defined as:

$$\begin{aligned}
\overline{u}_A(x, y) &= \overline{u}(x, y) - \tanh\left(\frac{\delta(\epsilon, M_\infty)}{\delta(\epsilon, 0)} y\right), \\
\overline{v}_A(x, y) &= \overline{v}(x, y), \\
\overline{\tau}_A(x, y) &= \overline{\tau}(x, y) - \overline{\tau}_\infty, \\
\overline{s}_A(x, y) &= 0.
\end{aligned} \tag{6.9}$$

The factor $\delta(\epsilon, M_\infty)/\delta(\epsilon, 0)$ is the vorticity thickness of the CSV base flow, defined by equation (3.14). As $|y| \rightarrow \infty$, the expressions defined by equation (6.9) decay exponentially fast to zero. These fields are then Fourier decomposed and their Fourier components used in integrals (6.3)-(6.8) to compute the post-shock fields. A condition on the magnitude of the pre-shock velocity and temperature perturbations permitted, equivalent to equation (6.1), is given in terms of the mass flux and the reference sound speed,

$$\frac{\epsilon}{\pi c_\infty M_S} \ll 1, \qquad \frac{\overline{\tau}_A}{\overline{\tau}_\infty} \ll 1, \tag{6.10}$$

where the characteristic length scale for the CSV is taken as π (the length over which the mass flux is defined, equation (2.6)). In the limit as $\epsilon \rightarrow 0$, $\overline{u}_A(x, y)$, $\overline{v}_A(x, y)$ and $\overline{\tau}_A(x, y)$ approach zero everywhere linearly with ϵ, Chapter 2. Thus, in this uninteresting limit the approximate method becomes exact. Conversely, as $\epsilon \rightarrow \infty$ the pre-shock velocities become infinite around the vortex cores, located at

$x = (2n+1)\pi$, $y = 0$, and equation (6.1) is violated. As $c_\infty \to \infty$, the velocity, and temperature perturbations induced by the array of vortices, become vanishingly small when compared to the velocities and temperatures induced by the passage of the shock.

The post-shock velocity in the x-direction due to the hyperbolic tangent is

$$u_{\tanh}(y) = \tanh\left(\frac{\delta(\epsilon, M_\infty)}{\delta(\epsilon, 0)}\nu y\right), \tag{6.11}$$

and is added to integral (6.3) for $u_{sw}(x, y)$. The CSV family of solutions was obtained numerically by MMP using a spectrally accurate technique, as described in Chapters 2 and 3. Thus, the Fourier decomposition and subsequent post-shock reconstruction must also be done numerically, and is described below.

6.3.1 Numerical method

The CSV is periodic in the x-direction, so that the Fourier integrals in dk_x reduce to discrete sums. The functions $\overline{u}_A$, $\overline{v}_A$ and $\overline{\tau}_A$ have been constructed to decay exponentially as $|y| \to \infty$. Thus, the Fourier transform in y may be estimated by applying a finite cut-off to the infinite frequency domain, $(-\infty, \infty) \to (-\eta_0, \eta_0)$. The finite domain $(-\eta_0, \eta_0)$ is discretized, and the Fourier transform approximated by a discrete sum,

$$\begin{aligned} \hat{f}_A(k_x, k_y) &\approx \frac{1}{2\eta_0 N_x} \sum_{m=-\frac{N_x}{2}}^{\frac{N_x}{2}-1} \sum_{n=-\frac{N_y}{2}}^{\frac{N_y}{2}-1} \overline{f}_A(x_m, y_n) e^{-ik_x x_m} e^{-ik_y y_n}, \\ \overline{f}_A(x, y) &\approx \frac{2\eta_0}{N_y} \sum_{m=-\frac{N_x}{2}}^{\frac{N_x}{2}-1} \sum_{n=-\frac{N_y}{2}}^{\frac{N_y}{2}-1} \hat{f}_A(k_x^{(m)}, k_y^{(n)}) e^{ik_x^{(m)} x} e^{ik_y^{(n)} y}, \end{aligned} \tag{6.12}$$

where f_A represents any one of u_A, v_A or τ_A. The collocation points x_m and discrete waves numbers $k_x^{(m)}$ are,

$$x_m = \frac{2\pi}{N_x}\left(m + \frac{Nx}{2}\right), \quad k_x^{(m)} = m, \quad \text{where} \quad m = -\frac{N_x}{2}, \cdots, \frac{N_x}{2} - 1. \tag{6.13}$$

The points y_n are obtained from the Whittaker sampling theorem, which relates them directly to η_0 and N_y,

$$y_n = \frac{\pi}{\eta_0} n, \quad k_y^{(n)} = \frac{2\eta_0}{N_y} n, \quad \text{where} \quad n = -\frac{N_y}{2}, \cdots, \frac{N_y}{2} - 1. \tag{6.14}$$

Once $\hat{u}_A(k_x^{(m)}, k_y^{(n)})$, $\hat{v}_A(k_x^{(m)}, k_y^{(n)})$ and $\hat{\tau}_A(k_x^{(m)}, k_y^{(n)})$ have been obtained, integrals (6.3)-(6.8) are computed using similar forms of the discrete sums given in equation (6.12).

6.3.2 Results

The solutions reported use $[N_x, N_y] = ([128, 1024], [128, 2048], [256, 1024])$, $\eta_0 = (4\pi,\ \tan(\theta_{crit}) N_x/2)$. The later value of η_0 ensures that for each $k_x^{(m)}$, there is a corresponding $k_y^{(n)}$, which when combined compose a wave vector making an angle θ_{crit} with the shock (appropriate when computing the pressure integrals). The different resolutions produced post-shock fields which were invariant in up to four significant figures.

For the shock-vortex problem there is a three-dimensional space of parameters comprising of the pre-shock free stream Mach number, M_∞, the pre-shock mass flux, ϵ, and the shock Mach number, M_S. Post-shock fields were computed over a wide range of these parameters, however, to illustrate the relative merits and deficiencies of the approximate method the subsequent discussion is restricted to a representative set of problem parameters, namely $M_S = 1.5$, $M_\infty = 0.31$, $\epsilon = 0.8871$. The corresponding steady pre-shock vorticity, dilatation, temperature and density fields are shown in figure 6.2. For this combination of parameters the small perturbation approximation is justified, $\epsilon/\pi c_\infty M_S = 0.0584$ and $\overline{\tau}_A(x, y)/\overline{\tau}_\infty \leq 0.041$, yet the pre-shock field is sufficiently compressible so that all the terms from integrals (6.3)-(6.8) should be important. Figure 6.2(d) shows that the minimum to maximum deviation of the pre-shock density field from constant is approximately ten percent of its uniform free stream value. In a shock stationary frame the normal Mach number behind a $M_S =$ 1.5 shock is 0.7011, implying that once the vortex has been processed by the shock,

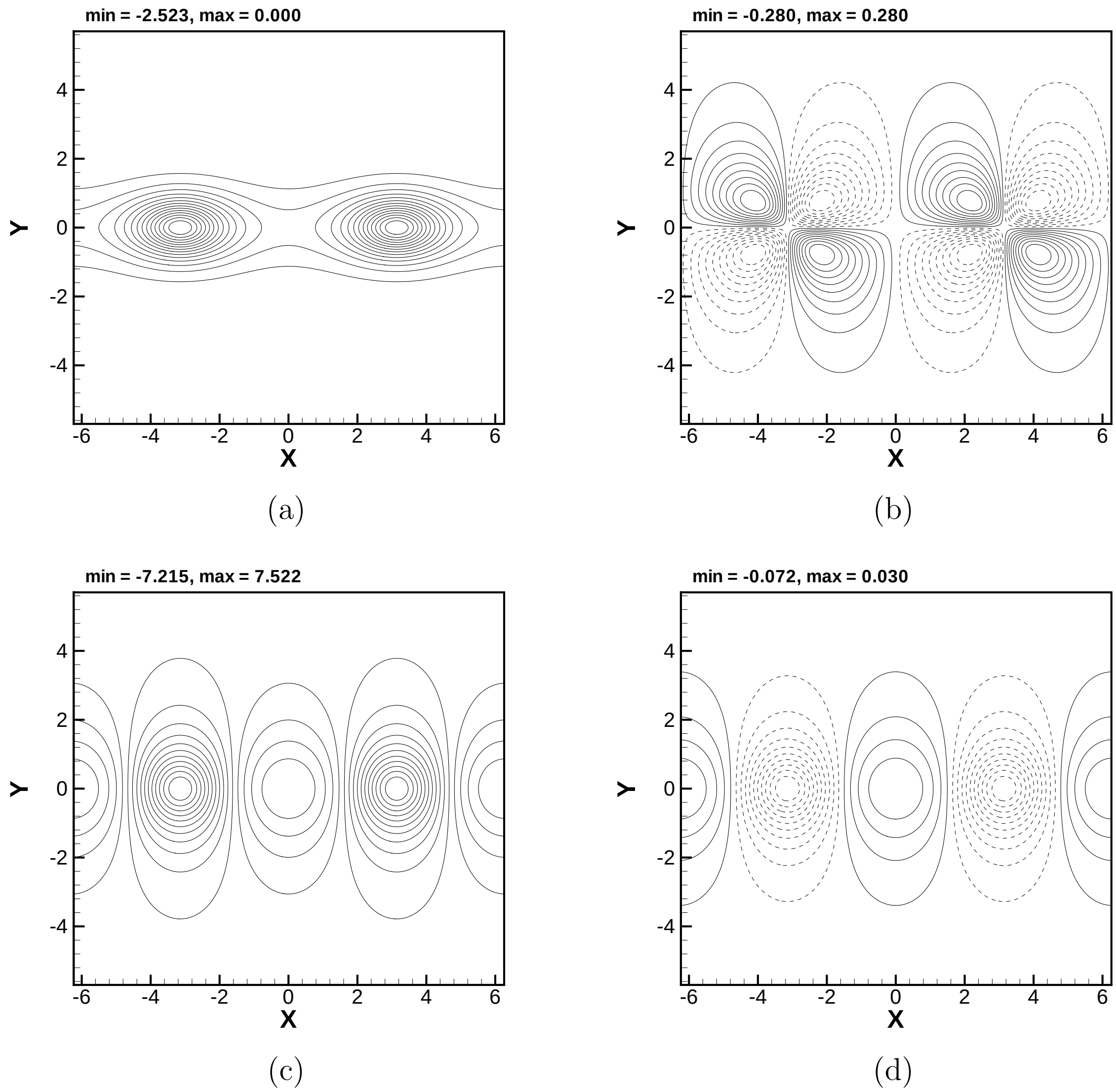

Figure 6.2: Steady pre-shock fields, shown over two periods in x, $M_\infty = 0.31$, $\epsilon = 0.8871$. (a) Pre-shock vorticity, $\nabla \times \overline{\mathbf{u}}(x, y)$. (b) Pre-shock dilatation, $\nabla \cdot \overline{\mathbf{u}}(x, y)$. (c) Pre-shock temperature, $\overline{\tau}(x, y)$. (d) Pre-shock density deviation from the constant, uniform value as $|y| \to \infty$, $\overline{\rho}(x, y)/R_A - 1$, $R_A = \overline{\rho}_\infty = 1.0$.

the shock should have little effect on its subsequent evolution. The approximate post-shock fields, computed via integrals (6.3)-(6.8), for this representative set of parameters are shown in figure 6.3.

Post-shock vorticity: As expected, the post-shock vorticity is enhanced by a factor of approximately ν with respect to the initial vorticity, an effect which is attributed to kinematic compression of the vortices by the shock, see figures 6.2(a) and 6.3(a). The pre-shock vorticity exhibits a two fold symmetry about the x- and y-axes, whereas, the post-shock vorticity is symmetric about the x-axis only. The symmetry is broken by the baroclinic production of vorticity as the shock passes through the compressible vortex. The pre-shock density gradient near the x-axis is predominately in the x-direction and is antisymmetric about the y-axis. When combined with the pressure gradient induced by the shock, it produces vorticity which is also antisymmetric about the y-axis. The variable pre-shock dilatational field contributes very little vorticity to the final post-shock state. An alternative approach to estimating post-shock vorticity, would be to take the incompressible Stuart vortex, and simply compress and enhance it by a factor ν. Figure 6.4(a) shows the difference between the post-shock vorticity obtained by simple compressions and enhancement of an incompressible Stuart vortex and the current theory.

On a side note, varying M_∞, while adhering to the restrictions imposed by condition (6.1), was not seen to change the shape of the post-shock fields significantly, only change their relative magnitudes. The effect of altering ϵ, again without violating condition (6.1), was to change the degree of localization about the vortex cores of the post-shock fields. The most dramatic change to the post-shock fields come from increasing M_S, which increases the amount by which these fields are compressed.

Post-shock dilataion: Intuitively we would expect the post-shock dilatational field to be compressed in a similar fashion to the vorticity field, and be of approximately the same order of magnitude as the pre-shock dilatational field. Nevertheless, figures 6.2(b) and 6.3(b) shows that the current method fails to do this. In fact, the post-

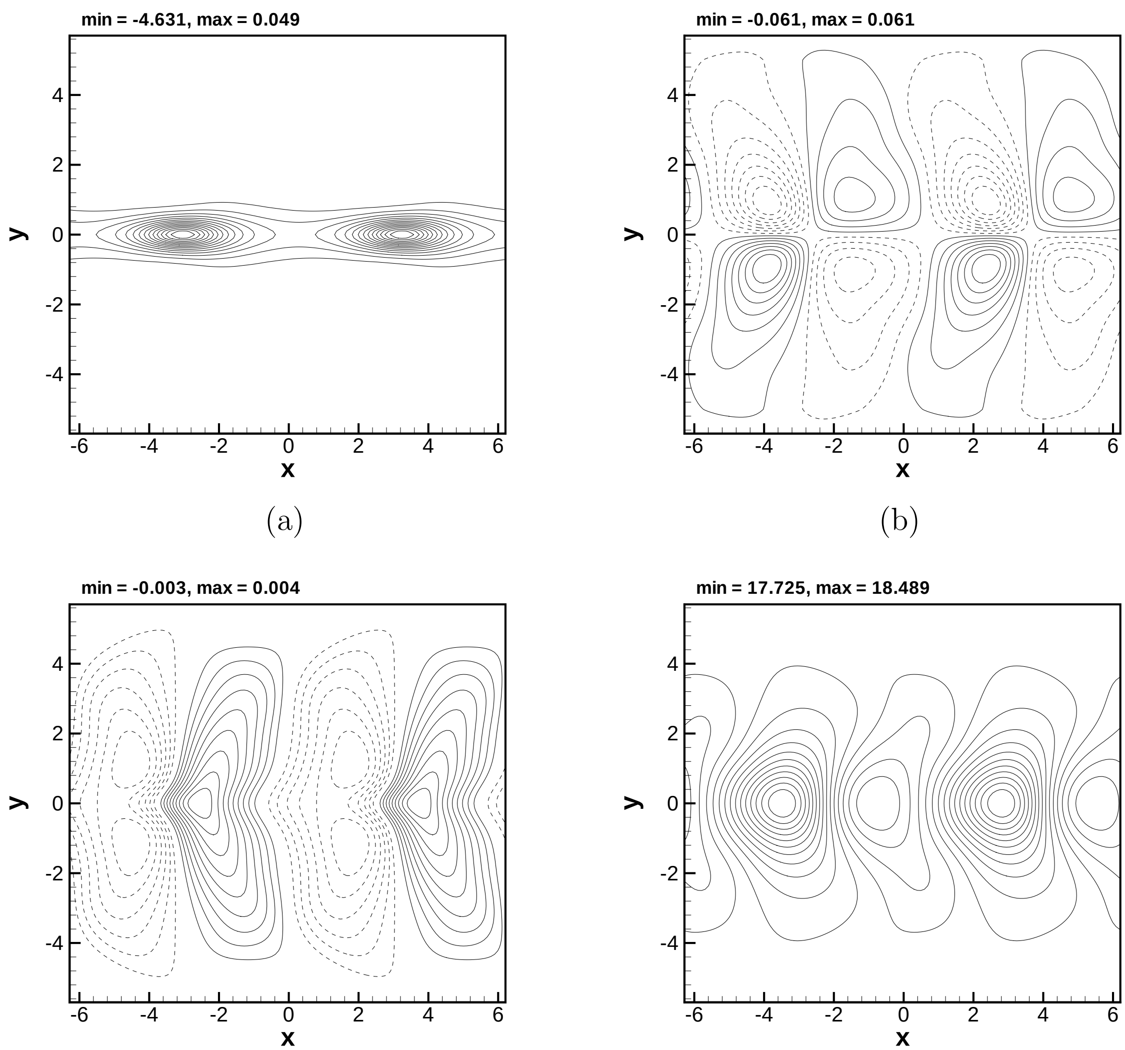

(a) (b) (c) (d)

Figure 6.3: Total post-shock fields, including all the terms from integrals (6.3)-(6.8). $M_S = 1.5$, $M_\infty = 0.31$ and $\epsilon = 0.8871$. (a) Post-shock vorticity. (b) Post-shock dilatation. (c) Post-shock entropy perturbation, s_{sw}/c_v. (d) Post-shock pressure.

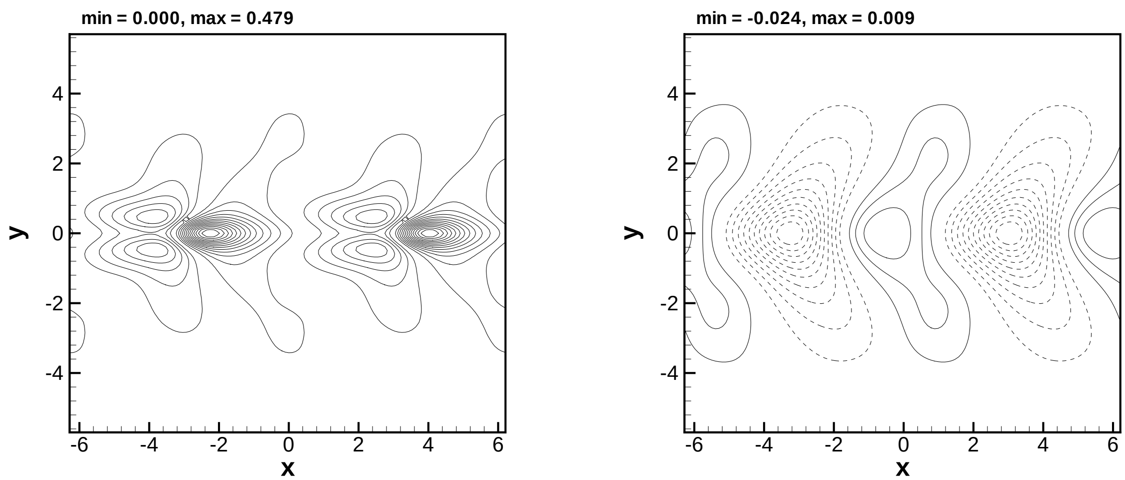

(a) (b)

Figure 6.4: (a) Difference between vorticity computed by the extended Ribner theory, figure 6.3(a), and pure kinematic compression of an incompressible Stuart vortex, $|\nabla \times \mathbf{u}_{sw}(x, y) - \nu\omega_{SV}(x, \nu y)|$, subscript SV implies Stuart vortex. (b) Post-shock density deviation from the constant, uniform value as $y \to \infty$, $\rho_{sp}(x, y)/R - 1.0$, $R = \nu\overline{\rho}_\infty = 1.8621$.

shock dilatation does not appear to be compressed, it's an order of magnitude smaller than the initial dilatation and its sign has been reversed. The velocity components which contribute to the post-shock dilatational fields stem from the pressure waves produced by the pre-shock disturbance, integrals (6.6) and (6.7). The linear equations dictate that for incident angles less than the critical angle, the pressure waves decay exponentially fast with downstream distance from the shock, implying there is no consistent way of including them in the post-shock integrals. It's not clear that a collection of these evanescent waves, when interacting non-linearly, would decay according to the linear equations. Unfortunately, even though the critical angle is small, $\theta_{crit} = 28.6$ for $M_S = 1.5$, it appears that little of the irrotational, compressible, post-shock velocity field is contained in the super-critical angles.

Post-shock pressure and density: The major contribution to the post-shock pressure fields comes from the integral involving $\hat{\tau}_A(\mathbf{k})$ in expression (6.8). Nonetheless, the minimum to maximum variation of the post-shock pressure field is also smaller than expected, due to the lack of inclusion of the sub-critical angles in integral (6.8). This is also manifested in the post-shock density field, which is computed using the equation of state along with the post-shock pressure and entropy fields. Let

$$\rho_{min} = \min_{\mathcal{R}} \rho_{sp}(x,y), \quad \rho_{max} = \max_{\mathcal{R}} \rho_{sp}(x,y),$$
$$\mathcal{R} = \{(x,y) : 0 \leq x \leq 2\pi, -\infty < y < \infty\}.$$

We would expect the ratio $(\rho_{max} - \rho_{min})$ to the uniform free-stream density in the post-shock fluid, $R = \nu$, to be at least as large as (it not larger than) the equivalent ratio in the pre-shock fluid. For the representative set of problem parameters, this ratio is 0.102 for the pre-shock density, and 0.033 for the post-shock density, figures 6.2(d) and 6.4(b), indicating that at least seventy percent of the density perturbation has been lost to the sub-critical angles.

The vertical velocities induced by the pre-shock vortex increase the normal shock Mach number on the left side of a vortex core, and decrease it on the right. This in turn induces larger jumps in pressure and density on one side of the vortex core than on the other, thereby breaking the symmetry of the pre-shock pressure and density fields with respect to the y-axis. Perhaps a success of the present method is that it captures the symmetry breaking of the pre-shock flow, figures 6.3(d) and 6.4(b), however it fails to give a reasonable prediction for the magnitude of the variation from constant of the post-shock pressure and density fields.

6.4 AMROC simulations

To further test the effectiveness of the current method, the post-shock vortex array produced by integrals (6.3)-(6.8) is evolved forward in time numerically. The evolution of this approximate field is then qualitatively compared with the numerical solution to the actual initial-value problem. By this, we mean a simulation in which the passage of the shock through the array of compressible vortices is computed numerically, rather than approximated as an instantaneous event at time zero. Thus, we are solving two initial value problems numerically. The first is referred to as Ribner, whereby the initial fields are given by integrals (6.3)-(6.8). In the second, referred to as the initial-value problem, the initial profile is the pre-shock CSV, figure 6.3. On these fields, at a large negative value of y where the velocity and density are uniform, a shock is painted into the flow. Across the shock the velocity, pressure and density jumps satisfy the Rankine-Hugoniot jump conditions.

To compare the two set of computations a virtual time origin must be chosen. For the approximate Ribner method the fields are held frozen till the shock has moved far away from the array of vortices. This is assumed to happen immediately, implying the post-shock fields are evaluated at time $t = 0$. For the initial-value problem, there is no way to hold the vortices frozen till the shock has left their vicinity. They begin to evolve as soon as the shock-vortex interaction begins. Thus, choosing a time origin for the initial value problem is somewhat subjective, and is done presently by setting time $t = 0$ as the time at which the shock has just passed through the vortex cores.

AMROC: The numerical simulations are done with AMROC, Deiterding [23], [24], available at [25]. AMROC provides a general object-oriented framework implementation, in C++, of an adaptive mesh refinement algorithm. It's a special version of the block-structured algorithm of Berger & Oliger [3], which is designed principally for the adaptive solution of hyperbolic partial differential equations. AMROC has been implemented using an efficient parallelization strategy for distributed memory machines, and the codes run on all high-performance computers that provide the MPI-library. It also has an automatic time-step algorithm, based on the CFL condition.

TCD-WENO scheme: A hybrid tuned-centered-difference-WENO method (TCD-WENO), developed and provided by Hill & Pullin [30], is used to calculated the fluxes for AMROC's conservative time explicit finite-volume scheme. Given a stencil width, all finite difference schemes have a maximum formal order of accuracy which can be achieved. The underlying idea for the TCD method is not to choose Taylor coefficients which give this maximum formal order of accuracy, but rather choose the coefficients so the scheme is optimal in some other sense. Hill & Pullin [30] used a method proposed by Ghosal to optimize their Taylor coefficients in the LES sense, essentially choosing a set which give an optimal modified wave number behavior. Thus a given five point stencil can yield a formally second order scheme with superior modified wave number behavior to the corresponding formally fourth order method. In this way, using a small local stencil suitable for AMR, a highly non-dissipative scheme can be constructed. Hill & Pullin [30] married their TCD scheme to WENO by specifying optimal WENO weights to match those of the TCD scheme, where it's expected that these weights will be achieved automatically in regions of smooth flow away from shocks. Consequently, their method excels at capturing moving discontinuities, such a shocks, is highly non-dissipative in smooth regions away from shock and uses a small stencil width which makes it suitable for AMR and complex boundary conditions.

In practice Hill & Pullin found that a switch was necessary. The switch is based on a measure of the smoothness of the candidate WENO stencils used to compute the interpolated flux values on the half grid points. If the variance of this smoothness measure is greater than a user specified threshold then WENO is used, if not, the fluxes are computed using the TCD scheme. Presently, as resolution is not an issue and we are not doing LES, a low value of this threshold is prescribed, so that WENO is active at the shock and inside the compressible vortices. The TCD scheme is numerically less intensive when evaluating fluxes, so effectively it is used only to reduce the computational time.

Simulation parameters: For the simulations presented a computational domain $\mathcal{R} = \{(x, y) : 0 \leq x < 2\pi,\ -4\pi \leq y \leq 4\pi\}$, shown in figure 6.5, was used with a base resolution of [300×1200] or [600×2400] cells. Two levels of factor two refinement was allowed, with a refinement criterion based on density gradients so that refinement was restricted to the shock. A five point WENO-TCD stencil was used, implying the scheme is formally second order, with a WENO-TCD threshold (λ_{max} in Hill & Pullin's notation) of 1.0. Both problems are set up so that the post-shock

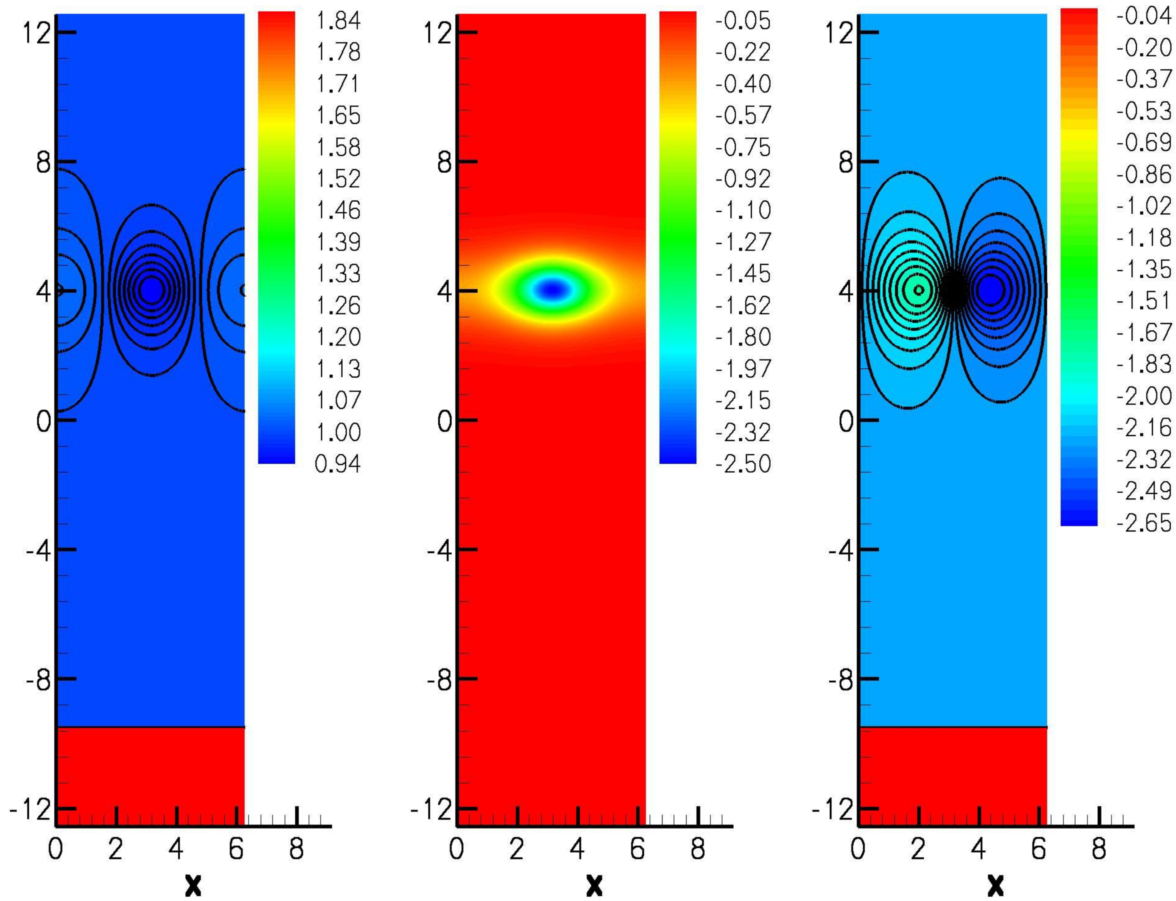

(a) (b) (c)

Figure 6.5: Computational domain shown for the initial-value problem (the same domain is used to evolve the approximate Ribner fields forward in time). The shock was initialized at $y = -9.5$. The base resolution shown is $[300 \times 1200]$, the left and right hand boundaries are periodic, while the top and bottom are zero gradient. (a) Density. (b) Vorticity. (c) Vertical velocity, $v(x, y)$.

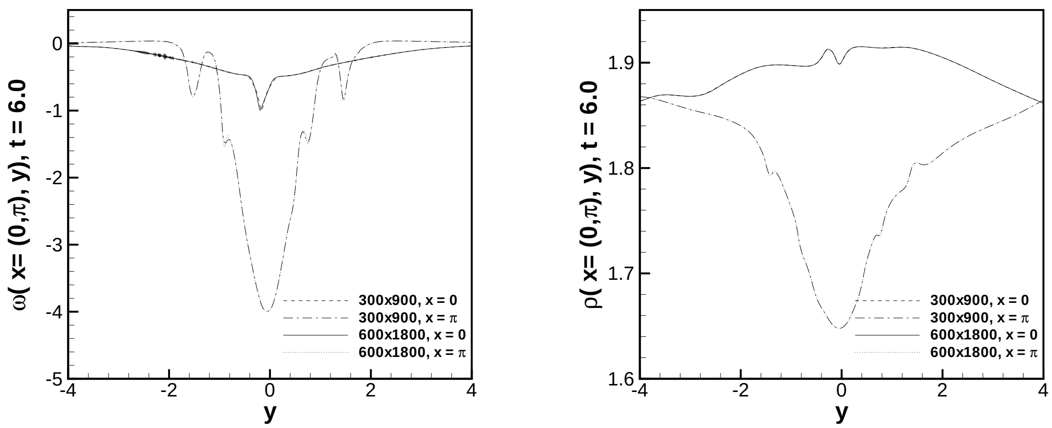

(a) (b)

Figure 6.6: Vorticity and density profiles along the lines $x = 0$ and $x = \pi$, $-4 \leq y \leq 4$ at time $t = 6.0$. Initial condition given by the approximate Ribner method, integrals (6.3)-(6.8), $M_S = 1.5$, $M_\infty = 0.31$ $\epsilon = 0.8871$. Base resolutions [300×1200] and [600×2400]. (a) Vorticity. (b) Density.

fluid has zero mean velocity in the lab fixed frame. Periodic boundary conditions are used for the left and right hand boundaries, with zero gradient conditions on the top and bottom boundaries. The zero gradient condition at the top boundary produces a reflected wave in the initial-value simulation when the shock passes out of the domain. The initial-value simulations are run till this reflected arrives back at the post-shock vortex array. The method used to initialize shocks in the initial-value problem leaves a small startup error as the Rankine-Hugoniot shock is evolved forward in time and smears into a numerical shock. This numerical artifact remains at the initial shock location throughout the simulation. Therefore, for the initial-value problem the shocks are initialized at $y = -9.5$, see figure 6.5, so that this spurious wave is far from the evolving post-shock vortices. Convergence was tested by comparing results from different resolution runs, see for example figure 6.6, which show very good agreement over the total simulation run times. The base flows are chosen so that the shock curvature remains small throughout the initial-value simulations.

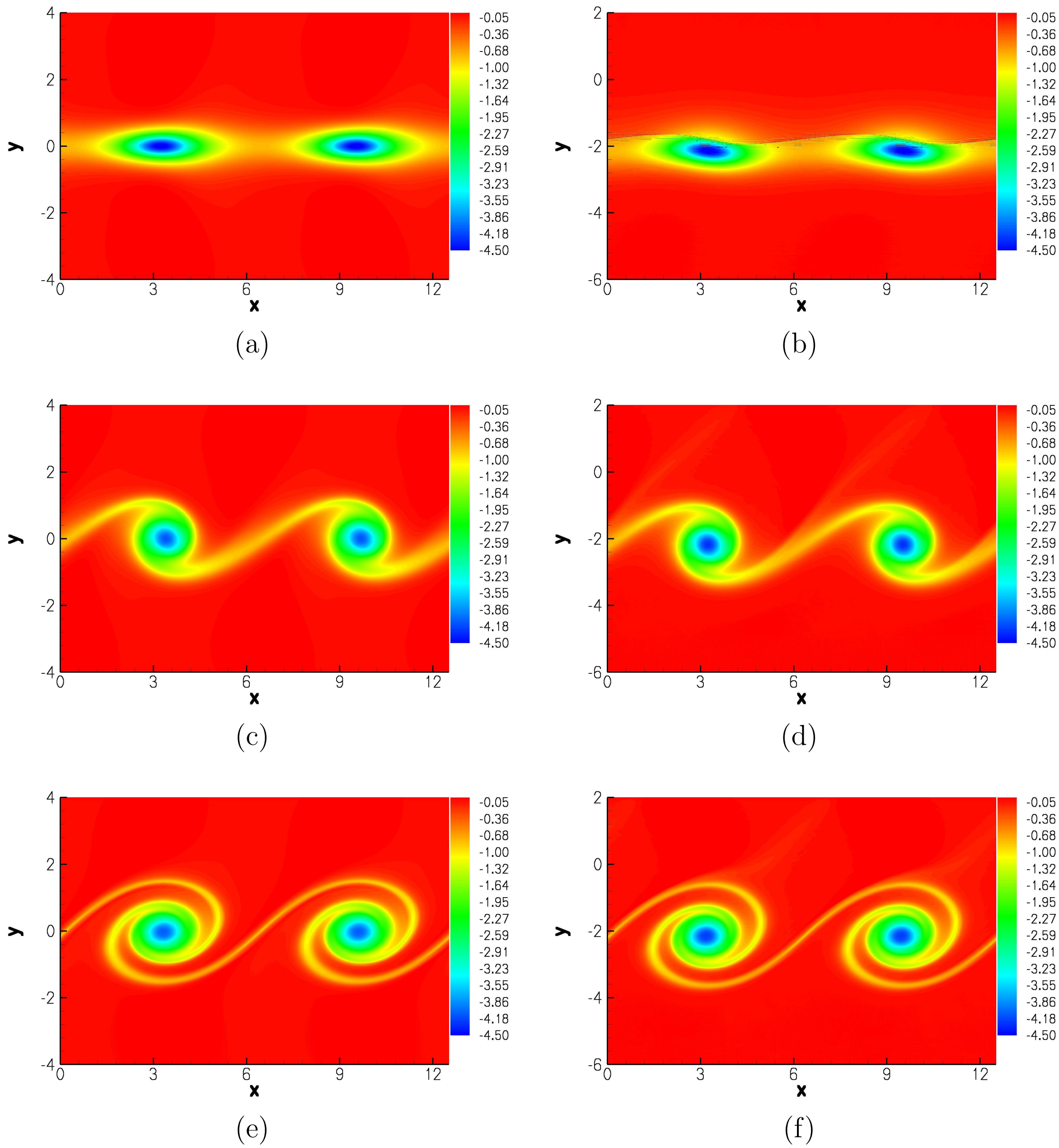

Figure 6.7: Vorticity computed using AMROC: $M_S = 1.5$, $M_\infty = 0.31$, $\epsilon = 0.8871$. In the left-hand column the initial condition is given by integrals (6.3)-(6.5), that is by the approximate Ribner method. The right-hand column is obtained by letting the shock interact with the steady CSV numerically. (a) t = 0.0. (b) t = 0.0. (c) t = 3.0. (d) t = 3.0. (e) t = 6.0. (f) t = 6.0.

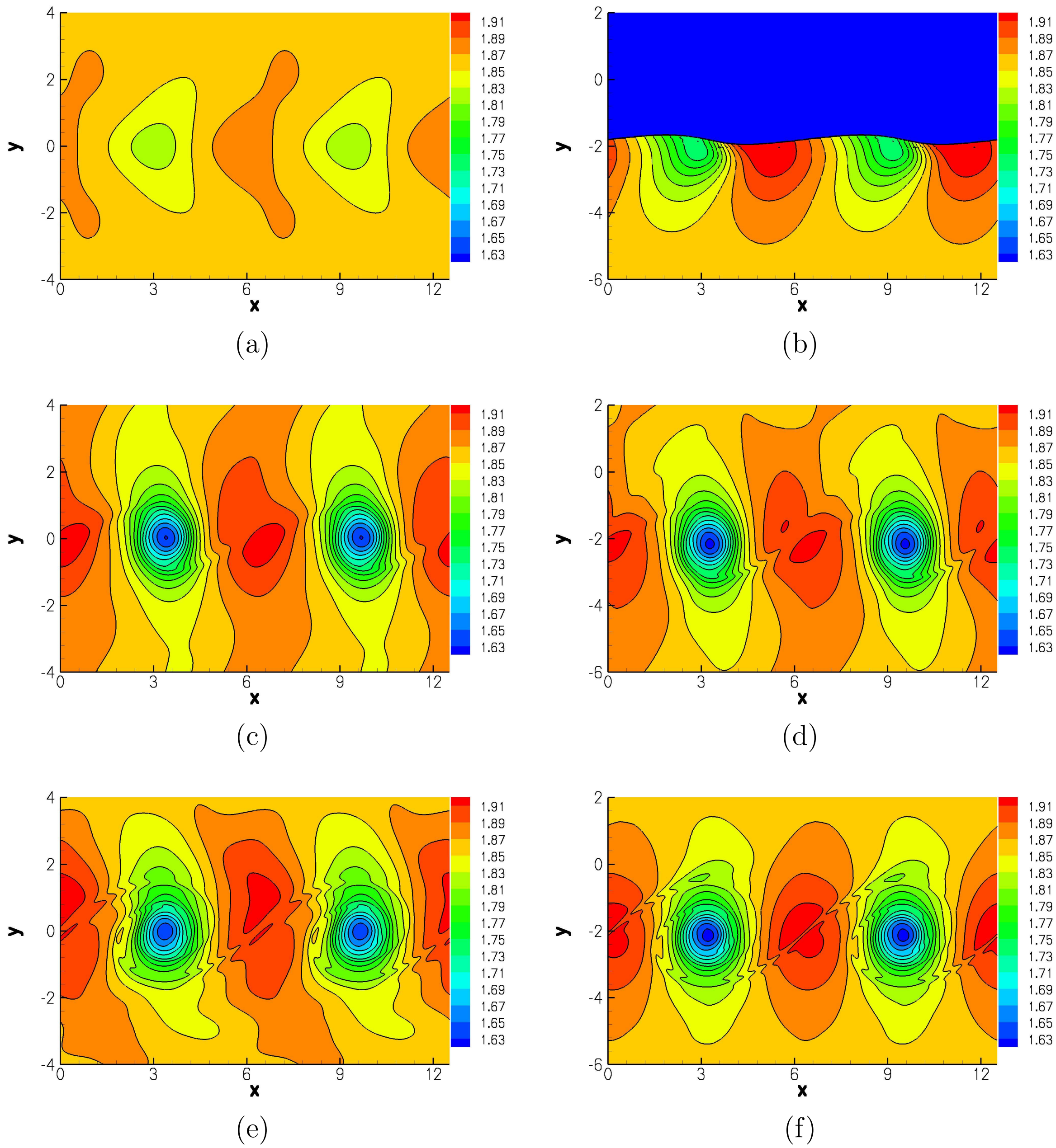

Figure 6.8: Density computed using AMROC: $M_S = 1.5$, $M_\infty = 0.31$, $\epsilon = 0.8871$. In the left hand column the initial condition is given by integrals (6.3)-(6.5), that is, by the approximate Ribner method. The right hand column is obtained by letting the shock interact with the steady CSV numerically. (a) t = 0.0. (b) t = 0.0. (c) t = 3.0. (d) t = 3.0. (e) t = 6.0. (f) t = 6.0.

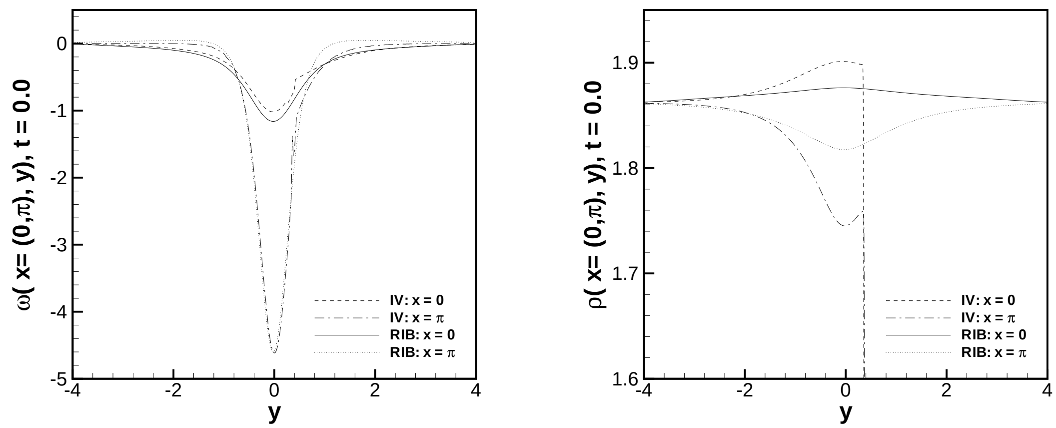

(a) (b)

Figure 6.9: Cross sections of the vorticity and density fields at $x = 0.0$ and $x = \pi$, $-4 \leq y \leq 4$, time $t = 0$. $M_S = 1.5$, $M_\infty = 0.31$, $\epsilon = 0.8871$. IV $\rightarrow$ initial value problem, RIB $\rightarrow$ approximate Ribner method. (a) Vorticity. (b) Density.

Results: Figures 6.7 and 6.8 show the evolution of post-shock vorticity and density fields respectively. The vorticity in figure 6.7(a) and density in figure 6.8(a) are computed using the approximate Ribner technique, while figures 6.7(b) and 6.8(b) show the corresponding fields for the time defined as zero from the initial-value calculation. Figure 6.9 shows cross sections of these vorticity and density fields at $t = 0$. The irregularity in the initial-value problem's vorticity cross section comes from the presence of the shock, which has just passed through the vortex core. Figure 6.10 show similar cross sections for the later times: $t = 3.0$ and $t = 6.0$.

Clearly, the approximate method is good at computing an initial vorticity distribution, figure 6.9(a), but underestimates the density variations, figure 6.9(b). At this value of M_∞, the flow is dominated by vorticity. Owing to this, the later time approximate Ribner and initial-value problem's density fields tend to look very similar, figures 6.10(b) & (d). The maximum value of vorticity decreases more rapidly for the approximate post-shock field than for the pure initial value problem. Never the less, their structures are akin over the total run time, 6.10(a) & (c). The faster decrease was found to be resolution independent. It's due to the poor initial density

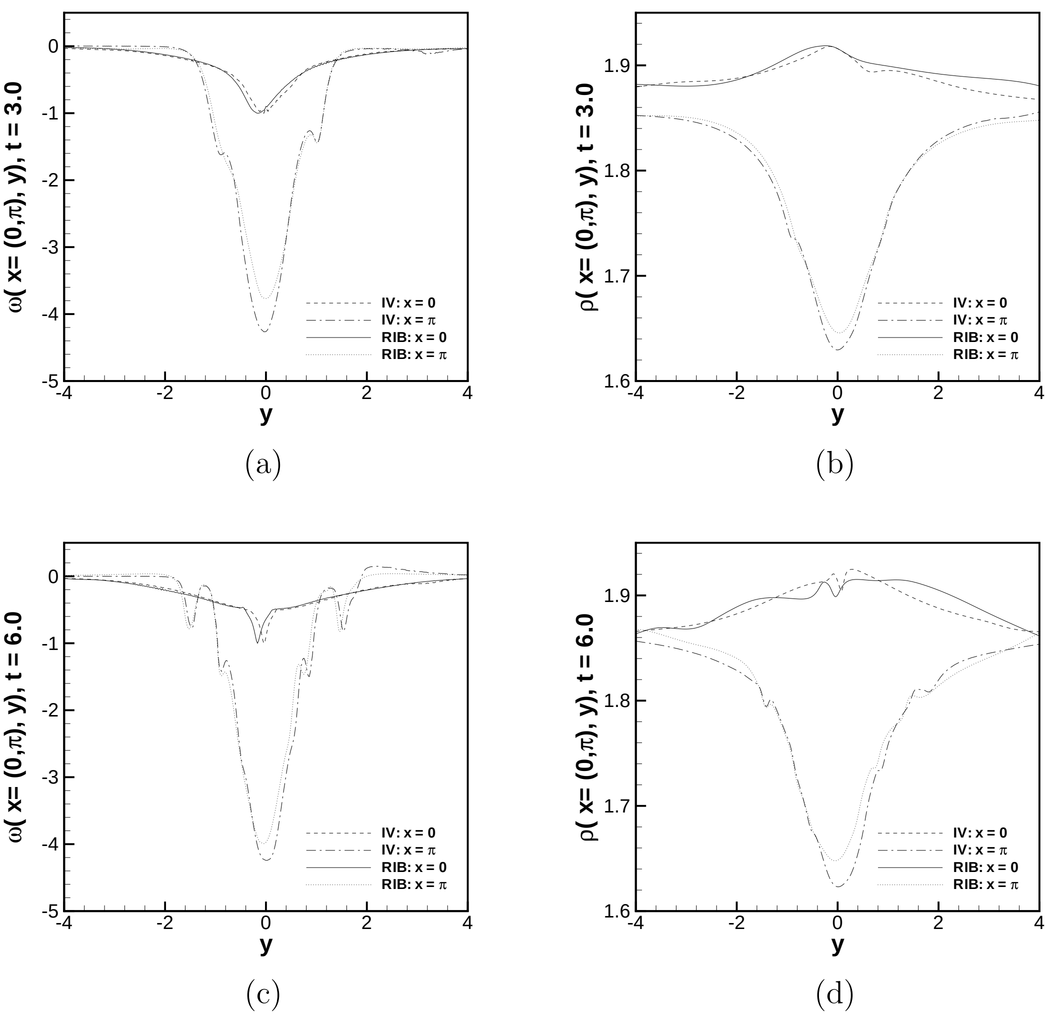

Figure 6.10: Cross-sections of the vorticity and density fields at $x = 0.0$ and $x = \pi$, $-4 \leq y \leq 4$. $M_S = 1.5$, $M_\infty = 0.31$, $\epsilon = 0.8871$. (a) Vorticity, $t = 3.0$. (b) Density, $t = 3.0$. (a) Vorticity, $t = 6.0$. (b) Density, $t = 6.0$.

and pressure fields produced by the approximate method.

The initial-value problem allows us to test the hypothesis that if condition (6.1) restricting the magnitude of the pre-shock perturbations is meet, then the shock curvature should stay small throughout the interaction. This was certainly found to be the case for the present representative set of problem parameters, see figure 6.8(b). For $M_\infty \gtrsim 0.4$, $\epsilon = 0.8871$, the shock begins to develop a complicated structure as it passes through the compressible vortex array, implying the the current approximate method would not longer be appropriate.

6.5 Remarks

A semi-analytical method for estimating post-shock fields has been developed. This was done by Fourier decomposing the initial velocity, temperature and entropy fields into a sum of frozen sinusoidal modes. The small perturbation theory developed in Chapter 5 is used to analytically compute the interaction of each frozen mode with the incident shock wave. Finally, these post-shock modes are numerically summed, thereby reconstructing the approximate post-shock fields. This method was then applied to the shock-CSV interaction.

The post-shock fields produced by this method were numerically evolved forward in time using AMROC combined with Hill & Pullin's [30] WENO-TCD method. Results from these computations were then qualitatively compared with results from an initial-value problem in which the shock is treated numerically. The approximate method was seen to produce a reasonable estimate of the post-shock vorticity and entropy fields, but does rather poorly when used to evaluate the post-shock dilatation, pressure and density. A possible future study would be to develop a consistent method to include the sub-critical angels in integrals (6.6)-(6.8). This would certainly improve the approximate post-shock pressure and density fields produced by this method and greatly extend its potential domain of usefulness.

Chapter 7 Conclusions and outlook

To assay the stability of the spatially nonuniform compressible Stuart vortices (CSV) a normal-mode assumption in conjunction with a spectral-collocation method was used. This problem was partially motivated by the link drawn between the linear stability of the constant density profile and the steady CSV base flow. As a physical model for the dynamics of compressible shear layers, the CSV structure is not without limitations. Principally, at a fixed mass flux within a vortex core, the homentropic solution branch terminates at a subsonic free stream Mach number. Moreover, DNS of compressible vortices show entropy variations in the core. Nonetheless the CSV provides a useful base-state for assessing the effect of compressibility on the stability properties of nonuniform compressible flows.

Three main classes of instabilities on the CSV were investigated; subharmonic, translative and a new parallel mode, each within the parameter space of the free-stream Mach number, the mass flow inside a closed vortex core and the wavenumber space of the perturbations. The largest growth rates consistently correspond to either the subharmonic or fundamental streamwise frequencies. For low Mach numbers the subharmonic mode is dominant, it maximizes for eigenmodes with no spanwise variation, and is linked to an instability of the pairing type. As the Mach number increases this perturbation becomes three dimensional and the term pairing instability no longer applies, since it can no longer be interpreted as an initiating mechanism for interactions between neighboring vortices. Not only do the subharmonic instabilities loose their ability to pair neighboring vortices at higher Mach numbers, but this instability becomes sub dominant to the more vigorous translative instability, which shows a broadband nature with respect to spanwise wave numbers. This is in agreement with experimental observations that compressible shear layers are largely inert, and show structures at every possible oblique angle to the streamwise direction.

Interestingly, the parallel instability which might be interpreted physically as having initiated a primary roll up producing a CSV-like structure, remains active and relatively unaltered over the base-flow parameter range. The persistence of this instability for the the strongly nonlinear CSV flows may explain the success of linear growth rates, obtained from parallel shear flows, in postdicting experimentally observed growth rates in the compressible turbulent mixing layer.

We remark that the two-dimensional continuations of the finite mass flux CSV from a parallel flow is not unique. Firstly, a continuation from a three-dimensional neutral stability point of the constant density hyperbolic tangent profile is possible. Since the relevant stability curves do not terminate when the free-stream Mach number becomes supersonic, this may enable the construction of vortical, three-dimensional, globally supersonic solutions to the steady compressible non-linear Euler equations. Secondly, a continuations from the steady stability point of a Crocco-Busemann parallel profile may also be possible. This could lead to CSV states with more realistic entropy profiles inside the vortex cores.

The Mallier & Maslowe vortex (MMV) is a two-dimensional solution to the steady, incompressible Euler equations parameterized by the mass flow rate between adjacent vortex cores. Two distinct continuations of the MMV into the compressible regime have been proposed. Under the first strategy, denoted solution A, the mass flow rate is fixed at its incompressible value as the free stream sound speed is reduced. This formulation yielded solution branches which, for a given mass flux, terminate at the onset of locally supersonic flow. The terminations is thought to be due to the onset of weak, almost entropy preserving shocks in the supersonic region (which is located on the vortex core boundary). Increasing compressibility increases the normalized strain rate at the vortex cores, elongating them in the vertical direction.

An alternative formulation (denoted solution B) in which the mass flux is computed, rather than held fixed, as the free stream sound speed is decreased, was also investigated. This formulation procedure led to two classes of eventual states. For the first, increasing compressibility causes the mass flow rate between adjacent vortex cores to asymptote to zero, implying that the branch is approaching a quiescent flow. The second termination mode allowed large regions of smooth supersonic flow to evolve, and was thought to be due to the large vertical dilatational gradients inside the supersonic region. An interesting variation on formulation B solution branches, would be to look for a bifurcation to solutions where the stagnation points at the vortex cores become hyperbolic. As a future project, the two- and three-dimensional stability characteristics of the CMMV could be explored using the techniques developed for CSV. This would allow the effect of compressibility on the Crow and elliptical instabilities associated with such flows to be explored.

Finally, we developed a method to compute approximate post-shock fields produced by shock-compressible-vortex interactions. This was done in two stages. Firstly, the flow downstream of a perturbed shock, where the perturbations are induced by the convection of a frozen disturbance in vorticity, dilatation, temperature and entropy through the shock is computed (the analysis used is a direct reformulation of Ribner [74]). The direction and magnitude of the shear-entropy and pressure waves produced are related to the initial direction and amplitude of the perturbations through a combination of the oblique shock relations, and matching a solution to the linearized Euler equations to the Rankine-Hugoniot jump conditions at the shock. Secondly, the initial velocity, temperature and entropy fields induced by the pre-shock vortices are Fourier decomposed into a sum of frozen sinusoidal modes. The passage of the shock is treated as an instantaneous event, so that the interaction of each frozen mode with the shock can be treated independently. Post-shock fields are constructed by summing the resulting post-shock shear-entropy and pressure waves.

This theory was used to compute approximate states corresponding to shock-CSV interactions, which were then numerically evolved forward in time using AMROC. The method was verified by comparing results with simulations in which the shock is treated numerically. The approximate method does a good job at capturing the post-shock vorticity produced by shock compression, baroclinic generation, and shock curvature. To further test the method it could be interesting to use it to compute shock-CMMV interactions, which would serve as a model for the re-shock of single- and multi-mode Richtmyer-Meshkov instabilities.

To increase the usefulness of this method a better approximation for the post-shock pressure and density fields must be obtained. There are a number of possible ways this might be achieved. The most obvious is to design a method which allows for the inclusion of sub-critical angles in the post-shock pressure integrals. Alternatively, using Samtaney & Zabusky [84] as a guide, perhaps the integration could be done incrementally in y, rather then in Fourier space. Essentially we would be chopping the vortex into horizontal slivers, computing the interaction of each sliver with the shock, and resuming all the post-shock slivers to obtain the approximate post-shock fields. This may overcome the restriction of not being able to include the evanescent post-shock pressure waves.

Appendix A Nomenclature

Roman letters

a	In phase magnitude of shock angle perturbation
A	RHS of governing equation for post-shock stream-function
$\mathbf{A}$	Chapter 3, discrete stability operator
b	Out of phase magnitude of shock angle perturbation
B	RHS of governing equation for post-shock stream-function
$\mathbf{B}$	Chapter 3, discrete stability operator
c	Integration constant for Ribner analysis
$\mathbf{c}$	Discrete state perturbation vector
c_∞	Constant, reference sound speed as $\lvert y \rvert \to \infty$
c_v	Constant volume specific heat
c_p	Constant pressure specific heat
C	Constant, reference post-shock sound speed
C_A	Constant, reference pre-shock sound speed
C_1, C_2	RHS boundary condition on post-shock velocities
d	Integration constant for Ribner analysis
dC_A	Perturbation to constant pre-shock sound speed
E	Eccentricity of local streamlines
h	Total enthalpy
$\mathbf{k} = (k_x, k_y)$	Pre-shock perturbation wave vector
$\mathbf{k}'$, $\mathbf{k}''$	Post-shock shear-entropy and pressure wave vectors
M_c	Convective Mach number
M_l	Local Mach number
M_{max}	Maximum local Mach number
M_S	Shock Mach number

M_U	Normal post-shock Mach number
M_∞	Free-stream Mach number
N_x	Number of collocation points in x
N_y	Number of collocation points in y
p	Chapter 4, Mallier & Maslowe pressure profile
p	Chapter 5, post-shock pressure perturbation
p_A	Chapter 5, pre-shock pressure perturbation
$p_j \quad j = 1, \cdots, 4$	Contribution to pressure from each pre-shock perturbation
p_{pw}	Chapter 6, post-shock pressure from pressure wave integral
p_r	Mallier & Maslowe constant, reference pressure
p_∞	Mallier & Maslowe constant, free-stream pressure
P	Constant, reference post-shock pressure
P_A	Constant, reference pre-shock pressure
R	Constant, reference post-shock density
R_A	Constant, reference pre-shock density
R_1, R_2	RHS boundary condition on post-shock velocities
$\mathcal{R}$	Computational domain
s	Chapter 4, Mallier & Maslowe entropy profile
s	Chapter 5, post-shock entropy perturbation
s_0	Chapter 4, strain rate for incompressible solution
s_A	Chapter 5, pre-shock entropy perturbation
s_c	Chapter 4, strain rate for compressible solution
$s_j \quad j = 1, \cdots, 4$	Contribution to entropy from each pre-shock perturbation
s_n	Normalized strain rate
s_{sw}	Chapter 6, post-shock entropy due to shear wave integral
s_∞	Chapter 4, constant, free-stream entropy
$\overline{s}(x, y)$	Chapter 3, steady base-flow entropy
$\overline{s}_A(x, y)$	Chapter 6, steady pre-shock entropy field
$\hat{s}_A(\mathbf{k})$	Chapter 6, pre-shock entropy Fourier component
$\hat{s}(x, y)$	Chapter 3, normal mode entropy perturbation

$s'(x,y,z,t)$	Chapter 3, general entropy perturbation
$S_j(\mathbf{k}, M_S)$	Shear entropy wave transfer function
T_1, T_2	RHS boundary condition on post-shock velocities
u	Component of velocity in the x-direction
$\mathbf{u}$	Velocity vector
u_{pw}	Chapter 6, post-shock x velocity due to pressure wave integral
u_{sw}	Chapter 6, post-shock x velocity due to shear wave integral
$\overline{u}(x,y)$	Chapters 3 & 6, steady CSV x velocity
$\overline{u}_A(x,y)$	Chapter 6, steady compact pre-shock x velocity
$\hat{u}(x,y)$	Chapter 3, normal mode x velocity perturbation
$\hat{u}_A(\mathbf{k})$	Chapter 6, pre-shock x velocity Fourier component
$\hat{u}_A^{(1)}(\mathbf{k})$	Chapter 6, pre-shock rotational x velocity Fourier component
$\hat{u}_A^{(2)}(\mathbf{k})$	Chapter 6, pre-shock compressible x velocity Fourier component
$u'(x,y,z,t)$	Chapter 3, general x velocity perturbation
U	Post-shock constant normal velocity in the x-direction
U_A	Pre-shock constant normal velocity in the x-direction
v	Component of velocity in the y-direction
v_{pw}	Chapter 6, post-shock y velocity due to pressure wave integral
v_{sw}	Chapter 6, post-shock y velocity due to shear wave integral
$\overline{v}(x,y)$	Chapters 3 & 6, steady CSV y velocity
$\overline{v}_A(x,y)$	Chapter 6, steady compact pre-shock y velocity
$\hat{v}(x,y)$	Chapter 3, normal mode y velocity perturbation
$\hat{v}_A(\mathbf{k})$	Chapter 6, pre-shock y velocity Fourier component
$\hat{v}_A^{(1)}(\mathbf{k})$	Chapter 6, pre-shock rotational y velocity Fourier component
$\hat{v}_A^{(2)}(\mathbf{k})$	Chapter 6, pre-shock compressible y velocity Fourier component
$v'(x,y,z,t)$	Chapter 3, general y velocity perturbation
V	Post-shock constant tangential velocity in the y-direction
$w^{(1)}$	Post-shock perturbational velocity in the main-stream direction
$w^{(2)}$	Post-shock perturbational velocity in the cross-stream direction
$w_0^{(1)}$	Post-shock velocity, evaluated at the shock, in main-stream direction

$w_0^{(2)}$	Post-shock velocity, evaluated at the shock, in cross-stream direction
$w_A^{(1)}$	Pre-shock perturbational velocity in the main-stream direction
$w_A^{(2)}$	Pre-shock perturbational velocity in the cross-stream direction
$w_p^{(1)}$	Post-shock potential velocity in the main-stream direction
$w_p^{(2)}$	Post-shock potential velocity in the cross-stream direction
$w_s^{(1)}$	Post-shock shear velocity in the main-stream direction
$\hat{w}(x,y)$	Chapter 3, normal mode z velocity perturbation
$w'(x,y,z,t)$	Chapter 3, general z velocity perturbation
$\mathbf{w}_A$	Pre-shock perturbational velocity vector
W	Post-shock main-stream speed in Ribner's frame of reference
W_A	Pre-shock main-stream speed in Ribner's frame of reference

Greek letters

α	Normal mode wave number in x
α_m	Exponential decay coefficient
α_s	Steady normal mode wave number in x
β	Normal mode wave number in z
β_m	Exponential decay coefficient
β_s	Steady normal mode wave number in z
γ	Ratio of specific heats
δ	Vorticity thickness
δ_{s_j}	Shear wave phase shift
δ_{p_j}	Pressure wave phase shift
δ_{σ_j}	Shock perturbation phase shift
δ_{n_j}	Entropy wave phase shift
ϵ	Mass flow rate between adjacent vortex cores
ϵ_1	Magnitude of main-stream pre-shock velocity perturbation
ϵ_2	Magnitude of cross-stream pre-shock velocity perturbation
ϵ_3	Magnitude of pre-shock temperature perturbation
ϵ_4	Magnitude of pre-shock entropy perturbation

η	Stretching factor
η_0	Cutoff for numerical Fourier transforms
θ	Angle between $\mathbf{k}$ and unperturbed shock
θ_{crit}	Critical incident angle
θ_d	Momentum thickness
θ'	Angle between $\mathbf{k}'$ and unperturbed shock
θ''	Angle between $\mathbf{k}''$ and unperturbed shock
κ	Mallier & Maslowe and Stuart vortex solution parameter
μ	Non-linear eigenvlaue for Mallier & Maslowe and Stuart vortex
$\mu_M = \operatorname{arccot}(\beta_w)$	Mach angle
ν	Velocity ratio across a normal shock
$\xi^{(1)}$	Post-shock main-stream direction
$\xi^{(2)}$	Post-shock cross-stream direction
Π_j	Pressure wave transfer function
ρ	Density
ρ_{sp}	Post-shock density field due to shear-entropy and pressure waves
ρ_∞	Constant free-stream density as $\|y\| \to \infty$
$\overline{\rho}(x, y)$	Steady CSV density field
$\hat{\rho}(x, y)$	Chapter 3, normal mode density perturbation
$\rho'(x, y, z, t)$	Chapter 3, general density perturbation
$\sigma = \sigma_r + i\sigma_i$	Chapter 3, normal mode growth rate
$\sigma(y)$	Chapter 5, perturbation to shock angle
τ	Chapter 4, temperature field
τ	Chapter 5, post-shock temperature perturbation
τ_A	Pre-shock temperature perturbation
$\overline{\tau}(x, y)$	CSV temperature profile
$\overline{\tau}_A(x, y)$	General pre-shock temperature profile
$\hat{\tau}_A(\mathbf{k})$	Pre-shock temperature Fourier component
ψ	Stream-function
ω	Vorticity

Appendix B Continuous spectrum for CD profile

A continuous spectrum is to be expected for an inviscid shear flow in an unbounded domain. In this appendix we discuss the properties of the continuous spectrum for the CD profile. This is useful for separating the discrete and continuous parts of spectra found in the numerical analysis of both the parallel and the CSV profiles. From (2.33), an ordinary differential equation may be obtained by taking Fourier transforms in both x and z, and a Laplace transform in time. Defining the operator $G(y;\sigma,\alpha) = \sigma + i\alpha\overline{u}(y)$, which corresponds to the substantial time derivative, previously denoted by L in definition (2.27), the transformed equation then reads,

$$G\,\frac{d^2R}{dy^2} - 2\frac{dG}{dy}\,\frac{dR}{dy} - \left(M_\infty^2 G^3 + \left(\alpha^2+\beta^2\right)G\right)R = 0, \tag{B.1}$$

$$\lim_{|y|\to\infty} R(y;\sigma,\alpha,\beta) = 0. \tag{B.2}$$

The discrete normal modes, or eigenvectors, are found by considering those values of σ for which this homogeneous equation has a nontrivial solution, vanishing at $y=\pm\infty$. The zeros of $G(y;\sigma,\alpha)$, define where a continuum of eigenvalues may be expected. For the CD profile, this suggests a continuous spectrum on the imaginary axis, between $\pm\alpha$. Letting $y\to\pm\infty$, and using a dominant balance argument on equation (B.1) gives

$$R(y;\sigma,\alpha,\beta) \sim \begin{cases} e^{-\nu^+ y}: & \nu^+ = (\alpha^2+\beta^2+M_\infty^2(\sigma+i\alpha)^2)^{\frac{1}{2}}, \quad y\to\infty \\ e^{+\nu^- y}: & \nu^- = (\alpha^2+\beta^2+M_\infty^2(\sigma-i\alpha)^2)^{\frac{1}{2}}, \quad y\to-\infty \end{cases} \tag{B.3}$$

Condition (B.2) requires that $\mathcal{R}(\nu^\pm)\geq 0$. To ensure this, a branch cut must be introduced in the complex σ plane; Miles [56]. For simplicity, considering purely 2D

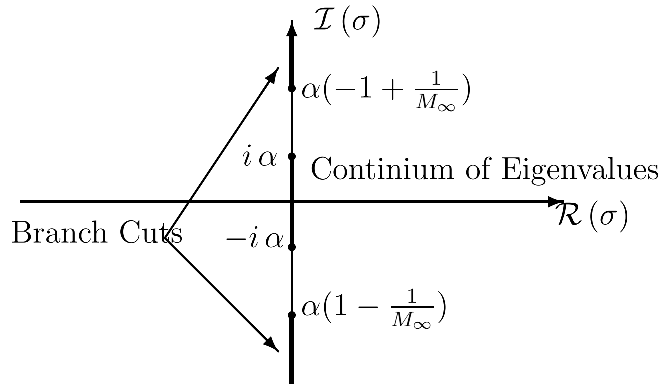

Figure B.1: Graphical representation of the branch cuts and continuum of eigenvalues

perturbations ($\beta = 0$), four branch points are obtained in the σ plane, for real α, from which branch cuts may be defined so that $\mathcal{R}(\nu^{\pm}) \geq 0$, as shown graphically in figure B.1

$$\nu^{+} \rightarrow \sigma_b^{+} = i\alpha\left(1 \pm \frac{1}{M_\infty}\right), \tag{B.4}$$

$$\nu^{-} \rightarrow \sigma_b^{-} = i\alpha\left(-1 \pm \frac{1}{M_\infty}\right), \tag{B.5}$$

$$\text{Branch Cut A}: \quad \sigma_{\mathrm{r}} = 0, \quad 1 - \frac{1}{\mathrm{M}_\infty} \leq \sigma_{\mathrm{i}} \leq \infty, \tag{B.6}$$

$$\text{Branch Cut B}: \quad \sigma_{\mathrm{r}} = 0, \quad -1 + \frac{1}{\mathrm{M}_\infty} \geq \sigma_{\mathrm{i}} \geq -\infty. \tag{B.7}$$

The presence of a branch cut in the Laplace transform generally implies the existence of a continuous spectrum in the operator A. Continuous spectra are generally difficult to resolve numerically, as if σ_c is an eigenvalue associated with the continuous spectrum, then $(A - \sigma_c I)^{-1}$ exists but is unbounded. These difficulties manifested themselves in a number of ways computationally. As the resolutions was increased, the spectral radius of the numerical spectrum also increased, figure B.2a. We believe these extra eigenvalues to be spurious ones, filling out the continuous part of the spectrum. This made the implementation of a subspace based Arnoldi type eigenvalue solver impractical, as for such systems a shift and invert method must be used. The

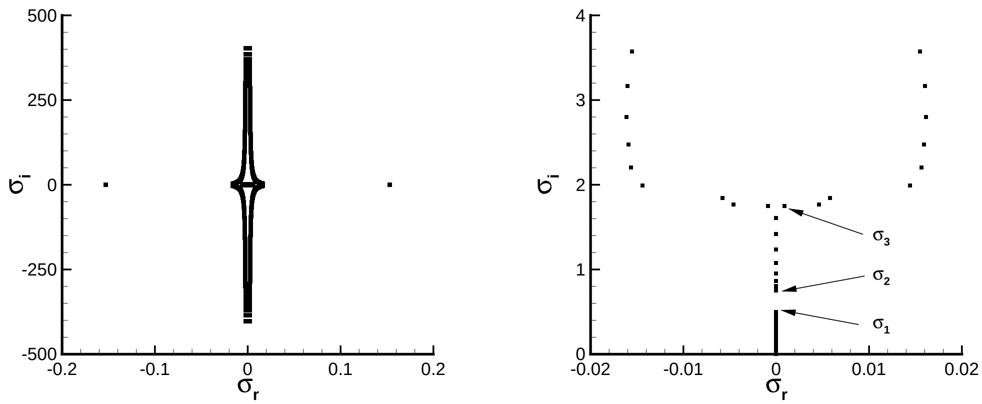

(a) (b)

Figure B.2: (a) Numerical spectrum of operator A using CD base flow. $N_y = 256$, $M_\infty = 0.4$, $\alpha = 0.5$, $\beta = 0.0$. (b) Zoomed region of the numerical spectrum, $\sigma_1 = 0.5i$, $\sigma_2 = 0.75i$, and $\sigma_3 = 0.00091 + 1.75i$.

numerical operators are so badly conditioned that the Krylov solvers, necessary to make these methods practical, failed to converge.

The numerical evidence that the spectrum for the CD profile has the form indicated in figure B.1 comes from figure B.2b. The eigenvalue σ_1 may be identified with the largest eigenvalue in the continuum of eigenvalues, located between $-i\alpha$ and $i\alpha$. The beginning of branch cut A is located at σ_2, and the imaginary part of σ_3 corresponds to the positive branch point from definition (B.4) of σ_b^+.

Spurious eigenvalues are not robust to small perturbations in the discretized matrix, and may be identified by examining the numerical spectrum under increasing resolution, or by using different numerical techniques to discretize the system. For example, all the eigenvalues with imaginary part greater than σ_3 were found to be strongly dependent on the resolution, the greater the resolution the smaller their real parts became.

The problem of spurious eigenvalues is more severe when using the CSV base flow, but the general structure described for the CD base flow remains. For calculations done with non-parallel base flows collocation points must be placed in two directions, thereby limiting the maximum resolution in each direction. Runs where there is about equal resolution in the x and y directions, show the presence of spurious eigenvalues with non zero growth rates. In fact their growth rates can be larger than the growth rates associated with the physical eigenvalues. To identify these spurious eigenvalues, at a given combination of the input parameter, the spectrum is computed at a number of different resolution, using algebraic and exponential stretching, and with modified Hermite polynomials in the y-direction, rather than Chebyschev. Using the numerical spectrums from these calculations, the spurious eigenvalues are identified and discarded.

Appendix C Ribner: Governing equation

In this appendix we define the various terms from equation (5.20), the equation governing the perturbations to the velocity down stream of the shock. They can be broken into five separate terms. The first is due to variable vorticity in the initial perturbation,

$$(\Omega)_1^{GE} = \sec(\theta') + 2(\nu - 1)\cos(\theta'). \tag{C.1}$$

The second stems from fluctuating compressibility in the upstream flow,

$$(\Delta)_1^{GE} = \frac{(\nu - 1)^2}{\nu}\sin(\theta'). \tag{C.2}$$

The third represents the temperature perturbation,

$$(\Theta)_1^{GE} = \left(\frac{\nu^2}{(\gamma - 1)}M_S^{-2} + \frac{1}{2}(\nu - 1)^2\right)\cos(\theta'), \tag{C.3}$$

and the fourth is due to the entropy perturbation,

$$(\Lambda)_1^{GE} = -\frac{1}{\gamma(\gamma - 1)}M_U^{-2}\sin(\theta'). \tag{C.4}$$

The final term is generated by the deviation from vertical of the normal shock,

$$(\Sigma)_1^{GE} = \frac{(\nu - 1)^2}{\nu}\sin(\theta'). \tag{C.5}$$

Appendix D Ribner: Boundary condition

In this appendix the abbreviations used for characterizing boundary conditions on the main and cross-stream velocity perturbations at the shock, equations (5.27) , for an upstream disturbance of general form are described. The abridged notation used when these conditions are specialized to disturbances which are sinusoidal in nature, equations (5.28), is also detailed.

D.1 General form

Vorticity in the initial perturbation and shock curvature; $w_A^{(1)}/W_A$ and $\sigma(y)$,

$$R_1 = \left(1 - 2\frac{\gamma-1}{\gamma+1}\nu\right)\left(\frac{w_A^{(1)}}{W_A} - \frac{\tan(\theta')}{\nu}\sigma\right), \tag{D.1}$$

$$R_2 = \nu\sigma + \tan(\theta')\frac{w_A^{(1)}}{W_A}. \tag{D.2}$$

Variable compressibility; $w_A^{(2)}/W_A$,

$$C_1 = \left(1 - 2\frac{\gamma-1}{\gamma+1}\nu\right)\frac{\tan(\theta')}{\nu}\frac{w_A^{(2)}}{W_A}, \tag{D.3}$$

$$C_2 = \nu\frac{w_A^{(2)}}{W_A}. \tag{D.4}$$

Temperature perturbation; τ_A/T_A,

$$T_1 = \left(1 - \frac{\gamma-1}{\gamma+1}\right)\frac{\tau_A}{T_A}. \tag{D.5}$$

These boundary conditions are independent of the upstream entropy perturbations, as the entropy does not appear in the equation governing the perturbation to the normal Mach number upstream of the shock, equation (5.6). The entropy enters through the right hand side of the governing equation.

D.2 Sinusoidal form

For sinusoidal perturbations equations (D.1)-(D.5) may be reduced to the following. Vorticity; ϵ_1 terms from equations (5.28),

$$(\Omega)_1^{BC} = -\left(1 - 2\frac{\gamma-1}{\gamma+1}\nu\right)\cos(\theta') + \frac{\sin^2(\theta')}{\cos(\theta')}, \tag{D.6}$$

$$(\Omega)_2^{BC} = 2\left(1 - \frac{\gamma-1}{\gamma+1}\nu\right)\sin(\theta'). \tag{D.7}$$

Compressibility; ϵ_2 terms from equations (5.28),

$$(\Delta)_1^{BC} = \frac{1}{\nu}\left(1 - 2\frac{\gamma-1}{\gamma+1}\nu + \nu^2\right)\sin(\theta'), \tag{D.8}$$

$$(\Delta)_2^{BC} = -\frac{1}{\nu}\left(1 - 2\frac{\gamma-1}{\gamma+1}\nu + \nu^2\right)\frac{\sin^2(\theta')}{\cos(\theta')}. \tag{D.9}$$

Temperature; ϵ_3 terms from equations (5.28),

$$(\Theta)_1^{BC} = \left(1 - \frac{\gamma-1}{\gamma+1}\nu\right)\cos(\theta'), \tag{D.10}$$

$$(\Theta)_2^{BC} = -\left(1 - \frac{\gamma-1}{\gamma+1}\nu\right)\sin(\theta'). \tag{D.11}$$

Shock curvature; a and b terms from equations (5.28),

$$(\Sigma)_1^{BC} = \frac{1}{\nu}\left(1 - 2\frac{\gamma-1}{\gamma+1}\nu + \nu^2\right)\sin(\theta'), \tag{D.12}$$

$$(\Sigma)_2^{BC} = -\frac{1}{\nu}\left(1 + \frac{3-\gamma}{\gamma+1}\nu\right)\frac{\sin^2(\theta')}{\cos(\theta')} + (\nu-1)\cos(\theta'). \tag{D.13}$$

Appendix E Horizontal wave solution

In this appendix we consider the problem of convection through a normal shock, of a frozen horizontal sinusoidal disturbance in upstream vorticity, dilatation, temperature and entropy. A solution valid everywhere down stream of the perturbed shock is derived. For $\theta = 0$ the governing equation and boundary conditions reduce substantially and the solution may be written in a simple, compact form. This solution also serves as a useful consistency check for the limiting solution to the general case of $\theta \neq 0$.

For a horizontal wave; $V = 0$, $W = U$, $\theta' = 0$, $k = k'$, $\xi_1 = x$, and $\xi_2 = y$. The governing equation reduces to

$$(1 - M_U^2)\psi_{xx} + \psi_{yy} = -Uk' \left(\epsilon_1(2\nu - 1) + \epsilon_3 \frac{\nu}{\gamma + 1}\left(M_S^{-2} + \frac{2}{\gamma - 1}\right) - \epsilon_4 \frac{M_U^{-2}}{\gamma(\gamma - 1)}\right)\sin(ky), \tag{E.1}$$

with boundary conditions on the main and cross stream velocity given by,

$$\frac{w_0^{(1)}}{U} = -\epsilon_1\left(1 - 2\frac{\gamma - 1}{\gamma + 1}\nu\right)\cos(ky) + \epsilon_3\left(1 - \frac{\gamma - 1}{\gamma + 1}\nu\right)\cos(ky), \tag{E.2}$$

$$\frac{w_0^{(2)}}{U} = a\,(\nu - 1)\cos(ky) + b\,(\nu - 1)\sin(ky). \tag{E.3}$$

The solution to equation (E.1) is written as the sum of a particular integral and complementary function. Define $\beta_u^2 = 1 - M_U^2$, then

$$\psi_p = \frac{U}{k'}\left(\epsilon_1(2\nu - 1) + \epsilon_3\frac{\nu}{\gamma - 1}\left(M_S^{-2} + \frac{2}{\gamma - 1}\right) - \epsilon_4\frac{M_U^{-2}}{\gamma(\gamma - 1)}\right)\sin(ky), \tag{E.4}$$

$$\psi_c = U\exp\left(-\frac{kx}{\beta_u}\right)\left(d\sin(ky) + c\cos(ky)\right), \tag{E.5}$$

where c and d are the constants of integration. To compute (a, b, c, d), use expressions

(E.4) and (E.5) to compute the perturbational velocities, then, let $x = 0$ and compare with boundary conditions (E.2) and (E.3). Equating the respective coefficients of $\sin(ky)$ and $\cos(ky)$ gives $a = 0$, implying $c = 0$, and

$$kd = \frac{b(\nu-1)}{\beta_u} = -\epsilon_1\frac{4\nu}{\gamma+1} + \epsilon_3\frac{\nu}{\gamma-1}\left(M_S^{-2} - \frac{2}{\gamma-1}\right) + \epsilon_4\frac{M_U^{-2}}{\gamma(\gamma-1)}. \tag{E.6}$$

Inclusion of (E.6) in equations (E.4) and (E.5) allows the perturbational velocity components, valid everywhere downstream of the shock, to be derived.

$$\begin{aligned}\frac{u}{U} &= \frac{b(\nu-1)}{\beta_u}\cos(kx)\exp\left(-\frac{kx}{\beta_u}\right) + \left(\epsilon_1(2\nu-1)\right. \\ &+ \left.\epsilon_3\frac{\nu}{\gamma+1}\left(M_S^{-2} + \frac{2}{\gamma-1}\right) - \epsilon_4\frac{M_U^{-2}}{\gamma(\gamma-1)}\right)\cos(ky) \qquad \text{(E.7)} \\ \frac{v}{U} &= b(\nu-1)\sin(ky)\exp\left(-\frac{kx}{\beta_u}\right) \qquad \text{(E.8)}\end{aligned}$$

The pressure perturbation is determined from the velocity field through a linearized Bernoulli equation, equation (5.23),

$$\frac{p}{P_A} = -\frac{\gamma M_S^2}{\nu}\frac{b(\nu-1)}{\beta_u}\cos(ky)\exp\left(-\frac{kx}{\beta_u}\right), \tag{E.9}$$

while the linear equation of state is used to compute the density, equation (5.24),

$$\frac{\rho}{R_A} = \left(\frac{\nu}{\gamma}\frac{P_A}{P}\right)\frac{p}{P_A} - \left(\left(\epsilon_1 + \frac{\epsilon_3}{2}\right)\nu(\nu-1)^2(\gamma-1)M_U^2 - \epsilon_4\frac{\nu}{\gamma}\right)\cos(ky). \tag{E.10}$$

The irrotational, compressible velocity field, associated with the complementary function ψ_c, and the pressure perturbation decay exponentially fast with down stream distance from the shock. Far down stream of the shock the flow is incompressible, with a variable vorticity, density and entropy field. Expressions (E.9) and (E.10), evaluated at $x = 0$, can be derived independently from the Rankine-Hugoniot jump conditions for pressure and density, which serves as a useful consistency check for the current analysis. The absence of ϵ_2, in both the governing equation and boundary conditions, imply that for this limiting case, the compressibility of the upstream disturbance does not effect the post-shock perturbations to the uniform down stream flow, or the shock inclination angle.

The local inclination of the shock from vertical is given by equation (5.18). The integral of this expression with respect to y gives the local shock displacement in the x direction relative to the mean shock plane.

$$\delta x = \frac{\beta_u}{k(\nu - 1)} \left(\epsilon_1 \frac{4\nu}{\gamma + 1} - \epsilon_3 \frac{\nu}{\gamma - 1} \left(M_S^{-2} - \frac{2}{\gamma - 1} \right) - \epsilon_4 \frac{M_U^{-2}}{\gamma(\gamma - 1)} \right) \cos(ky). \quad \text{(E.11)}$$

For the general case, $\theta \neq 0$, the solution technique will remain the same; solving equation (5.20) to obtain a solution valid everywhere downstream of the shock, matching this solution to boundary conditions (5.28) at the shock to obtain a system of linear algebraic equations for a and b, the parameters governing the shock inclination, and c and d, the constants of integration.

Appendix F Subsonic solution

In this appendix we derive and solve the linear algebraic system of equations governing the constants a, b, c and d for subsonic downstream flow. The solution is manipulated so that, for the limiting case of $\epsilon_2 = \epsilon_3 = \epsilon_4 = 0$, Ribner's results are easily recovered. To facilitate this, the additional constants C, D, E and F are required.

Expressions (5.31) and (5.32), used in equation (5.7), give the velocity perturbations downstream of the shock.

$$\begin{aligned}\frac{w^{(1)}}{U} &= A\cos(k'\xi_2) + B\sin(k'\xi_2) \\ &+ \beta_u^2 \exp\left(-\frac{k'\beta_w}{\beta_u^2}\cos(\theta')\left[\xi_1\cos(\theta') - \xi_2\sin(\theta')\right]\right) \\ &\times \left[(c\sin(\theta') + d\beta_w\cos(\theta'))\cos\left(\frac{k'\cos(\theta)(\xi_1\sin(\theta') + \beta_w^2\xi_2\cos(\theta'))}{\beta_u^2}\right)\right. \\ &\left. + (-c\beta_w\cos(\theta') + d\sin(\theta'))\sin\left(\frac{k'\cos(\theta)(\xi_1\sin(\theta') + \beta_w^2\xi_2\cos(\theta'))}{\beta_u^2}\right)\right]\end{aligned} \tag{F.1}$$

$$\begin{aligned}\frac{w^{(2)}}{U} &= \beta_u^2 \exp\left(-\frac{k'\beta_w}{\beta_u^2}\cos(\theta')\left[\xi_1\cos(\theta') - \xi_2\sin(\theta')\right]\right) \\ &\times \left[\left(c\beta_w^2\cos(\theta') - d\beta_w\sin(\theta')\right)\cos\left(\frac{k'\cos(\theta)(\xi_1\sin(\theta') + \beta_w^2\xi_2\cos(\theta'))}{\beta_u^2}\right)\right. \\ &\left. + \left(c\beta_w\sin(\theta') + d\beta_w^2\cos(\theta')\right)\sin\left(\frac{k'\cos(\theta)(\xi_1\sin(\theta') + \beta_w^2\xi_2\cos(\theta'))}{\beta_u^2}\right)\right]\end{aligned} \tag{F.2}$$

Along the shock $\xi_1\cos(\theta') = \xi_2\sin(\theta')$, so that at the shock the argument of the exponential reduces to zero and the arguments of the sine and cosine terms reduces to $k'\xi_2$. Thus, the respective coefficients of $\sin(k'\xi_2)$ and $\cos(k'\xi_2)$ from the expressions for $w^{(1)}$ and $w^{(2)}$, equations (F.1) and (F.2), may be matched to those for $w_0^{(1)}$ and $w_0^{(2)}$, boundary conditions (5.28), at the shock. This yields four simultaneous equations, (5.33), for the constants a, b, c and d.

The four terms, H_1-H_4, multiplying the constants a, b, c and d on the left hand side of equations (5.33) are:

$$
\begin{aligned}
H_1 &= (\Sigma)_1^{GE} - (\Sigma)_1^{BC} = -\frac{4}{\gamma+1}\sin(\theta'), && \text{(F.3)}\\
H_2 &= \frac{1}{\beta_u^2}\sin(\theta'), && \text{(F.4)}\\
H_3 &= \frac{\beta_w}{\beta_u^2}\cos(\theta'), && \text{(F.5)}\\
H_4 &= (\Sigma)_2^{BC} = \frac{1}{\nu}\left(1+\frac{3-\gamma}{\gamma+1}\nu\right)\frac{\sin^2(\theta')}{\cos(\theta')} - (\nu-1)\cos(\theta'). && \text{(F.6)}
\end{aligned}
$$

The terms from the right hand side of these equations, due to vorticity, compressibility, temperature and entropy, are:

$$
\begin{aligned}
(\Omega)_1 &= (\Omega)_1^{BC} - (\Omega)_1^{GE} = -\frac{4\nu}{\gamma+1}\cos(\theta'), && \text{(F.7)}\\
(\Omega)_2 &= (\Omega)_2^{BC} = 2\left(1-\frac{\gamma-1}{\gamma+1}\right)\sin(\theta) && \text{(F.8)}\\
(\Delta)_1 &= (\Delta)_1^{BC} - (\Delta)_1^{GE} = \frac{4}{\gamma+1}\sin(\theta'), && \text{(F.9)}\\
(\Delta)_2 &= (\Delta)_2^{BC} = -\frac{1}{\nu}\left(1-2\frac{\gamma-1}{\gamma+1}\nu+\nu^2\right)\frac{\sin^2(\theta')}{\cos(\theta')}, && \text{(F.10)}\\
(\Theta)_1 &= (\Theta)_1^{BC} - (\Theta)_1^{GE} = \frac{\nu}{\gamma+1}\left(M_S^{-2}-\frac{2}{\gamma-1}\right)\cos(\theta'), && \text{(F.11)}\\
(\Theta)_2 &= (\Theta)_2^{BC} = -\left(1-\frac{\gamma-1}{\gamma+1}\nu\right)\sin(\theta'), && \text{(F.12)}\\
(\Lambda)_1 &= -(\Lambda)_1^{GE} = \frac{M_U^{-2}}{\gamma(\gamma-1)}\cos(\theta'). && \text{(F.13)}
\end{aligned}
$$

Using various forms of the oblique shock relations, and defining the constants

$$
\begin{aligned}
C &= \left(\frac{\gamma-1}{\gamma+1}+\frac{3-\gamma}{\gamma+1}\nu\right)\tan(\theta') - \left((\nu-1)^2+\frac{2(\nu-1)}{\gamma+1}\right)\sin(\theta')\cos(\theta'), && \text{(F.14)}\\
D &= \frac{\beta_w}{\beta_u^2}D' = \frac{\beta_w}{\beta_u^2}(\nu-1)\left(1+(\nu-1)\cos^2(\theta')\right), && \text{(F.15)}\\
E &= \frac{\beta_w^2}{\beta_u^2}2(\nu-1)\cos^2(\theta') + 2\left(1-\frac{\gamma-1}{\gamma+1}\nu\right), && \text{(F.16)}\\
F &= \frac{\beta_w}{\beta_u^2}F' = \frac{\beta_w}{\beta_u^2}\left(2(\nu-1)\sin(\theta')\cos(\theta')\right), && \text{(F.17)}
\end{aligned}
$$

allows the solution to be written in the following form:

$$a = \sum_{j=1}^{4} \epsilon_j a_j, \quad b = \sum_{j=1}^{4} \epsilon_j b_j, \quad c = \sum_{j=1}^{4} \epsilon_j c_j, \quad d = \sum_{j=1}^{4} \epsilon_j d_j, \tag{F.18}$$

where

$$a_1 = \frac{\nu(CE+DF)}{C^2+D^2}, \tag{F.19}$$

$$a_2 = \frac{\Delta_1}{H_1} + \frac{\nu^2 H_4}{H_1 \beta_u^2} \frac{H_1(\Delta)_2 - H_4(\Delta)_1}{C^2+D^2}, \tag{F.20}$$

$$a_3 = \frac{\Theta_1}{H_1} + \frac{\nu^2 H_4}{H_1 \beta_u^2} \frac{H_1(\Theta)_2 - H_4(\Theta)_1}{C^2+D^2}, \tag{F.21}$$

$$a_4 = \frac{\Lambda_1}{H_1} - \frac{\nu^2 H_4}{H_1 \beta_u^2} \frac{H_4(\Lambda)_1}{C^2+D^2}, \tag{F.22}$$

$$b_1 = \frac{\nu(CF-DE)}{C^2+D^2}, \tag{F.23}$$

$$b_2 = \frac{\nu^2 \beta_w}{\beta_u^2} \frac{H_1(\Delta)_2 - H_4(\Delta)_1}{C^2+D^2}, \tag{F.24}$$

$$b_3 = \frac{\nu^2 \beta_w}{\beta_u^2} \frac{H_1(\Theta)_2 - H_4(\Theta)_1}{C^2+D^2}, \tag{F.25}$$

$$b_4 = -\frac{\nu^2 \beta_w}{\beta_u^2} \frac{H_4(\Lambda)_1}{C^2+D^2}, \tag{F.26}$$

$$c_1 = D' \frac{CE+DF}{C^2+D^2} - F', \tag{F.27}$$

$$c_2 = \nu C \frac{H_4(\Delta)_1 - H_1(\Delta)_2}{C^2+D^2}, \tag{F.28}$$

$$c_3 = \nu C \frac{H_4(\Theta)_1 - H_1(\Theta)_2}{C^2+D^2}, \tag{F.29}$$

$$c_4 = \nu C \frac{H_4(\Lambda)_1}{C^2+D^2}, \tag{F.30}$$

$$d_1 = D' \frac{CF-DE}{C^2+D^2}, \tag{F.31}$$

$$d_2 = \nu D \frac{H_1(\Delta)_2 - H_4(\Delta)_1}{C^2+D^2}, \tag{F.32}$$

$$d_3 = \nu D \frac{H_1(\Theta)_2 - H_4(\Theta)_1}{C^2+D^2}, \tag{F.33}$$

$$d_4 = -\nu D \frac{H_4(\Lambda)_1}{C^2+D^2}. \tag{F.34}$$

This solution can be easily seen to reduce to R54 for $\epsilon_1 = \epsilon_2 = \epsilon_3 = 0$. If the additional generalization of out of phase temperature and entropy perturbation is allowed, the right hand side of the second and fourth equations from the system defined by (5.33) would be non-zero, and depend on the out of phase components of these perturbations. For this case, extra terms would appear in the expressions for a, b, c and d, dependent upon those out of phase components.

The constants A and B can also be written in a compact fashion:

$$A = \sum_{j=1}^{4} \epsilon_j A_j, \quad B = \sum_{j=1}^{4} \epsilon_j B_j, \tag{F.35}$$

where

$$A_1 = (\Omega)_1^{GE} + (\Sigma)_1^{GE} a_1, \tag{F.36}$$

$$A_2 = (\Delta)_1^{GE} + (\Sigma)_1^{GE} a_2, \tag{F.37}$$

$$A_3 = (\Theta)_1^{GE} + (\Sigma)_1^{GE} a_3, \tag{F.38}$$

$$A_4 = (\Lambda)_1^{GE} + (\Sigma)_1^{GE} a_4, \tag{F.39}$$

$$B_1 = (\Sigma)_2^{GE} b_1, \tag{F.40}$$

$$B_2 = (\Sigma)_2^{GE} b_2, \tag{F.41}$$

$$B_3 = (\Sigma)_2^{GE} b_3, \tag{F.42}$$

$$B_4 = (\Sigma)_2^{GE} b_4. \tag{F.43}$$

Appendix G Supersonic solution

In this appendix we derive and solve the linear algebraic system of equations governing the constants a and c for supersonic downstream mean velocity W. This system of equations is considerably simpler than the system for subsonic downstream flow, as the B terms are set to zero from the outset. As in Appendix F, the solution is manipulated so that the incompressible solution in R54, can be easily recovered for the limiting case of $\epsilon_2 = \epsilon_3 = \epsilon_4 = 0$. The constants C', D', E', F' and G are introduced to aid this process.

Expressions (5.34) and (5.35), used in equation (5.7), give the velocity perturbations downstream of the shock.

$$\frac{w^{(1)}}{U} = A\cos(k'\xi_2) + \frac{c\sec(\theta')}{\beta_w + \tan(\theta')}\cos\left(\frac{k'(\xi_1 + \beta_w\xi_2)}{\beta_w + \tan(\theta')}\right) \tag{G.1}$$

$$\frac{w^{(2)}}{U} = \frac{c\beta_w\sec(\theta')}{\beta_w + \tan(\theta')}\cos\left(\frac{k'(\xi_1 + \beta_w\xi_2)}{\beta_w + \tan(\theta')}\right) \tag{G.2}$$

Along the shock $\xi_1 = \xi_2\tan(\theta')$, and the arguments of the cosine terms reduce to $k'\xi_2$. At the shock the respective coefficients of $\cos(k'\xi_2)$ from the expressions for $w^{(1)}$ and $w^{(2)}$, equations (G.1) and (G.2), may be matched to those for $w_0^{(1)}$ and $w_0^{(2)}$, boundary conditions (5.28). This yields two simultaneous equations for the constants a and c.

The three terms, G_1-G_3, multiplying the constants a and c on the left hand side of equations (5.36) are

$$G_1 = (\Sigma)_1^{GE} - (\Sigma)_1^{BC} = -\frac{4}{\gamma+1}\sin(\theta'), \tag{G.3}$$

$$G_2 = \frac{\sec(\theta')}{\beta_w + \tan(\theta')}, \tag{G.4}$$

$$G_3 = (\Sigma)_2^{BC} = \frac{1}{\nu}\left(1 + \frac{3-\gamma}{\gamma+1}\nu\right)\frac{\sin^2(\theta')}{\cos(\theta')} - (\nu - 1)\cos(\theta') \tag{G.5}$$

The terms from the right-hand side of these equations, due to vorticity, compressibility, temperature and entropy, are

$$\begin{aligned}
(\Omega)_1 &= (\Omega)_1^{BC} - (\Omega)_1^{GE} = -\frac{4\nu}{\gamma+1}\cos(\theta'), && \text{(G.6)}\\
(\Omega)_2 &= (\Omega)_2^{BC} = 2\left(1 - \frac{\gamma-1}{\gamma+1}\right)\sin(\theta) && \text{(G.7)}\\
(\Delta)_1 &= (\Delta)_1^{BC} - (\Delta)_1^{GE} = \frac{4}{\gamma+1}\sin(\theta'), && \text{(G.8)}\\
(\Delta)_2 &= (\Delta)_2^{BC} = -\frac{1}{\nu}\left(1 - 2\frac{\gamma-1}{\gamma+1}\nu + \nu^2\right)\frac{\sin^2(\theta')}{\cos(\theta')}, && \text{(G.9)}\\
(\Theta)_1 &= (\Theta)_1^{BC} - (\Theta)_1^{GE} = \frac{\nu}{\gamma+1}\left(M_S^{-2} - \frac{2}{\gamma-1}\right)\cos(\theta'), && \text{(G.10)}\\
(\Theta)_2 &= (\Theta)_2^{BC} = -\left(1 - \frac{\gamma-1}{\gamma+1}\nu\right)\sin(\theta'), && \text{(G.11)}\\
(\Lambda)_1 &= -(\Lambda)_1^{GE} = \frac{M_U^{-2}}{\gamma(\gamma-1)}\cos(\theta'). && \text{(G.12)}
\end{aligned}$$

As for the subsonic solution, various forms of the oblique shock relations are used to manipulate the solution into a manageable form.

$$\begin{aligned}
C' &= 2\frac{\gamma-1}{\gamma+1}\nu - 2\left(1 + (\nu-1)\cos^2(\theta')\right), && \text{(G.13)}\\
D' &= (\nu-1)\left(1 + (\nu-1)\cos^2(\theta')\right), && \text{(G.14)}\\
E' &= (\nu-1)^2\sin(\theta')\cos(\theta') - \left(1 + \frac{3-\gamma}{\gamma+1}\nu\right)\tan(\theta'), && \text{(G.15)}\\
F' &= 2(\nu-1)\sin(\theta')\cos(\theta') && \text{(G.16)}\\
G &= \frac{1-\beta_w\tan(\theta')}{\beta_w + \tan(\theta')} = \tan(\mu_M - \theta'), && \text{(G.17)}
\end{aligned}$$

where $\mu_M = \operatorname{arccot}(\beta_w)$ is the Mach angle. The solution is then written in the following form:

$$a = \sum_{j=1}^{4}\epsilon_j a_j, \quad c = \sum_{j=1}^{4}\epsilon_j c_j, \tag{G.18}$$

where

$$\begin{aligned}
a_1 &= \frac{\nu(C' + GF')}{E' + GD'}, && \text{(G.19)}\\
a_2 &= -\frac{\nu\sec(\theta')}{\beta_w + \tan(\theta')}\frac{(\Delta)_2 - \beta_w(\Delta)_1}{E' + GD'}, && \text{(G.20)}\\
a_3 &= -\frac{\nu\sec(\theta')}{\beta_w + \tan(\theta')}\frac{(\Theta)_2 - \beta_w(\Theta)_1}{E' + GD'}, && \text{(G.21)}\\
a_4 &= \frac{\nu\sec(\theta')}{\beta_w + \tan(\theta')}\frac{\beta_w(\Lambda)_1}{E' + GD'}, && \text{(G.22)}\\
c_1 &= \frac{D'C' - F'E'}{E' + GD'}, && \text{(G.23)}\\
c_2 &= -\nu\frac{G_3(\Delta)_1 - G_1(\Delta)_2}{E' + G'}, && \text{(G.24)}\\
c_3 &= -\nu\frac{G_3(\Theta)_1 - G_1(\Theta)_2}{E' + G'}, && \text{(G.25)}\\
c_4 &= -\nu\frac{G_3(\Theta)_1}{E' + G'}. && \text{(G.26)}
\end{aligned}$$

Out of phase temperature and entropy perturbations would generate an additional independent set of two linear algebraic equations for the constants b and d. The out of phase components would not appear in the expressions for a and c, however, the constants b and d would depend exclusively on those components.

For in phase perturbations in this regime the B terms are zero, and the constant A is written as

$$A = \sum_{j=1}^{4} \epsilon_j A_j, \qquad \text{(G.27)}$$

where

$$\begin{aligned}
A_1 &= (\Omega)_1^{GE} + (\Sigma)_1^{GE} a_1, && \text{(G.28)}\\
A_2 &= (\Delta)_1^{GE} + (\Sigma)_1^{GE} a_2, && \text{(G.29)}\\
A_3 &= (\Theta)_1^{GE} + (\Sigma)_1^{GE} a_3, && \text{(G.30)}\\
A_4 &= (\Lambda)_1^{GE} + (\Sigma)_1^{GE} a_4. && \text{(G.31)}
\end{aligned}$$

Appendix H Constants and limits

In this appendix we give the definition of the various terms in the entropy transfer function defined by equation (5.47). Also, some of the constants and transfer functions used in Chapter 5 have limits which are non-trivial to compute as $\theta \to \pi/2$. The following relationships are used extensively in computing these limits.

$$\frac{\cos(\theta)}{\cos(\theta')} \to \nu \quad \text{as} \quad \theta \to \pi/2, \tag{H.1}$$

$$\frac{\cos(\theta')}{\cos(\theta'')} \to \frac{M_U}{M_U+1} \quad \text{as} \quad \theta \to \pi/2, \tag{H.2}$$

$$\sin(\mu_M)\beta_w \to 1 \quad \text{as} \quad \theta \to \pi/2, \tag{H.3}$$

Entropy transfer functions:

$$\frac{s_1}{c_p} = CNST \times \sin(\theta)\left[(\cot(\theta)-a_1)^2+b_1^2\right]^{\frac{1}{2}}, \tag{H.4}$$

$$\frac{s_2}{c_p} = -CNST \times \sin(\theta)\left[(a_2+1)^2+b_2^2\right]^{\frac{1}{2}}, \tag{H.5}$$

$$\frac{s_3}{c_p} = -CNST \times \tan(\theta)\left[(\frac{1}{2}\cot(\theta)-a_3)^2+b_3^2\right]^{\frac{1}{2}}, \tag{H.6}$$

$$\frac{s_4}{c_p} = CNST \times \tan(\theta)\left[\left(\frac{\cot(\theta)}{\gamma}\frac{2(\gamma-1)(\nu-1)^2}{(\gamma+1)\nu-(\gamma-1)}-a_4\right)^2+b_4^2\right]^{\frac{1}{2}}, \tag{H.7}$$

where

$$CNST = \frac{2(\gamma-1)(\nu-1)^2}{(\gamma+1)\nu-(\gamma-1)}. \tag{H.8}$$

Entropy phase shifts:

$$\begin{aligned}
\delta_{n_1} &= \arctan\left(\frac{b}{\cot(\theta)-a}\right), && \text{(H.9)}\\
\delta_{n_2} &= \arctan\left(\frac{-b}{a-1}\right), && \text{(H.10)}\\
\delta_{n_3} &= \arctan\left(\frac{-b}{\frac{1}{2}\cot(\theta)-a}\right), && \text{(H.11)}\\
\delta_{n_4} &= \arctan\left(\frac{-b\tan(\theta)\times CNST}{\frac{1}{\gamma}-a\tan(\theta)\times CNST}\right) && \text{(H.12)}
\end{aligned}$$

Limits as $\theta \to \pi/2$:

$$\frac{p_1}{\cos(\theta)P} \to \frac{1}{M_U}\frac{2\gamma}{(\gamma+1)\nu-(\gamma-1)} \times \left[2(\nu-1)\frac{M_U}{M_U+1} + \frac{(\nu-1)\left(2\nu\frac{\gamma-1}{\gamma+1}-2-2(\nu-1)\frac{M_U}{M_U+1}\right)}{\left(1+\frac{3-\gamma}{\gamma+1}\nu\right)\frac{M_U+1}{M_U}+\nu-1}\right] \tag{H.13}$$

$$\frac{s_1}{\cos(\theta)c_p} \to \frac{2(\gamma-1)(\nu-1)^2}{\nu(\gamma+1)-(\gamma-1)}\left[1+2\left(\frac{\nu\frac{\gamma-1}{\gamma+1}-1-(\nu-1)\frac{M_U}{M_U+1}}{1+\frac{3-\gamma}{\gamma_1}\nu+(\nu-1)\frac{M_U}{M_U+1}}\right)\right] \tag{H.14}$$

$$a_2 \to -\left[\left(1+\frac{3-\gamma}{\gamma+1}\nu\right)(M_U+1)+(\nu-1)M_U\right]^{-1} \times \left[1-2\frac{\gamma-1}{\gamma+1}\nu+\nu^2+\frac{4\nu}{\gamma+1}M_U\right] \tag{H.15}$$

$$c_2 \to -\nu(\nu-1)\frac{4}{\gamma+1}\left[1+\frac{3-\gamma}{\gamma+1}\nu+(\nu-1)\frac{M_U}{M_U+1}\right]^{-1} \tag{H.16}$$

$$\frac{p_2}{P} \to \nu(\nu-1)\frac{4}{\gamma+1}\frac{2\gamma\nu}{(\gamma+1)\nu-(\gamma-1)} \times \left[\left(1+\frac{3-\gamma}{\gamma+1}\nu\right)(M_U+1)+(\nu-1)M_U\right]^{-1} \tag{H.17}$$

$$\frac{p_3}{P} \to -\frac{1}{M_U}\frac{2\gamma\nu}{(\gamma+1)\nu-(\gamma-1)} \times \left[\left(1+\frac{3-\gamma}{\gamma+1}\nu\right)\frac{M_U+1}{M_U}+\nu-1\right]^{-1} \times \left[\frac{1}{\gamma+1}\left(M_s^{-2}-\frac{2}{\gamma-1}\right)\left(1+\frac{3-\gamma}{\gamma+1}\nu\right)-\frac{4}{\gamma+1}\left(1-\frac{\gamma-1}{\gamma+1}\nu\right)\right] \tag{H.18}$$

$$\frac{s_3}{c_p} \to -\frac{2(\gamma-1)(\nu-1)^2}{(\gamma+1)\nu-(\gamma-1)} \times \left[\frac{1}{2}+\frac{1}{M_U+1}\left[1+\frac{3-\gamma}{\gamma+1}\nu+(\nu-1)\frac{M_U}{M_U+1}\right]^{-1} \times \left[1-\frac{\gamma-1}{\gamma+1}\nu+M_U\frac{\nu}{\gamma+1}\left(M_S^{-2}-\frac{2}{\gamma-1}\right)\right]\right] \tag{H.19}$$

$$\frac{p_4}{P} \to -\frac{1}{M_U^3}\frac{1}{\gamma-1}\frac{2}{(\gamma+1)\nu-(\gamma-1)}\left(1+\frac{3-\gamma}{\gamma+1}\nu\right) \times \left[\left(1+\frac{2-\gamma}{\gamma+1}\right)\nu\frac{M_U+1}{M_U}+\nu-1\right]^{-1} \tag{H.20}$$

$$\frac{s_4}{c_p} \to \frac{1}{\gamma}-\frac{1}{\gamma}\frac{2(\nu-1)^2}{(\gamma+1)\nu-(\gamma-1)} \times \left[\left(1+\frac{3-\gamma}{\gamma+1}\nu\right)M_U(M_U+1)+(\nu-1)M_U^2\right]^{-1} \tag{H.21}$$

Bibliography

[1] A. Aleshin, E. Gamalii, S. Zaitsev, E. Lazareva, I. Lebo, and V. Rozanov. Nonlinear and transitional states in the onset of the Richtmyer-Meshkov instability. *Sov. Tech. Phys. Lett.*, 14(6):466–468, 1988.

[2] B. Bayly. Three-dimensional instability of elliptical flow. *Physical Review Letters*, 57(17):2160–2163, 1986.

[3] M. Berger and J. Oliger. Adaptive mesh refinement for hyperbolic partial differential equations. *J. Comp. Phys.*, 53:484–512, 1984.

[4] L. Bernal and A. Roshko. Streamwise vortex structure in plane mixing layers. *J. Fluid Mech.*, 170:499–525, 1986.

[5] S. Birch and J. Eggers. A critical review of the experimental data for developed free turbulent shear layers. *NASA SP-321*, pages 11–40, 1972.

[6] W. Blumen. Shear layer instabilities of an inviscid compressible fluid. *J. Fluid Mech.*, 40:769–781, 1970.

[7] W. Blumen, P. Drazin, and D. Billings. Shear layer instabilities of an inviscid compressible fluid. part 2. *J. Fluid Mech.*, 71:305–316, 1975.

[8] D. Bogdanoff. Compressibility effects in turbulent shear layers. *AIAA J.*, 21:926–927, 1983.

[9] J. Boyd. A Chebyshev polynomial method for computing analytic solutions to eigenvalue problems with applications to the anharmonic oscillator. *J. Math. Phys*, 19:1445–1456, 1978.

[10] J. Boyd. Spectral and pseudospectral methods for eigenvalue and nonseperable boundary value problems. *Monthly Weather Review*, 106:1192–1203, 1978.

[11] J. Boyd. The optimization of convergence for Chebyshev polynomial methods in an unbounded domain. *J. Comp. Phys.*, 45:43–79, 1982.

[12] M. Brouillette and B. Sturtevant. Experiments on the Richtmyer-Meshkov instability: single-scale perturbations on a continuous interface. *J. Fluid Mech.*, 263:271–292, 1994.

[13] F. Browand and B. Latigo. Growth of the two-dimensional mixing layers from a turbulent and nonturbulent boundary layer. *Phys. Fluids*, 22(6):1011–1019, 1979.

[14] G. Brown and A. Roshko. On density effects and large structure in turbulent mixing layers. *J.. Fluid Mech.*, 64:775–816, 1974.

[15] J. M. Budzinski, Benjamin R. F., and J. F. Jacobs. Influence of initial conditions on the flow patters of a shock accelerated thin fluid layer. *Phys. Fluids*, 6:3510–3512, 1994.

[16] A. Cain, J. Ferziger, and W. Reynolds. Discrete orthogonal function expansions for nonuniform grids using the fast fourier transform. *J. Comp. Phys.*, 56:272–286, 1984.

[17] C. Chandrsuda, R. Mehta, A. Weir, and P. Bradshaw. Effect of free-stream turbulence on large structures in turbulent mixing layers. *J. Fluid Mech.*, 85, 1978.

[18] C. Chang. Interaction of a plane shock and oblique plane disturbance with special reference to entropy waves. *J. of the Aeronautical Sciences*, pages 675–682, 1957.

[19] N. Chinzei, G. Masuya, T. Komuro, A. Murakami, and K. Kudoi. Spreading of two-stream supersonic turbulent mixing layers. *Phys of Fluids*, 29(5):1345–1347, 1986.

[20] B. Chu and L. S. Kovasznay. Non-linear interactions in a viscous heat-conducting compressible gas. *J. Fluid Mech.*, 3:494–514, 1958.

[21] N. Clemens and M. Mungal. Large-scale structure end entrainment in the supersonic mixing layer. *J. Fluid Mech.*, 284:171–216, 1995.

[22] B. D. Collins and J. W. Jacobs. PLIF flow visualization and measurements of the Richtmyer-Meshkov instability of an air/SF6 interface. *J. Fluid Mech.*, 464:113–136, 2002.

[23] Ralf Deiterding. Construction and application of an AMR algorithm for distributed memory computers. In *Proc. of Chicago Workshop on Adaptive Mesh Refinement Methods*, page in press. ASCI/Flash Center, Springer, Sep 3-5 2003.

[24] Ralf Deiterding. *Parallel adaptive simulation of multi-dimensional detonation structures*. PhD thesis, Brandenburgische Technische Universität Cottbus, Sep 2003.

[25] Ralf Deiterding. AMROC - Blockstructured Adaptive Mesh Refinement in Object-oriented C++. Available at http://amroc.sourceforge.net, Mar 2004.

[26] S. Goebel and J. Dutton. Experimental study of compressible turbulent mixing layers. *AIAA Journal*, 29(4):538–546, 1991.

[27] F. Grasso and S. Pirozzoli. Shock-wave-vortex interactions: Shock and vortex deformations, and sound production. *Theoret. Comput. Fluid Dynamics*, 13:412–456, 2000.

[28] J. Hall, P. Dimotakis, and H. Rosemann. Experiments in non-reacting compressible shear layers. *AIAA Journal*, 31(12):1993, 1993.

[29] S. W. Hann. Weakly nonlinear hydrodynamic instabilities in inertial fusion. *Phys. Fluids B*, 3:2349–2247, 1991.

[30] D. J. Hill and D. I. Pullin. Hybrid tuned centered-difference-weno method for large eddy simulations in the presence of strong shocks. *J. Comp. Phys.*, 194:435–450, 2004.

[31] O. Inoue. Propagation of sound generated by weak shock-vortex interaction. *Phys. Fluids*, 12(6):1258–1261, 2000.

[32] O. Inoue and Y. Hattori. Sound generation by shock-vortex interactions. *J. Fluid Mech.*, 380:81–116, 1999.

[33] O. Inoue and T. Yasuo. Successive generation of sounds by shock strong-vortex interaction. *Phys. Fluids*, 12(12):3229–3234, 2000.

[34] J. Jacobs, D. G. Jenkins, D. L. Klein, and Benjamin R. Nonlinear growth of the shock-accelerated instability of a thin fluid layer. *J. Fluid Mech.*, 295:23–42, 1995.

[35] M. A. Jones and J. W. Jacobs. A membraneless experiment for the study of Richtmyer-Meshkov instability. *Phys. Fluids*, 9:3078–3085, 1997.

[36] G. P. Klaassen and W. R. Peltier. The onset of turbulence in finite amplitude kelvin-helmholtz billows. *J. Fluid Mech.*, 155:1–53, 1985.

[37] G. P. Klaassen and W. R. Peltier. The role of transverse secondary instabilities in the evolution of free shear layers. *J. Fluid Mech.*, 202:367–402, 1989.

[38] G. P. Klaassen and W. R. Peltier. The influence of stratification on secondary instability in free shear layers. *J. Fluid Mech.*, 227:71–106, 1991.

[39] H. Lamb. *Hydrodymanics.* Cmabridge Mathematical Library, sixth edition, 1932.

[40] M. Landman and P. Saffman. The three-dimensional instability of strained vortices in a viscous fluid. *Phys. Fluids*, 30(8):2339–2342, 1987.

[41] S. Lee, S. K. Lele, and P. Moin. Direct numerical simulations of isotropic turbulence with a weak shock wave. *J. Fluid Mech.*, 251:533–562, 1993.

[42] S. Lee, S. K. Lele, and P. Moin. Interaction of isotropic turbulence with shock wave: effect of shock strength. *J. Fluid Mech.*, 340:225–247, 1997.

[43] L. Lees and C. Lin. Investigation of the stability of the laminar boundary layer in a compressible fluid. Wash. Rep. 1115, Nat. Adv. Comm. Aero., 1946.

[44] M. Lessen, J. A. Fox, and H. M. Zien. On the inviscid stability of the laminar mixing of two parallel streams of compressible fluid. *J. Fluid Mech.*, 23:355–367, 1965.

[45] M. Lessen, J. A. Fox, and H. M. Zien. Stability of the laminar mixing of two parallel streams with respect to supersonic disturbances. *J. Fluid Mech.*, 25:737–742, 1966.

[46] A. Lifschitz and E. Hameiri. Local stability conditions in fluid dunamics. *Phys. Fluids A*, 3(11):2644–2651, 1991.

[47] C. Lin. On the stability of the laminar mixing region between two parallel streams in a gas. Wash. Rep. 2887, Nat. Adv. Comm. Aero., 1953.

[48] S. Lin and G. Corcos. The mixing layer: deterministic models of turbulent flow. part 3. the effect of plain strain on the dynamics of streamwise vortices. *J. Fluid Mech*, 141:139–178, 1984.

[49] K. Mahesh, S. Lele, and P. Moin. The response of anisotropic turbulence to rapid homogenous one-dimensional compression. *Phys. Fluids*, 6(2):1052–1062, 1994.

[50] K. Mahesh, S. K. Lele, and P. Moin. The influence of entropy fluctuations on the interaction of turbulence with a shock wave. *J. Fluid Mech.*, 334:353–379, 1997.

[51] R. Mallier and S. Maslowe. A row of counter-rotating vortices. *Phys. Fluids A*, 5(4):1074–1075, 1993.

[52] D. I. Meiron, D. W. Moore, and D. I. Pullin. On steady compressible flows with compact vorticity; the compressible stuart vortex. *J. Fluid Mech.*, 409:29–49, 2000.

[53] E.E. Meshkov. Instability of the interface of two gases accelerated by a shock wave. *Izv. Akad. Nauk. SSSR Mehk. Zhidk. Gaza.*, 4:151–157, 1969.

[54] A. Michalke. On spatially growing disturbances in an inviscid shear layer. *J. Fluid Mech.*, 23:521–544, 1965.

[55] K. Mikaelian. Richtmyer-Meshkov instabilities in stratified fluids. *Phys. Rev. A*, 31(1):410–419, 1985.

[56] J. Miles. On the disturbed motion of a plane vortex sheet. *J. Fluid Mech.*, 4(5):538–552, 1958.

[57] D. Moore and P. Saffman. The density of organized vortices in a turbulent mixing layer. *J. Fluid Mech.*, 64:465–473, 1972.

[58] D. W. Moore and D. I. Pullin. The compressible vortex pair. *J. Fluid Mech.*, 185:171–204, 1987.

[59] D. W. Moore and D. I. Pullin. On steady compressible flows with compact vorticity; the compressible hill's spherical vortex. *J. Fluid Mech.*, 374:285–303, 1998.

[60] F. Moore. Unsteady oblique interaction of a shock wave with a plane disturbance. NACA TN 2879, Nat. Adv. Comm. Aero., 1954.

[61] C. S. Morawetz. On the non-existence of continuous transonic flow past airfoils. I. *Commun. Pure Appl. Maths*, 9:45–68, 1956.

[62] C. S. Morawetz. On the non-existence of continuous transonic flow past airfoils. II. *Commun. Pure Appl. Maths*, 10:107–131, 1957.

[63] C. S. Morawetz. On the non-existence of continuous transonic flow past airfoils. III. *Commun. Pure Appl. Maths*, 11:129–144, 1958.

[64] M. Munk and R. Prim. On the multiplicity of steady gas flows having the same streamline pattern. *Proc. Natl. Acad. Sci.*, 33:137–141, 1974.

[65] Staff of the Ames 1-by 3-foot Supersonic Wind-Tunnel Section. Notes and tables for use in the analysis of supersonic flow. NACA TN 1428, Nat. Adv. Comm. Aero., 1947.

[66] D. Papamoschou. *Experimental investigation of heterogeneous compressible shear layers*. PhD thesis, California Institute of Technology, 1986.

[67] D. Papamoschou and A. Bunyajitradulya. Evolution of large eddies in compressible shear layers. *Phys. Fluids*, 9(3):756–765, 1996.

[68] D. Papamoschou and A. Roshko. The compressible turbulent shear layer: an experimental study. *AIAA paper*, 86-0162, 1986.

[69] D. Papamoschou and A. Roshko. The compressible turbulent shear layer: an experimental study. *J. Fluid Mech.*, 197:453–477, 1988.

[70] T. Pham and D. I. Meiron. A numerical study of Richtmyer-Meshkov instability in continuously stratified fluids. *Phys. Fluids A*, 5(2):344–368, 1993.

[71] R. Pierrehumbert. Universal short-wave instability of two-dimensional eddies in an inviscid fluid. *Physcial Review Letters*, 57(27):2157–2159, 1986.

[72] R. Pierrehumbert and S. Widnall. The two- and three- dimension instabilities of a spatially periodic shear layer. *J. Fluid Mech.*, 114:59–82, 1982.

[73] S. Ragab and J. Wu. Linear instabilities in two-dimensional compressible mixing layers. *Phys. Fluids A*, 1(6):957–966, 1989.

[74] H. Ribner. Convection of a pattern of vorticity through a shock wave. NACA. Rep. 1164, Nat. Adv. Comm. Aero., 1954.

[75] H. Ribner. Shock-turbulence interaction and the generation of noise. NACA. Rep. 1233, Nat. Adv. Comm. Aero., 1955.

[76] H. Ribner. The sound generated by interaction of a single vortex with a shock wave. UTIA TN 61, Univ. of Toronto, Inst. for Aerospace Studies, 1959.

[77] H. Ribner. Acoustic energy flux from shock-turbulence interaction. *J. Fluid Mech.*, 35:299–310, 1969.

[78] H. Ribner. Cylindrical sound wave generated by shock-vortex interaction. *AIAA Journal*, 23(11):1708–1715, 1985.

[79] R. D. Richtmyer. Taylor instability in shock acceleration of compressible fluids. *Commum. Puer Appl. Maths*, 23:297–319, 1960.

[80] L. Rosenhead. The spread of vorticity in the wake behind a cylinder. *Roy. Soc. Proc.A*, 127:590–612, 1930.

[81] O. Sadot, L. Erez, U. Alon, D. Oron, L. Levin, G. Erez, G. Ben-Dor, and D. Shvarts. Study of nonlinear evolution of single-mode and two-bubble interaction under Richtmyer-Meshkov instability. *Phys. Rev. Lett.*, 80:1654–1657, 1998.

[82] P. G. Saffman and D. I. Meiron. Kinetic energy generated by the incompressible Richtmyer-Meshkov instability in a continuously stratified fluid. *Phys. Fluids A*, 11(1):1767–1771, 1989.

[83] M. Samimy and G. Elliott. Effects of compressibility in the characteristics of free shear layers. *AIAA Journal*, 28(3):439–445, 1990.

[84] R. Samtaney and N. Zabusky. Circulation deposition on shock-accelerated planar and curved density-stratified interfaces: Models and scaling laws. *J. Fluid Mech.*, 269:45, 1994.

[85] N. D. Sandham and W. C. Reynolds. Compressible mixing layer: linear theory and direct simulation. *AIAA*, 28(4):618–624, 1990.

[86] N. D. Sandham and W. C. Reynolds. Three-dimensional simulations of large eddies in the compressible mixing layer. *J. Fluid Mech.*, 224:133–158, 1991.

[87] M Sirieix and J. Solignac. Contribution a l'etude experimentale de la couche de melange turbulent isobare d'un ecoulment supersonique. *AGARD*, CP4, 1966.

[88] M. Slessor. *Aspects of turbulent-shear-layer dynamics and mixing.* PhD thesis, California Institute of Technology, 1998.

[89] M. Slessor, M. Zhuang, and P. Dimotakis. Turbulent shear-layer mixing: growth-rate compressibility scaling. *J. Fluid Mech.*, 414:35–45, 2000.

[90] J. Stuart. On finite amplitude oscillations in laminar mixing layers. *J. Fluid Mech.*, 29:417–440, 1967.

[91] F. Waleffe. On the three-dimensional instability of strained vortices. *Phys. Fluids A*, 2(1):76–80, 1990.

[92] C. Winant and F. Browand. Vortex pairing: The mechanism of turbulent mixing layer growth at moderate reynolds number. *J. Fluid Mech.*, 63:237–255, 1974.

[93] Y. Yang, T. Kubota, and E.E. Zukoski. Application of shock-induced mixing to supersonic combustion. *AIAA J.*, 31:854–862, 1993.

[94] Q. Zhang and S. Sohn. Non-linear theory of unstable fluid mixing driven by shock wave. *Phys. Fluids*, 9:1106–1124, 1997.

[95] M. Zhuang and P. Dimotakis. Instability of wake dominated compressible mixing layers. *Phys. Fluids*, 7(10):2489–2495, 1995.

[96] M. Zhuang, P. Dimotakis, and T. Kubota. The effect of walls on spatially growing supersonic shear layers. *Phys. Fluids*, 2(4):599–604, 1990.

[97] M. Zhuang, T. Kubota, and P. Dimotakis. Instability of inviscid, compressible free shear layers. *AIAA*, 28(10):1728–1733, 1990.